

# The convective instability of the BEK system of rotating boundary-layer flows over rough disks

*Thesis submitted for the degree of*

*Doctor of Philosophy*

*at the University of Leicester*

*by*

*Burhan Alveroğlu MSc (Nottingham)*

*Department of Mathematics*

*University of Leicester*

April 2016

# The convective instability of the BEK system of rotating boundary-layer flows over rough disks

Burhan Alveroğlu

## Abstract

A numerical study investigating the effects of surface roughness on the stability properties of the BEK system of flows is introduced. The BEK system of flows occur in many engineering applications such as turbo-machinery and rotor-stator devices, therefore they have great practical importance. Recent studies have been concerned with the effects of surface roughness on the von Kármán flow<sup>1</sup>. The aim of this thesis is to investigate whether distributed surface roughness could be used as a passive drag reduction technique for the broader BEK system of flows. If it can, what is “the right sort of roughness?” To answer these questions, a linear stability analysis is performed using the Chebyshev collocation method to investigate the effect of particular types of distributed surface roughness, both anisotropic and isotropic, on the convective instability characteristics of the inviscid Type I (cross-flow) instability and the viscous Type II instability. The results reveal that all roughness types lead to a stabilisation of the Type I mode in all flows within the BEK family, with the exception of azimuthally-anisotropic roughness (radial grooves) within the Bödewadt flow which causes a mildly destabilising effect. In the case of the Type II mode, the results reveal the destabilising effect of radially-anisotropic roughness (concentric grooves) on all the boundary layers, whereas both azimuthally-anisotropic and isotropic roughness have a stabilising effect on the mode for Ekman and von Kármán flows. Moreover, an energy analysis is performed to investigate the underlying physical mechanisms behind the effects of rough surfaces on the BEK system. The conclusion is that isotropic surface roughness is the most effective type of the distributed surface roughness and can be recommended as a passive-drag reduction mechanism for the entire BEK system of flows.

---

<sup>1</sup> Cooper *et al.* (2015) & Garrett *et al.* (2016)

To the loving memory of my mother who passed away in 2009...

## Acknowledgements

Firstly, I would like to express my sincere gratitude to my advisor Prof. Stephen Garrett for the continuous support during my Ph.D. studies and related research, for his patience, motivation, and immense knowledge. His guidance helped me research and write this thesis. I could not have imagined having a better advisor and mentor for my Ph.D studies. My sincere thanks also goes to Dr. Antonio Segalini, who help me develop the MATLAB code used in this study. I also wish to acknowledge financial support from Republic of Turkey, Ministry of National Education.

I would also like to thank all my friends and their families in Leicester and Nottingham for their friendships and support, Murat Gürer, Ahmet Faruk Acar, Sabahattin Çağ, Osman Ay, Fatih Say, Adnan Ayna, Asuman and Fuat Usta, Yedigâr and İshak Fırat, Gürbüz Çomak, Kürşat Çevik, Ercan Eser, Recep Yücedoğru, Ahmet Durgungöz, İbrahim Duman, Neslihan Sönmez, Emrah Haspolat, Kevser Sevim, Ahmet Kaya, Halil İbrahim Eğilmez Ömer Faruk Zararsız, Salih Cihangir, Gökmen Durmuş, Nurdan Çabukoğlu and Özcan Gazioğlu.

Last but not the least, I would like to thank my family: my father and to my brothers Sinan and Tarık and sister Deniz for supporting me spiritually throughout writing this thesis and my life in general.

Burhan ALVEROĞLU

# Contents

<b>1</b>	<b>Introduction</b>	<b>1</b>
1.1	Motivation and aim of the current study . . . . .	7
<b>2</b>	<b>The governing equations of the linear stability analysis</b>	<b>12</b>
2.1	Overview . . . . .	12
2.2	A brief description of the BEK flows . . . . .	13
2.3	Derivation of the governing equations . . . . .	15
2.3.1	The steady mean flows . . . . .	15
2.3.2	Derivation of the perturbation equations . . . . .	21
2.3.3	Derivation of the energy balance equations . . . . .	29
<b>3</b>	<b>Numerical methods</b>	<b>33</b>
3.1	Matlab solver for the steady mean flow . . . . .	33
3.2	Chebyshev spectral methods . . . . .	35
3.2.1	Overview of the spectral methods . . . . .	36
3.2.2	Implementation of Chebyshev collocation method . . . . .	39
<b>4</b>	<b>Effect of azimuthally anisotropic roughness on the BEK family of boundary layers</b>	<b>47</b>
4.1	Overview . . . . .	47
4.2	The steady mean flow solutions . . . . .	48
4.3	The convective instability analysis . . . . .	55
4.3.1	Neutral curves . . . . .	55
4.3.2	The growth rates . . . . .	64

---

4.4	Energy Analysis . . . . .	67
4.5	Absolute instability . . . . .	71
4.6	Conclusion . . . . .	72
<b>5</b>	<b>Effect of radially anisotropic roughness on the BEK family of boundary layers</b>	<b>74</b>
5.1	Overview . . . . .	74
5.2	The steady mean flow solutions . . . . .	75
5.3	The convective instability analysis . . . . .	81
5.3.1	Neutral curves . . . . .	82
5.3.2	The growth rates . . . . .	91
5.4	Energy Analysis . . . . .	92
5.5	Absolute instability . . . . .	99
5.6	Conclusion . . . . .	100
<b>6</b>	<b>Effect of isotropic roughness on the BEK family of boundary layers</b>	<b>102</b>
6.1	Overview . . . . .	102
6.2	The steady mean flow solutions . . . . .	103
6.3	The convective instability analysis . . . . .	109
6.3.1	Neutral curves . . . . .	110
6.3.2	The growth rates . . . . .	116
6.4	Energy Analysis . . . . .	118
6.5	Absolute instability . . . . .	121
6.6	Conclusion . . . . .	122
<b>7</b>	<b>Conclusion</b>	<b>124</b>
7.1	Comparison of main results . . . . .	124

---

7.2	Future work . . . . .	131
<b>Appendix A MATLAB codes for the convective instability analysis</b>		<b>134</b>
A.1	Mean flow solver . . . . .	134
A.1.1	Function for setup of the governing mean flow equations . . .	135
A.1.2	Function for setup of the partial-slip boundary conditions . . .	136
A.2	Convective instability solvers . . . . .	136
A.2.1	Main solver . . . . .	136
A.2.2	Function for energy analysis . . . . .	139
A.2.3	Functions for Chebyshev method . . . . .	140
<b>List of References</b>		<b>146</b>

# List of Figures

1.1	Visualisation of the instability and transition on a rotating disk. Reproduced from Gregory <i>et al.</i> (1955). . . . .	4
1.2	Experimental image of the transition process in the Bödewadt flow, reproduced from Cros <i>et al.</i> (2005). The angular velocity of the fluid increases from 9rpm to 20rpm, from top left to bottom right and the radius of the disk is $R = 140$ mm. . . . .	5
1.3	Sketch of (i) stable, (ii) convectively unstable and (iii) absolutely unstable disturbances. . . . .	6
2.1	Variation in $Co$ with $Ro$ for the BEK system flows . . . . .	14
2.2	Evolution of an initial perturbation. (a,b) Temporal growth of a local perturbation; (c,d) temporal growth of a global periodic ; (e,f) spatial evolution of perturbation. Taken from Schmid & Henningson (2012). . . . .	28
3.1	The first few Chebyshev polynomials of first kind. . . . .	39
3.2	Comparable distributed nodes on the rotational disk geometry. . . . .	40
4.1	Radial grooves over a disk. . . . .	48
4.2	Mean-flow components of the von Kármán flow in the case of azimuthally-anisotropic roughness (radial grooves, $\eta = 0$ ). . . . .	49
4.3	Mean-flow components for $Ro = -0.5$ in the case of azimuthally-anisotropic roughness (radial grooves, $\eta = 0$ ) . . . . .	51
4.4	Mean-flow components of the Ekman flow ( $Ro = 0$ ) in the case of azimuthally-anisotropic roughness (radial grooves, $\eta = 0$ ). . . . .	52

4.5	Mean-flow components for $Ro = 0.5$ in the case of azimuthally-anisotropic roughness (radial grooves, $\eta = 0$ ).	53
4.6	Mean-flow components of the Bödewadt flow ( $Ro = 1$ ) in the case of azimuthally-anisotropic roughness (radial grooves, $\eta = 0$ ).	54
4.7	The two spatial branches showing region of crossflow instability for the Ekman flow in the case of $\lambda = 0.5$ ; (a) at $Re = 227$ , (b) at $Re = 500$ .	56
4.8	Neutral curves of the convective instability of the von Kármán flow in the case of azimuthally-anisotropic roughness (radial grooves, $\eta = 0$ ).	57
4.9	Neutral curves of the convective instability for $Ro = -0.5$ in the case of azimuthally-anisotropic roughness (radial grooves, $\eta = 0$ ).	58
4.10	Neutral curves of the convective instability of the Ekman flow in the case of azimuthally-anisotropic roughness (radial grooves, $\eta = 0$ ).	59
4.11	Neutral curves of the convective instability for $Ro = 0.5$ in the case of azimuthally-anisotropic roughness (radial grooves, $\eta = 0$ ).	60
4.12	Neutral curves of the convective instability of the Bödewadt flow in the case of azimuthally-anisotropic roughness (radial grooves, $\eta = 0$ ).	61
4.13	Neutral curves of convective instability for a range of flows within the BEK system in the case of a moderate value of azimuthally-anisotropic roughness parameter, $\lambda = 0.5$ .	63
4.14	Growth rates of Type I instability mode within the BEK boundary layer flows as a function of the vortex number $n$ at $Re = Re_{critical} + 25$ in the case of radial grooves, azimuthally-anisotropic roughness. The red dots indicate the most rapidly growing mode.	66
4.15	Energy balance at the location of maximum amplification of the BEK boundary layer flows at $Re = Re_{critical} + 25$ , except the Bödewadt flow for radially anisotropic roughness. For the Bödewadt flow, $Re = 400$ and $n = 85$ . The terms are normalised by the mechanical energy flux of the most dangerous mode within each figure.	69

4.16	Type I mode profiles for the azimuthal and the axial disturbance velocity profiles of the BEK flows at the location of maximum amplification of the BEK boundary layer flows in the case of a radially grooved disk at $Re = Re_{critical} + 25$ , except for the Bödewadt flow for radially anisotropic roughness. For the Bödewadt flow, $Re = 400$ and $n = 85$ . . . . .	70
5.1	Concentric grooves over a disk. . . . .	75
5.2	Mean-flow components of the von Kármán flow in the case of radially-anisotropic roughness (concentric grooves, $\lambda = 0$ ). . . . .	76
5.3	Mean-flow components for $Ro = -0.5$ in the case of radially-anisotropic roughness (concentric grooves, $\lambda = 0$ ) . . . . .	78
5.4	Mean-flow components of the Ekman flow ( $Ro = 0$ ) in the case of radially-anisotropic roughness (concentric grooves, $\lambda = 0$ ). . . . .	79
5.5	Mean-flow components for $Ro = 0.5$ in the case of radially-anisotropic roughness (concentric grooves, $\lambda = 0$ ). . . . .	80
5.6	Mean-flow components of the Bödewadt flow ( $Ro = 1$ ) in the case of radially-anisotropic roughness (concentric grooves, $\lambda = 0$ ). . . . .	81
5.7	The two spatial branches after the exchange showing regions of both streamline-curvature and crossflow instability at $Re = 195$ for the Ekman flow in the case of $\eta = 0.5$ . . . . .	82
5.8	Neutral curves of the convective instability of the von Kármán flow in the case of radially-anisotropic roughness (concentric grooves, $\lambda = 0$ ). . . . .	83
5.9	Neutral curves of the convective instability for $Ro = -0.5$ in the case of radially-anisotropic roughness (concentric grooves, $\lambda = 0$ ). . . . .	84
5.10	Neutral curves of the convective instability of the Ekman flow in the case of radially-anisotropic roughness (concentric grooves, $\lambda = 0$ ). . . . .	85
5.11	Neutral curves of the convective instability for $Ro = 0.5$ in the case of radially-anisotropic roughness (concentric grooves, $\lambda = 0$ ). . . . .	87

5.12	Neutral curves of the convective instability of the Bödewadt flow in the case of radially-anisotropic roughness (concentric grooves, $\lambda = 0$ ).	88
5.13	Neutral curves of the convective instability of the particular flows in the BEK system in the case of a moderate value of radially-anisotropic roughness, $\eta = 0.5$ .	90
5.14	Growth rates of Type I and Type II instability modes within the BEK boundary layer flows as a function of vortex number $n$ at $Re = Re_{critical} + 25$ in the case of radial grooves, azimuthally-anisotropic roughness. The red dots and circles indicate the most rapidly growing mode for Type I and Type II modes, respectively.	92
5.15	Energy balance of the Type I mode of the BEK system of boundary layer flows for radially anisotropic roughness at the location of maximum amplification at $Re = Re_{critical} + 25$ except the Bödewadt flow. For Bödewadt flow, $Re = 400$ and $n = 30$ . The terms are normalised by the mechanical energy flux of the most dangerous mode within each figure.	94
5.16	Energy balance of the Type II mode of the BEK system of boundary layer flows for radially anisotropic roughness at the location of maximum amplification at $Re = Re_{critical} + 25$ , except the Bödewadt flow. For this flow, $Re = 400$ and $n = 12$ . The terms are normalised by the mechanical energy flux of the most dangerous mode within each figure.	95
5.17	Type I mode profiles for the azimuthal and the axial disturbance velocity profiles of the BEK flows in the case of a concentrically grooved disk at the location of maximum amplification at $Re = Re_{critical} + 25$ except the Bödewadt flow. For Bödewadt flow, $Re = 400$ and $n = 30$ .	97

5.18	Type II mode profiles for the azimuthal and the axial disturbance velocity profiles of the BEK flows in the case of a concentrically grooved disk at the location of maximum amplification at $Re = Re_{critical} + 25$ except the Bödewadt flow. For Bödewadt flow, $Re = 400$ and $n = 12$ . . . . .	98
6.1	Distribution of roughness isotropically over a disk. . . . .	103
6.2	Mean-flow components of the von Kármán flow in the case of isotropic roughness ( $\eta = \lambda \neq 0$ ). . . . .	104
6.3	Mean-flow components for $Ro = -0.5$ in the case of isotropic roughness ( $\eta = \lambda \neq 0$ ). . . . .	106
6.4	Mean-flow components of the Ekman flow ( $Ro = 0$ ) in the case of isotropic roughness ( $\eta = \lambda \neq 0$ ). . . . .	107
6.5	Mean-flow components for $Ro = 0.5$ in the case of isotropic roughness ( $\eta = \lambda \neq 0$ ). . . . .	108
6.6	Mean-flow components of the Bödewadt flow ( $Ro = 1$ ) in the case of isotropic roughness ( $\eta = \lambda \neq 0$ ). . . . .	109
6.7	Neutral curves of the convective instability of the von Kármán flow in the case of azimuthally-anisotropic roughness ( $\eta = \lambda \neq 0$ ). . . . .	110
6.8	Neutral curves of the convective instability for $Ro = -0.5$ in the case of isotropic roughness ( $\eta = \lambda \neq 0$ ). . . . .	111
6.9	Neutral curves of the convective instability of the Ekman flow in the case of isotropic roughness ( $\eta = \lambda \neq 0$ ). . . . .	112
6.10	Neutral curves of the convective instability for $Ro = 0.5$ in the case of isotropic roughness ( $\eta = \lambda \neq 0$ ). . . . .	113
6.11	Neutral curves of the convective instability of the Bödewadt flow in the case of isotropic roughness ( $\eta = \lambda \neq 0$ ). . . . .	114
6.12	Neutral curves of the convective instability of the particular flows in the BEK system in the case of a moderate value of isotropic roughness, $\eta = 0.5$ . . . . .	116

- 6.13 Growth rates of Type I instability mode within the BEK boundary layer flows as a function of vortex number  $n$  at  $Re = Re_{critical} + 25$  in the case of isotropic. The red dots indicates the most rapidly growing mode for Type I. . . . . 117
- 6.14 Energy balance at the location of maximum amplification of the BEK boundary layer flows at  $Re = Re_{critical} + 25$  for isotropic roughness. The terms are normalised by the mechanical energy flux of the most dangerous mode within each figure. . . . . 119
- 6.15 Type I mode profiles for the azimuthal and the axial disturbance velocity profiles of the BEK flows at  $Re = Re_{critical} + 25$  in the case of an isotropically rough disk. . . . . 120
- 7.1 Comparative mean-flow components of the main flows of the BEK system. The size of roughness is set to 0.5 in each rough case. . . . 125
- 7.2 Comparative convective neutral curves of the main flows in the BEK system for each type of surface roughness. The size of roughness is set to 0.5 in each rough case. . . . . 126
- 7.3 Comparative convective growth rate curves of the von Kármán and Ekman flows for the Type I mode at the location of maximum amplification of  $Re_{critical} = Re_{critical} + 25$ , where  $Re_{critical}$  corresponds the critical Reynolds number of each type of surface roughness. The size of roughness is set to 0.5 in each rough case. . . . . 127
- 7.4 Energy balance comprasion of Type I mode of the BEK boundary layer flows for each roughness cases at the location of maximum amplification at  $Re = Re_{critical} + 25$ , except the Bödewadt flow. For these flow,  $Re = 400$  and  $n = 40$ . The terms are normalised by the mechanical energy flux of the most dangerous mode within each figure. 128

# List of Tables

4.1	The initial values of $U'$ and $V'$ at the disk surface for various $Ro$ , in the case of azimuthally-anisotropic roughness (radial grooves, $\eta = 0$ ).	50
4.2	Critical values of observable parameters at the onset of convective instability of Type I mode for the flows around $Ro = 0.7$ .	62
4.3	Critical values of observable parameters at the onset of convective instability of both modes for the boundary layers in the BEK system in the case of azimuthally-anisotropic roughness (radial grooves). Type I and (Type II). The most dangerous mode is indicated as bold text in terms of critical Reynolds number.	65
4.4	Critical Reynolds number for the stationary Type I mode interacting with the absolute instability region inside the neutral curves of the BEK system of flows in the case of radial grooves.	71
5.1	The initial values of $U'$ and $V'$ at the disk surface for various $Ro$ (concentric grooves, $\lambda = 0$ ).	77
5.2	Critical values of observable parameters at the onset of convective instability of both modes for the boundary layers in the BEK system in the case of radially-anisotropic roughness (concentric grooves). Type I and (Type II). The most dangerous mode is indicated as bold text in terms of critical Reynolds number.	89
5.3	Critical Reynolds number for the stationary Type I mode interacting with the absolute instability region inside the neutral curves of the BEK system flows in the case of concentric grooves.	99

---

6.1	The initial values of $U'$ and $V'$ at the disk surface for various $Ro$ , calculated by shooting method in case of isotropic roughness ( $\eta = \lambda \neq 0$ ). . . . .	105
6.2	Critical values of observable parameters at the onset of convective instability of both modes for the boundary layers in the BEK system in the case of isotropic roughness. Type I and (Type II). The most dangerous mode is indicated as bold text in terms of critical Reynolds number. . . . .	115
6.3	Critical Reynolds number for the stationary Type I mode interacting with the absolute instability region inside the neutral curves of the BEK system flows in the case of isotropic roughness. . . . .	121
7.1	Critical Reynolds number for the stationary Type I mode interacting with the absolute instability region inside the neutral curves of the BEK system flows in the case of isotropic roughness. . . . .	130

# Chapter 1

## Introduction

Finding a way to reduce the skin-friction drag caused by viscous shear forces acting on the surface of a rigid body moving through a fluid is an important problem in fluid mechanics. This problem has attracted a great deal of attention from numerous authors and has been a research priority in the community for many years. In most technological applications, the skin-friction drag is significantly greater in the turbulent state of the flow than in the laminar state and an intelligent strategy towards drag reduction is to delay the onset of the transition process as long as possible. A promising technique towards drag reduction is potentially to delay the transition of the laminar flow via surface roughness.

The classical belief that smooth surfaces create less skin-friction drag is undermined with the observation of the lower drag on non-smooth (rough) surfaces created by using v-shapes ribbons in the studies of Walsh (1982) and Bechert *et al.* (1985). However, Sirovich & Karlsson (1997) established a series of wind tunnel experiments with specified patterns of roughness on the confining walls and reported that the drag reduction or enhancement that can be achieved depends on the arrangements of those patterns. These studies suggest that carefully designed surface roughness could be used to develop new drag-reduction techniques, but the main problem that remains is to identify what is “the right sort of roughness” that leads to drag reduction effects in any particular application (Carpenter, 1997).

Investigating the transition from laminar to turbulence in fully three-dimensional

flows has been an important aim of much research in the literature for decades. This has typically been motivated by the practical significance of applications involving swept wings. It is well known that fully three-dimensional flows over swept wings have similar inflectional crossflow velocity components to three-dimensional rotating boundary layer flows. This inflectional profile leads to a convectively unstable flow regime in which a characteristic flow instability mechanism manifesting itself in the form of co-rotating crossflow vortices is observed. This instability mechanism is referred to as the Type I instability mode and is inviscid in nature. Owing to this similarity, many theoretical and experimental works using rotating disk flows have been performed to obtain a understanding of the transition process over swept wings.

Early studies related to rotating boundary-layer flows have focussed on understanding the characteristics of laminar-turbulent transition over smooth disks and the investigations of this problem were first performed for the von Kármán boundary layer flow. This was shown by Batchelor (1951) to be a limiting case of a family of three-dimensional rotating flows. The other limiting cases are the Ekman (1905) and Bödewadt (1940) flows established by the introduction of the additional rotating disk in the far-field of the fluid domain. This wide class of boundary layer flows is often referred to as the “BEK” system owing to these particular limiting cases. However, there are infinitely many flows in between these cases established by differential rotation rates between the lower disk and the fluid above generated by the upper rotating disk. The stability characteristics of the BEK flows have practical importance not only for their similarities with the flows over swept wings but also for the occurrence of those flows in turbo-machinery and rotor-stator devices, such as mixers.

The von Kármán flow is induced by the rotation of a single disk in a still fluid and was first introduced by von Kármán (1921). He showed that this flow is an exact solution of the Navier-Stokes equations using the similarity variables that are known now as the von Kármán similarity variables. In part, this mathematical feature makes it attractive for theoretical analyses. The main characterization of the von Kármán flow is the lack of a radial pressure force in the vicinity of the disk

so that the fluid spirals outwards to balance the centrifugal forces and is replaced by an axial flow directed back towards the disk. The resulting velocity distribution in the boundary layer is three-dimensional and has an inflectional component in the radial direction.

The first stability analysis of the von Kármán flow was performed by Gregory *et al.* (1955) who used both theoretical and experimental techniques. Their motivation was to gain a better understanding of the transition process regarding the flow over a swept wing. The presence of the crossflow vortices had firstly been noticed in the experimental studies of Smith (1947) and of Gray (1952) for the rotating disk flows and flows over a swept wing, respectively. The experimental part of the study conducted by Gregory & Walker used a china-clay technique to observe the transition from laminar to turbulent flow. Their study provided photographic evidence showing that these vortices are in a stationary vortex pattern on the disk surface. They reported that the crossflow vortices were first noticed at a Reynolds number of around  $Re = 430$ , whereas the transition was first observed around  $Re = 530$ . The numbers of vortices were around 30 in this pattern while the angle between the normal of vortices and the outward radius vector was measured to be approximately 14 degrees. Figure 1.1 shows the laminar flow, crossflow vortices and fully developed turbulent flow in order of increased radii in the transition process observed in that study. The theoretical part of the study was conducted by Stuart using a linear stability analysis to model the crossflow instabilities for high Reynolds numbers. His prediction for the number of vortices was almost 4 times the experimental observation, but this discrepancy can be attributed to the neglect of viscous forces in the theoretical study. The predictions for the angle of the vortices on the other hand were in total agreement with those observed in the experimental part.

The Ekman flow occurs in the particular case of the lower disk and the fluid in the far-field rotating at approximately the same rate. The flow was first formulated by Ekman (1905) in order to analyse planetary wind-driven rotating flows. The Ekman flow is characterised by the balance between the radial pressure, Coriolis and viscous forces. The stability studies of the Ekman flow was first conducted by

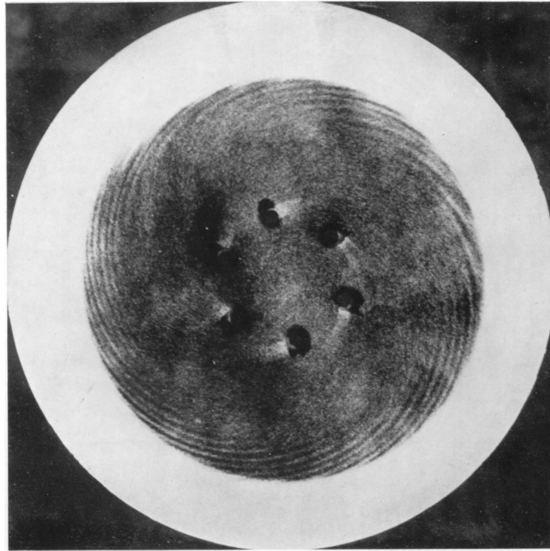


Figure 1.1: Visualisation of the instability and transition on a rotating disk. Reproduced from Gregory *et al.* (1955).

experimentally Faller (1963) and then analytically by Faller & Kaylor (1966). The onset of the inviscid Type I instability mode was obtained around  $Re = 126$  in the experimental study and approximately at  $Re = 118$  in the analytical study. In addition to the inviscid cross-flow instability, a new viscous Type 2 instability mode was detected in both studies and was attributed to the Coriolis force and streamwise curvature effects. This mode was also obtained in the experimental study of Tatro & Mollo-Christensen (1967) and the existence of it was confirmed theoretically by Lilly (1966) and Melander (1983). Lilly also concluded that the inclusion of the Coriolis forces leads to a higher critical Reynolds number for the onset of stationary crossflow vortices via the Type I mode compared to the non-included cases. The Type II mode was later found by Malik (1986) in the case of the von Kármán flow.

The Bödewadt flow is established when the lower disk is stationary and the upper fluid is rotating with a constant angular velocity. In the Bödewadt flow, the radial pressure, Coriolis and viscous forces are in equilibrium in the far-field but the Coriolis forces decrease towards the boundary layer due to viscous effects. This leads to a radial flow directed inwards and an upward axial flow. The mean flow solution of this flow was found by Bödewadt in 1940, but there were no experimental or theoretical studies until the experimental investigations of Savas (1987). Savas

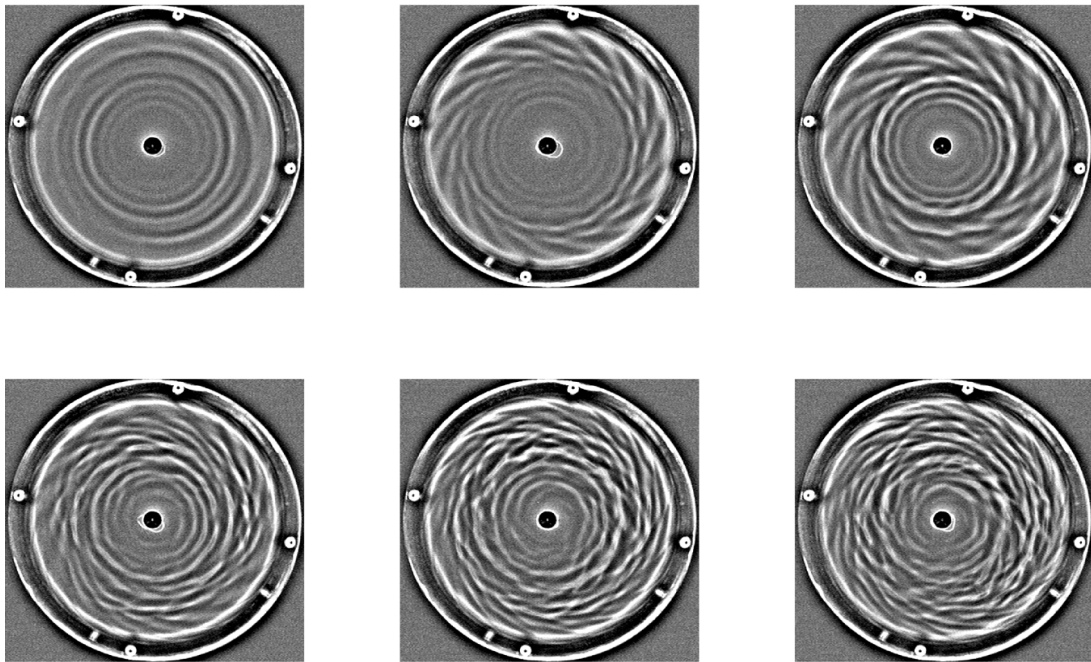


Figure 1.2: Experimental image of the transition process in the Bödewadt flow, reproduced from Cros *et al.* (2005). The angular velocity of the fluid increases from 9rpm to 20rpm, from top left to bottom right and the radius of the disk is  $R = 140$  mm.

reported that the laminar flow was in the form of circular waves at low values of the Reynolds number and found a critical Reynolds number for the onset of stationary vortices to be approximately  $Re = 25$ . This critical Reynolds number is significantly smaller than those of the von Kármán and Ekman flows. Lingwood (1997) conducted a stability analysis for all flows of the BEK system and found the critical Reynolds number of Type I mode to be approximately  $Re = 27$ , which is in good agreement with Savas (1987).

Figure 1.2 shows the transition process of the Bödewadt flow in increased order of Reynolds number and reveals a purely laminar flow in the form of circular wave patterns at low Reynolds numbers. As the Reynolds number increases, the stationary vortices begin to be observed and coexist with these circular waves. After a threshold value of the Reynolds number is reached, the circular waves disappear and the stationary vortices dominate the flow. Increasing the Reynolds number further triggers a transition process to the turbulent state.

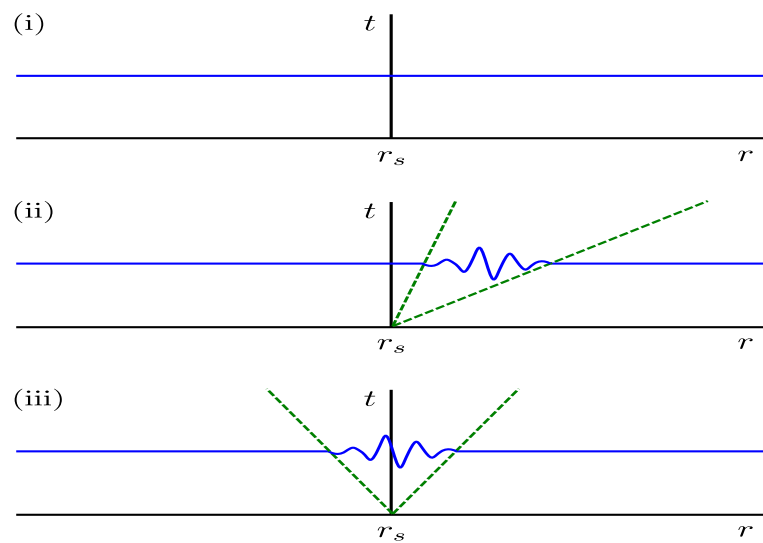


Figure 1.3: Sketch of (i) stable, (ii) convectively unstable and (iii) absolutely unstable disturbances.

A third mode propagating energy towards the centre of the disk was discovered by Mack (1985) for the von Kármán flow. This mode is referred to as the Type III mode and is spatially damped so that it had not been observed in previous studies. The existence of the Type III mode in the broader BEK system was shown by Lingwood (1995). Many authors had assumed that the studies on the rotating disk boundary layer had been complete until the results of Lingwood's studies were published in the mid 1990s. Lingwood used the Briggs-Bers method (Briggs, 1964; Bers, 1975) to show that the coalescence of the Type I and Type III modes leads to an absolute instability regime in the rotating disk flow (Lingwood, 1995, 1996, 1997). The flows are reported as stable or convectively unstable outside of the absolute instability regime.

If a localised disturbance generated by an initial impulse propagates away from the location where it originated both upstream and downstream, the flow is said to be absolutely unstable. In the case the disturbance is swept away from the source either downstream or upstream, the flow is said to be convectively unstable. Figure 1.3 demonstrates the concepts of (i) stability, (ii) convectively instability and (iii) absolute instability. The wave packet in case (ii) sweeps away from the source and grows as it convects. On the other hand, the disturbance spreads both upstream

and downstream of the source while it grows in case (iii).

The local convective - absolute behaviour and global properties of the disturbances have been studied by many authors in a wide range of flow types. The interested reader is referred to Huerre & Monkewitz (1990), Billant *et al.* (1998), Huerre *et al.* (2000), Davies & Carpenter (2003), Chomaz (2004), Healey (2010), Schmid & Henningson (2012) and Imayama *et al.* (2014) for extensive discussions on the subject.

## 1.1. Motivation and aim of the current study

The majority of this thesis is concerned with the effects of surface roughness on the stability characteristics of the BEK system of flows. Interest in the characteristics of laminar-turbulent transition over rough disks has started to increase recently and some valuable contributions have already been made. In the early studies of this area, a small number of roughness elements aligned in particular patterns were used in order to excite some particular disturbance modes in the boundary layer. A well-known example related to those early studies is the theoretical study of Cooper & Carpenter (1997) that analyses the effects of the wall compliance on the stability of the von Kármán flow. The wall compliance was found to be effective in stabilising the inviscid Type I mode, and the effects on the viscous Type II mode were reported as destabilising. This destabilising effect was attributed to increased energy production by viscous forces on the disk surface. Those results were then confirmed by the experimental studies of the Colley *et al.* (1999).

The interest of this thesis is, on the other hand, to analyse the effects of more general distributed surface roughness. A study involving this type of roughness would be the experimental investigation of Watanabe *et al.* (1993) who considered the laminar-turbulent transition of the boundary layer flow over a rotating cone. An indication of the potential stabilising effect of surface roughness was, in this case, shown by reducing the number of vortices from 32 to 26 for a modest level of the surface roughness.

Due to well-known connection between the rotating cone and the rotating disk boundary layers (Garrett *et al.*, 2009; Garrett, 2009), a study on the effects of distributed surface roughness on the transition of the von Kármán flow can be used as the first step towards explaining Watanabe's results. Two alternative models for surface roughness in the von Kármán flow exist in the literature. The first is due to Yoon *et al.* (2007), henceforth referred to as the YHP model. Under the YHP model, surface roughness is modelled by imposing a particular surface distribution as a function of radial position only and assuming a rotational symmetry. Thereby, this model is limited to a particular case of *anisotropic roughness*, namely concentric grooves (radially anisotropic roughness).

An alternative method to the YHP model in the literature is the MW model developed by Miklavcic & Wang (2004). The MW approach models surface roughness empirically instead of imposing a particular mathematical form by converting the usual no-slip boundary conditions to partial-slip conditions at the disk surface. Therefore, independent levels of roughness in the radial and azimuthal directions can be modelled using this approach by separately modifying the boundary conditions in these directions. The MW model can therefore model all variations of distributed roughness that will be used throughout this thesis: *isotropic roughness* (uniform in both directions) and two forms of anisotropic roughness, radial grooves (azimuthally anisotropic) and concentric grooves (radially anisotropic).

Recently, those variations of the distributed surface roughness were considered in the study of Cooper *et al.* (2015) using the MW model on the von Kármán flow. The results obtained reveal that the introduction of surface roughness leads to a stabilisation of the Type I mode in terms of increased critical Reynolds number. However, the study of Garrett *et al.* (2016) for the concentric grooves case reveals parallel results for the Type II mode to that of Garrett *et al.* (2012) such that a significant destabilisation is obtained and the Type II mode becomes the most dangerous mode in terms of critical Reynolds number for higher levels of roughness.

This current study aims to broaden the theoretical studies of the von Kármán flow to flows within the broader BEK system. The principle objective is to under-

stand the effects of distributed surface roughness on the characteristics of the BEK system in terms of the response of the convective instability properties. The work is hoped to contribute to progress towards developing an understanding of *the right sort of roughness*. Therefore, a linear convective instability analyses will be applied to those flows in order to determine curves of neutral stability and produce the convective growth rates. As discussed by Lingwood & Garrett (2011), the absolute instability mechanism limits the computation of the convective growth rate curves in certain flows due to the “branch exchange” issue resulting from the coalescence of the Type I and Type III modes. Therefore, the effect of increased surface roughness on the delaying of the “branch exchange” will also be investigated. In some sense this is a proxy for investigating the onset of absolute instability, but it should be noted that this is not a complete absolute instability analysis which would require an additional, highly focused study.

It also known that the BEK system of flows are convectively unstable within certain regions to *travelling* disturbances. That is, disturbances that are not stationary in the frame of the rotating disk (Lingwood, 1997). It is well known that for smooth disks these travelling disturbances are dominant, but in the case of rough disks, *stationary* disturbances are consistently excited by surface roughnesses fixed in time in the rotating frame and are continually reinforced such that they dominate. For this reason only stationary disturbances are studied in this thesis. The interested reader is referred to the studies of Lingwood (1997), Corke & Knasiak (1998), Othman & Corke (2006) and Corke *et al.* (2007) for comprehensive discussions of the instability characteristics of travelling modes over a rotating disk.

There are two other main drag reduction techniques discussed in the literature and applied to the rotating disk flows in order to delay the onset of the transition process. One of these methods is applying mass transfer at the disk surface. This method has been widely used by many authors since Batchelor (1951) extended the governing equations of the von Kármán flow to rotating disks flows with a uniform axial mass flux at the disk surface. The axial mass flux is satisfied by applying a uniform mass suction or injection. The experimental study of Gregory & Walker

(1960) revealed that controlled surface suction might delay the onset of instability modes. These observations are supported theoretically by the linear stability work of Dhanak (1992) who showed that uniform suction leads to an increase in critical Reynolds numbers of the Type I and Type II modes whereas uniform mass injection has the reverse effect. The same effects of uniform mass flux have been observed for the BEK system of flows in the study of Lingwood & Garrett (2011). For an extensive review of this area of research the reader is referred to Turkyilmazoglu (2009).

Magnetohydrodynamic (MHD) systems are also used as a potential drag reduction technique in the literature. The first application of these systems on rotating disk flows uses the application of a uniform magnetic field to the electrically conducting fluid and is studied by Sparrow & Cess (1962). They revealed that the presence of a magnetic field has a stabilising effect on the flow. Further stability analysis on the von Kármán flow are conducted by Jasmine (2003) and Jasmine & Gajjar (2005). Their findings are in agreement with previous results in the literature. There are many other studies between those works and for a recent and comprehensive review of the area interested reader is referred to Thomas (2007). Where appropriate, the results of this thesis will be discussed in the context of these alternative stabilisation methods.

This thesis is organised as follows: A brief introduction to the BEK system of boundary layer flows is given in Chapter 2. The governing steady mean flow equations are formulated using the MW model and the perturbation equations are presented in the same chapter. The details of the mean flow solver and the spectral Chebyshev methods used to solve those equations are then stated in Chapter 3. Here, the Chebyshev collocation points are transformed into the fluid domain using an exponential transformation mapping to be ensure the accuracy of the approximation inside the boundary layer. The effects of surface roughness generated by azimuthally anisotropic roughness (radial grooves), radially anisotropic roughness (concentric grooves) and isotropic roughness are discussed in Chapters, 4, 5 & 6, respectively. In each of those chapters, the mean flow profiles and convective neutral stability

curves are presented. It is seen that increased radial grooves and isotropic roughness have a great stabilisation effect on both Type I and Type II modes for the BEK system of flows. The only exception is the destabilisation of the Bödewadt flow in the case of increased radial grooves. Increased concentric grooves also has a stabilisation effect on Type I mode, however, it causes destabilisation of the Type II mode. These results are validated by analysing the effects of surface roughness on the most rapidly growing modes that would be most likely to dominate and be observed in experiments. Yet further confirmation is obtained in each case by conducting an energy balance analysis at the location of the maximum amplification of each instability mode. The energy balance approach also enables us to gain an insight into the physics of the stabilisation process. This is then followed by a brief discussion of the absolute instability that focuses on “branch exchange” between the Type I and Type III modes. All findings discussed in those chapters are compared qualitatively to the other drag-reduction techniques mentioned previously. The purpose of the final chapter, Chapter 7, is to compare all findings and make comments on the potential for using surface roughness as a control mechanism for the BEK family of flows. Possible extensions of this work are also discussed.

A considerable amount of the findings presented herein has already been published as Alveroglu *et al.* (2016a) and a second publication will appear shortly in the Proceedings of ISROMAC-16 (Alveroglu *et al.*, 2016b).

# Chapter 2

## The governing equations of the linear stability analysis

### 2.1. Overview

Analysing the response of a laminar flow to a perturbation of small amplitude is one of the main challenges of stability theory. A flow could be defined as stable if it returns to its original laminar state after suffering some perturbation. However if the perturbation grows and leads to the transition of the laminar state into a different state, the flow can be defined as unstable. Mathematically, stability theory is concerned with the evolution of superposed perturbations on the laminar base flow. By assuming the perturbations to be small, further simplifications can be justified and linear equations governing the growth of the perturbation can be achieved. However, those linear equations lose their validity as the perturbations grow above a few percent of the base flow and nonlinear interactions begin to occur. Despite the limited region of validity, the linear equations are important to determine physical growth mechanisms and dominant disturbances types (Schmid & Henningson, 2012).

In this chapter, a brief description of the BEK family of boundary layers is given in §2.2, and the derivation of nonlinear steady mean flow equations governing the laminar base flows of the BEK system flows are outlined in §2.3.1. In §2.3.2 the derivation of the perturbation equations is presented. A derivation of the energy

balance equations is included in §2.3.3.

## 2.2. A brief description of the BEK flows

This study is concerned with the BEK family of boundary layers, referred to as the BEK system for simplicity throughout the thesis. The BEK system of flows is generated by a two rotating disk system in which the lower and upper disks rotate around a common axis in an otherwise still, incompressible fluid. The flows are then distinguished by a differential rotation rate between the lower disk and the fluid above which is generated by the upper rotating disk. The angular velocities of the lower disk and the fluid above are denoted by  $\Omega_D^*$  and  $\Omega_F^*$  indicating the disk  $D$  and flow  $F$ , respectively.

The BEK system includes the Bödewadt, Ekman and von Kármán flows as the main particular cases. Between these particular cases, there are flows in which both the disk and the fluid rotate with different angular velocities. The von Kármán flow occurs in the case of a rotational lower disk and a stationary upper fluid, i.e.  $\Omega_D^* \neq 0$  and  $\Omega_F^* = 0$ ; whereas the Ekman flow occurs in the case of both lower disk and upper fluid rotate with the same angular velocity in the same direction, i.e.  $\Omega_D^* = \Omega_F^* \neq 0$ . The Bödewadt flow occurs in the case of a stationary lower disk and a rotating upper flow, i.e.  $\Omega_D^* = 0$  and  $\Omega_F^* \neq 0$ . It is also assumed that the lower disk is to be rotating in a frame of reference that rotates with the disk. As a result, the Coriolis terms and centrifugal effects due to rotation appear in the governing equations. The existence of those Coriolis terms leads to use of the Rossby number to distinguish the flows in the system. The Rossby number is a constant parameter of the flow relating the ratio of Coriolis forces to inertial forces and can be defined as

$$Ro = \frac{\Omega_F^* - \Omega_D^*}{\Omega^*}, \quad (2.1)$$

where  $\Omega^*$  is the system rotation rate and defined as

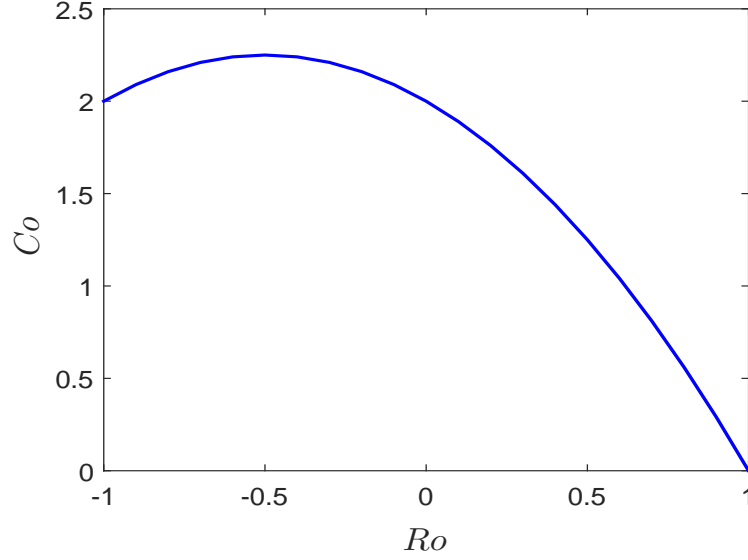


Figure 2.1: Variation in  $Co$  with  $Ro$  for the BEK system flows

$$\Omega^* = \frac{\Omega_F^*}{2 - Ro} + \frac{\Omega_D^*}{2 + Ro} = \frac{\Omega_F^* + \Omega_D^*}{4} + \left( \left( \frac{\Omega_F^* + \Omega_D^*}{4} \right)^2 + \frac{(\Omega_F^* - \Omega_D^*)^2}{2} \right)^{1/2}.$$

The Rossby number for the BEK system of flows has a range from negative unity to positive unity, i.e.,  $Ro \in [-1, 1]$ . Furthermore, the constant parameter Coriolis number is related to the Rossby number such that

$$Co = 2\Omega_D^*/\Omega^* = 2 - Ro - Ro^2.$$

Figure 2.1 shows  $Co$  plotted against  $Ro$  and a classification of the BEK family of boundary layer flows in terms of those parameters is stated in the study of Lingwood & Garrett (2011) as

Bödewadt flow:	$Ro = 1$	$Co = 0$	$\Omega^* = \Omega_F^*$
Ekman flow:	$Ro = 0$	$Co = 2$	$\Omega^* = \Omega_F^* = \Omega_D^*$
Von Kármán:	$Ro = -1$	$Co = 2$	$\Omega^* = \Omega_D^*$ .

## 2.3. Derivation of the governing equations

In the derivation of the governing equations for the steady mean flow and perturbation equations of the BEK system, the dimensional Navier-Stokes equations are used in a cylindrical polar coordinate system  $(r^*, \theta, z^*)$ . Furthermore, we assume an incompressible flow. The momentum equations are given in (2.2) and the continuity equation is given in (2.3)

$$\begin{aligned} \frac{\partial U^*}{\partial t^*} + \mathbf{U}^* \cdot \nabla U^* - \frac{V^{*2}}{r^*} - 2\Omega_D^* V^* \\ = -\frac{1}{\rho^*} \frac{\partial P^*}{\partial r^*} + \nu^* \left( \nabla^2 U^* - \frac{U^*}{r^{*2}} - \frac{2}{r^{*2}} \frac{\partial V^*}{\partial \theta} \right), \end{aligned} \quad (2.2)$$

$$\begin{aligned} \frac{\partial V^*}{\partial t^*} + \mathbf{U}^* \cdot \nabla V^* + \frac{U^* V^*}{r^*} + 2\Omega_D^* U^* \\ = -\frac{1}{r^* \rho^*} \frac{\partial P^*}{\partial \theta} + \nu^* \left( \nabla^2 V^* + \frac{2}{r^{*2}} \frac{\partial U^*}{\partial \theta} - \frac{V^*}{r^{*2}} \right), \end{aligned}$$

$$\frac{\partial W^*}{\partial t^*} + \mathbf{U}^* \cdot \nabla W^* = -\frac{1}{\rho^*} \frac{\partial P^*}{\partial z^*} + \nu^* \nabla^2 W^*,$$

$$\frac{\partial U^*}{\partial r^*} + \frac{U^*}{r^*} + \frac{1}{r^*} \frac{\partial V^*}{\partial \theta} + \frac{\partial W^*}{\partial z^*} = 0. \quad (2.3)$$

Here, the asterisk superscript denotes the dimensional form of the quantities and  $\mathbf{U}^* = (U^*, V^*, W^*)$  in which  $U^*$ ,  $V^*$  &  $W^*$  are the radial, azimuthal and axial velocity components, respectively. Furthermore,  $P^*$  is the fluid pressure,  $\nu^*$  is the kinematic viscosity,  $\rho^*$  is the density of the fluid and  $t^*$  is time.

### 2.3.1. The steady mean flows

In the derivation of the steady mean flow equations, an axisymmetric mean flow assumption is made. Therefore, the mean flow components and pressure term are independent of axial direction  $\theta$ . The Navier-stokes equations (2.2)-(2.3) can be

written explicitly using this assumption as

$$\begin{aligned} U^* \frac{\partial U^*}{\partial r^*} + W^* \frac{\partial U^*}{\partial z^*} - \frac{V^{*2}}{r^*} - 2\Omega_D^* V^* \\ = -\frac{1}{\rho^*} \frac{\partial P^*}{\partial r^*} + \nu^* \left( \frac{\partial^2 U^*}{\partial r^{*2}} + \frac{1}{r^*} \frac{\partial U^*}{\partial r^*} + \frac{\partial^2 U^*}{\partial z^{*2}} - \frac{U^*}{r^{*2}} \right), \end{aligned} \quad (2.4)$$

$$\begin{aligned} U^* \frac{\partial V^*}{\partial r^*} + W^* \frac{\partial V^*}{\partial z^*} + \frac{U^* V^*}{r^*} + 2\Omega_D^* U^* \\ = \nu^* \left( \frac{\partial^2 V^*}{\partial r^{*2}} + \frac{V^*}{r^*} + \frac{\partial^2 V^*}{\partial z^{*2}} - \frac{V^*}{r^{*2}} \right), \end{aligned} \quad (2.5)$$

$$U^* \frac{\partial W^*}{\partial r^*} + W^* \frac{\partial W^*}{\partial z^*} = -\frac{1}{\rho^*} \frac{\partial P^*}{\partial z^*} + \nu^* \left( \frac{\partial^2 W^*}{\partial r^{*2}} + \frac{W^*}{r^*} + \frac{\partial^2 W^*}{\partial z^{*2}} \right), \quad (2.6)$$

$$\frac{\partial U^*}{\partial r^*} + \frac{U^*}{r^*} + \frac{\partial W^*}{\partial z^*} = 0. \quad (2.7)$$

To obtain the dimensionless form of these equations, global similarity variables that extend the exact similarity solution of the Navier-Stokes equations for the von Kármán flow, and used by Lingwood (1997), amongst others, are used here. These dimensionless mean flow variables are assumed to have the following form:

$$U(z) = \frac{U^*}{r^* \Omega^* Ro}, \quad V(z) = \frac{V^*}{r^* \Omega^* Ro}, \quad (2.8)$$

$$W(z) = \frac{W^*}{l^* \Omega^* Ro}, \quad P(r, z) = \frac{P^*}{\rho^* l^{*2} \Omega^{*2} Ro^2},$$

where  $l^* = \sqrt{\nu^*/\Omega^*}$  is the boundary layer thickness. Moreover,  $z = z^*/l^*$  and  $r = r^*/l^*$  are the dimensionless forms of  $z^*$  and  $r^*$ , respectively. The dimensionless Reynolds number is given as

$$Re = \frac{r^* \Delta \Omega^* l^*}{\nu^*} = r^* \frac{Ro \Omega^*}{\nu^*} l^* = r^* \frac{1}{l^{*2}} l^* Ro = \frac{r^*}{l^*} Ro = r Ro. \quad (2.9)$$

Here,  $\Delta \Omega^* = \Omega_F^* - \Omega_D^*$  and  $\Delta \Omega^* = Ro \Omega^*$  from the definition (2.1).

Differentiations of the dimensional mean flow velocity components  $U^*$ ,  $V^*$ ,  $W^*$  and the pressure term  $P^*$  are then stated in terms of the dimensionless mean flow variables as

$$\begin{aligned}
\frac{\partial U^*}{\partial r^*} &= \frac{\partial}{\partial r^*} \left( U(z) r^* \Omega^* Ro \right) = \Omega^* Ro U(z), & \frac{\partial U^*}{\partial z^*} &= \frac{r^* \Omega^* Ro}{l^*} U'(z), \\
\frac{\partial^2 U^*}{\partial r^{*2}} &= \frac{\partial^2}{\partial r^{*2}} \left( U(z) r^* \Omega^* Ro \right) = 0, & \frac{\partial^2 U^*}{\partial z^{*2}} &= \frac{r^* \Omega^* Ro}{l^{*2}} U''(z), \\
\frac{\partial V^*}{\partial r^*} &= \frac{\partial}{\partial r^*} \left( V(z) r^* \Omega^* Ro \right) = \Omega^* Ro V(z), & \frac{\partial V^*}{\partial z^*} &= \frac{r^* \Omega^* Ro}{l^*} V'(z), \\
\frac{\partial^2 V^*}{\partial r^{*2}} &= \frac{\partial^2}{\partial r^{*2}} \left( V(z) r^* \Omega^* Ro \right) = 0, & \frac{\partial^2 V^*}{\partial z^{*2}} &= \frac{r^* \Omega^* Ro}{l^{*2}} V''(z), \\
\frac{\partial W^*}{\partial r^*} &= \frac{\partial}{\partial r^*} \left( W(z) l^* \Omega^* Ro \right) = 0, & \frac{\partial W^*}{\partial z^*} &= \Omega^* Ro W'(z), \\
\frac{\partial^2 W^*}{\partial r^{*2}} &= \frac{\partial^2}{\partial r^{*2}} \left( W(z) l^* \Omega^* Ro \right) = 0, & \frac{\partial^2 W^*}{\partial z^{*2}} &= \frac{\Omega^* Ro}{l^*} W''(z).
\end{aligned} \tag{2.10}$$

The radial pressure gradient that appears in (2.4) should be determined from the relative circumferential flow as  $z \rightarrow \infty$ , i.e,  $V \rightarrow 1$ . Using the assumptions  $U(z) \rightarrow 0$ ,  $U'(z) \rightarrow 0$  and  $U''(z) \rightarrow 0$  as  $z \rightarrow \infty$  gives

$$Ro + Co = \frac{1}{\rho^* \Omega^{*2} r^* Ro} \frac{\partial P^*}{\partial r^*}, \tag{2.11}$$

that is taken as a constant in  $z$ . Therefore, the mean pressure term can be written as

$$P^*(r, z) = \rho^* \Omega^{*2} l^{*2} Ro^2 \left( \frac{r^2 (Ro + Co)}{2Ro} + P(z) + \text{constant} \right). \tag{2.12}$$

It follows that

$$\frac{\partial P^*}{\partial z^*} = P'(z) \rho^* \Omega^{*2} l^* Ro^2. \tag{2.13}$$

The dimensionless steady mean flow equations are then obtained using the cor-

responding terms in (2.10)-(2.13). The radial component of the dimensional Navier-Stokes equations, (2.4), can be expressed as

$$\begin{aligned} r^* \Omega^{*2} Ro^2 \left\{ U^2(z) + W(z)U'(z) - V^2(z) \right\} - 2\Omega_D^* r^* \Omega^* Ro V(z) \\ = -\frac{1}{\rho^*} \frac{\partial P^*}{\partial r^*} + \left( \frac{\nu^* \Omega^* Ro}{r^*} U(z) + \frac{\nu^* r^* \Omega^* Ro}{l^{*2}} U''(z) - \frac{\nu^* \Omega^* Ro}{r^*} U(z) \right). \end{aligned}$$

Dividing each term of this equation by  $\frac{\nu^* r^* \Omega^* Ro}{l^{*2}}$  and using (2.11) gives

$$Ro \left( U^2 + WU' - V^2 \right) - CoV = Ro + Co - U'',$$

as  $Co = \frac{2\Omega_D^*}{\Omega^*}$  and  $\frac{\nu^*}{l^{*2}} = \Omega^*$ . Therefore, the radial equation for the dimensionless mean flow is

$$Ro \left( U^2 + U'W - (V^2 - 1) \right) - Co(V - 1) - U'' = 0. \quad (2.14)$$

Similarly, the azimuthal component of the dimensional Navier-Stokes equations, (2.5), can be expressed, using the dimensionless components, as

$$\begin{aligned} r^* \Omega^{*2} Ro^2 \left\{ U(z)V(z) + W(z)V'(z) + U(z)V(z) \right\} + 2\Omega_D^* r^* \Omega^* Ro U(z) \\ = \left( \frac{\nu^* \Omega^* Ro}{r^*} V(z) + \frac{\nu^* r^* \Omega^* Ro}{l^{*2}} V''(z) - \frac{\nu^* \Omega^* Ro}{r^*} V(z) \right). \end{aligned}$$

Dividing each side of this equation by  $\frac{\nu^* r^* \Omega^* Ro}{l^{*2}}$  leads to the dimensionless azimuthal steady mean flow equation

$$Ro \left( 2UV + WV' \right) + CoU - V'' = 0. \quad (2.15)$$

The axial component of the dimensional Navier-Stokes equations, (2.6), is expressed as

$$l^* \Omega^{*2} Ro^2 W(z)W'(z) = -\frac{1}{\rho^*} \rho^* \Omega^{*2} l^* Ro^2 P'(z) + \frac{\nu^* \Omega^* Ro}{l^*} W''(z).$$

Dividing each term by  $\frac{\nu^* \Omega^* Ro}{l^*}$  leads to the dimensionless axial equation for the steady mean flow

$$Ro \left( WW' + P' \right) - W'' = 0. \quad (2.16)$$

The dimensional continuity equation (2.7) is expressed as

$$\Omega^* Ro U(z) + \frac{r^* \Omega^* Ro}{r^*} U(Z) + \Omega^* Ro W'(z) = 0,$$

which directly implies that the dimensionless continuity equation of the steady mean flow is

$$2U + W' = 0. \quad (2.17)$$

The obtained dimensionless mean flow equations for the BEK system flows are then stated as

$$\begin{aligned} Ro \left( U^2 + U'W - (V^2 - 1) \right) - Co \left( V - 1 \right) - U'' &= 0, \\ Ro \left( 2UV + V'W \right) + CoU - V'' &= 0, \\ Ro \left( WW' + P' \right) - W'' &= 0, \\ 2U + W' &= 0. \end{aligned} \quad (2.18)$$

In the above all derivatives denoted by primes are with respect to  $z$ , and  $U$ ,  $V$  &  $W$  are the mean flow components in radial, azimuthal and axial directions, the pressure term is denoted by  $P$ .

The boundary conditions at the lower rough disk surface in the BEK system are derived from the MW approach proposed in the study of Miklavcic & Wang (2004). That is, the surface roughness is modelled empirically using partial-slip conditions at the disk surface instead of the usual no-slip condition proposed by Navier (1827). However, the far-field boundary conditions at the upper edge of the boundary layer are identical to the no-slip condition at infinity. These partial-slip

boundary conditions are

$$\begin{aligned} U(0) &= \lambda U'(0), & V(0) &= \eta V'(0) & \text{and} & & W(0) &= 0, \\ U &\longrightarrow 0, & V &\longrightarrow 1, & \text{as} & & z &\longrightarrow \infty. \end{aligned} \quad (2.19)$$

Note that the derivatives (indicated with a prime) are again with respect to  $z$  and the two parameters  $\eta$  and  $\lambda$  are empirical values related to experimental measures of roughness in the *radial* and *azimuthal* directions, respectively. The no-slip boundary conditions for a smooth disk are established at  $\lambda = \eta = 0$ . The particular cases  $\eta > 0$ ,  $\lambda = 0$  (concentric grooves) and  $\eta = 0$ ,  $\lambda > 0$  (radial grooves) correspond to *anisotropic* roughness, *radially* and *azimuthally*, whereas the case  $\eta = \lambda \neq 0$  corresponds to *isotropic* roughness. The effects of these types of roughness on the instability properties of the BEK system of flows are studied individually in the later chapters of this thesis. The conditions are further discussed in Cooper *et al.* (2015).

In the case of the Ekman flow,  $Ro = 0$ , it should be noted that there is a precise analytical solution of equations (2.18) for the velocity components subject to boundary conditions (2.19) at general  $\eta$  and  $\lambda$  and it is stated in (2.20). The pressure term  $P$  is not required to perform the stability analysis, as discussed later. Therefore, an analytic solution for this term is not presented here

$$\begin{aligned} U &= e^{-z}(A \sin z - B \cos z), \\ V &= 1 + e^{-z}(B \sin z + A \cos z), \\ W &= e^{-z}[B(\sin z - \cos z) + A(\sin z + \cos z)] + B - A, \end{aligned} \quad (2.20)$$

where  $A$  and  $B$  are constants given by

$$A = -\frac{1 + \lambda}{(1 + \lambda)(1 + \eta) + \lambda\eta}, \quad \text{and} \quad B = \frac{\lambda}{(1 + \lambda)(1 + \eta) + \lambda\eta}.$$

Of physical interest is the resisting torque  $T$  on the lower disk as given by

$$T = \int_0^R \nu V'(0) 2\pi r^2 dr = \frac{2\pi\nu}{3} \frac{Re^3}{Ro^3} V'(0), \quad (2.21)$$

(Miklavcic & Wang, 2004). Here,  $R$  is radius of the disk and  $r$  is replaced with  $Re/Ro$  using the dimensionless Reynolds number (2.9).

### 2.3.2. Derivation of the perturbation equations

In the derivation of perturbation equations, the dimensional Navier-Stokes equations (2.2)-(2.3) are used. The equations are non-dimensionalised with respect to the local similarity variables based on a local radial position of the disk,  $r_a$ . The local similarity variables are

$$\begin{aligned} U(z) &= \frac{U^*}{r_a^* \Omega^* Ro}, & V(z) &= \frac{V^*}{r_a^* \Omega^* Ro}, & W(z) &= \frac{W^*}{r_a^* \Omega^* Ro}, \\ P(r, z) &= \frac{P^*}{\rho^* r_a^{*2} \Omega^{*2} Ro^2}, & t &= \frac{t^*}{l^*/(r_a^* \Omega^* Ro)}, & \text{and} & & r &= r_a^*/l^*. \end{aligned} \quad (2.22)$$

The non-dimensional Reynolds number in terms of local scales is given as

$$Re = \frac{r_a^* \Delta \Omega^* l^*}{\nu^*} = r_a Ro. \quad (2.23)$$

The local Reynolds number is therefore negative for a negative Rossby number, however this is merely a consequence of using a single model for positive and negative Rossby number flows. The results will therefore be presented in terms of positive  $Re$  throughout this dissertation.

The dimensionless velocity and pressure of a perturbed flow are denoted by bared lower-case quantities. To derive the perturbation equations, each of those quantities are decomposed into dimensionless mean flow and perturbation parts. The mean flow and perturbation parts are denoted by upper-case and lower-case quantities, respectively. The expansions are as follows

$$\begin{aligned} \bar{u}(r, \theta, z, t) &= \frac{r Ro}{Re} U(z) + u(r, \theta, z, t) \\ \bar{v}(r, \theta, z, t) &= \frac{r Ro}{Re} V(z) + v(r, \theta, z, t) \\ \bar{w}(r, \theta, z, t) &= \frac{Ro}{Re} W(z) + w(r, \theta, z, t) \\ \bar{p}(r, \theta, z, t) &= \frac{Ro^2}{Re^2} P(z) + p(r, \theta, z, t). \end{aligned} \quad (2.24)$$

It is also assumed throughout this dissertation that the imposed disturbances are sufficiently small so that the transition process is controlled by the primary stability of the mean flow instead of any secondary instability that can occur if the perturbations are large enough to deform the mean flow profiles. Furthermore, the non-linear terms arising from products of these small perturbation quantities are also sufficiently small to be ignored in the equations. In other words, a linear analysis is conducted. Note that bypass transition in which the initial perturbations are large enough such that non-linear terms dominate the flow from the very beginning are not considered here.

In order to obtain the dimensionless perturbation equations, the local similarity variables (2.22) are firstly inserted in equations (2.2)-(2.3). Then, using the perturbed flow components (2.24), and having scaled the dimensional differential operators, we find that

$$\begin{aligned}
& \frac{r_a^{*2} \Omega^{*2} Ro^2}{l^*} \left\{ \frac{\partial}{\partial t} \left( \frac{rRo}{Re} U(z) + u(r, \theta, z, t) \right) \right. \\
& \quad + \left( \frac{rRo}{Re} U(z) + u(r, \theta, z, t) \right) \frac{\partial}{\partial r} \left( \frac{rRo}{Re} U(z) + u(r, \theta, z, t) \right) \\
& \quad + \frac{1}{r} \left( \frac{rRo}{Re} V(z) + v(r, \theta, z, t) \right) \frac{\partial}{\partial \theta} \left( \frac{rRo}{Re} U(z) + u(r, \theta, z, t) \right) \\
& \quad + \left( \frac{Ro}{Re} W(z) + w(r, \theta, z, t) \right) \left( \frac{rRo}{Re} U'(z) + \frac{\partial u(r, \theta, z, t)}{\partial z} \right) \\
& \quad \left. - \frac{1}{r} \left( \frac{rRo}{Re} V(z) + v(r, \theta, z, t) \right)^2 \right\} - 2\Omega_D^* r_a^* \Omega^* Ro \left( \frac{rRo}{Re} V(z) + v(r, \theta, z, t) \right) \\
& = -\frac{r_a^{*2} \Omega^{*2} Ro^2}{l^*} \frac{\partial}{\partial r} \left( \frac{Ro^2}{Re^2} P(z) + p(r, \theta, z, t) \right) + \frac{\nu^* r_a^* \Omega^* Ro}{l^{*2}} \left\{ \frac{\partial^2}{\partial r^2} \left( \frac{rRo}{Re} U(z) + u(r, \theta, z, t) \right) \right. \\
& \quad + \frac{1}{r} \frac{\partial}{\partial r} \left( \frac{rRo}{Re} U(z) + u(r, \theta, z, t) \right) + \frac{1}{r^2} \frac{\partial^2}{\partial r^2} \left( \frac{rRo}{Re} U(z) + u(r, \theta, z, t) \right) \\
& \quad \left. + \frac{\partial^2}{\partial z^2} \left( \frac{rRo}{Re} U(z) + u(r, \theta, z, t) \right) - \frac{1}{r^2} \left( \frac{rRo}{Re} U(z) + u(r, \theta, z, t) \right) \right\}
\end{aligned}$$

$$- \frac{2}{r^2} \frac{\partial}{\partial \theta} \left( \frac{rRo}{Re} U(z) + u(r, \theta, z, t) \right) \Bigg\}, \quad (2.25)$$

$$\begin{aligned} & \frac{r_a^{*2} \Omega^{*2} Ro^2}{l^*} \left\{ \frac{\partial}{\partial t} \left( \frac{rRo}{Re} V(z) + v(r, \theta, z, t) \right) \right. \\ & + \left( \frac{rRo}{Re} U(z) + u(r, \theta, z, t) \right) \frac{\partial}{\partial r} \left( \frac{rRo}{Re} V(z) + v(r, \theta, z, t) \right) \\ & + \frac{1}{r} \left( \frac{rRo}{Re} V(z) + v(r, \theta, z, t) \right) \frac{\partial}{\partial \theta} \left( \frac{rRo}{Re} V(z) + v(r, \theta, z, t) \right) \\ & + \left( \frac{Ro}{Re} W(z) + w(r, \theta, z, t) \right) \left( \frac{rRo}{Re} V'(z) + \frac{\partial v(r, \theta, z, t)}{\partial z} \right) \\ & \left. + \frac{1}{r} \left( \frac{rRo}{Re} U(z) + u(r, \theta, z, t) \right) \left( \frac{rRo}{Re} V(z) + v(r, \theta, z, t) \right) \right\} \\ & + 2\Omega_D^* r_a^* \Omega^* Ro \left( \frac{rRo}{Re} U(z) + u(r, \theta, z, t) \right) \\ = & - \frac{r_a^{*2} \Omega^{*2} Ro^2}{l^* r} \frac{\partial}{\partial \theta} \left( \frac{Ro^2}{Re^2} P(z) + p(r, \theta, z, t) \right) + \frac{\nu^* r_a^* \Omega^* Ro}{l^{*2}} \left\{ \frac{\partial^2}{\partial r^2} \left( \frac{rRo}{Re} V(z) + v(r, \theta, z, t) \right) \right. \\ & + \frac{1}{r} \frac{\partial}{\partial r} \left( \frac{rRo}{Re} V(z) + v(r, \theta, z, t) \right) + \frac{1}{r^2} \frac{\partial^2}{\partial r^2} \left( \frac{rRo}{Re} V(z) + v(r, \theta, z, t) \right) \\ & + \frac{\partial^2}{\partial z^2} \left( \frac{rRo}{Re} V(z) + v(r, \theta, z, t) \right) - \frac{1}{r^2} \left( \frac{rRo}{Re} V(z) + v(r, \theta, z, t) \right) \\ & \left. + \frac{2}{r^2} \frac{\partial}{\partial \theta} \left( \frac{rRo}{Re} V(z) + v(r, \theta, z, t) \right) \right\}, \quad (2.26) \end{aligned}$$

$$\frac{r_a^{*2} \Omega^{*2} Ro^2}{l^*} \left\{ \frac{\partial}{\partial t} \left( \frac{Ro}{Re} W(z) + w(r, \theta, z, t) \right) \right.$$

$$\begin{aligned}
& + \left( \frac{rRo}{Re} U(z) + u(r, \theta, z, t) \right) \frac{\partial}{\partial r} \left( \frac{Ro}{Re} W(z) + w(r, \theta, z, t) \right) \\
& + \frac{1}{r} \left( \frac{rRo}{Re} V(z) + v(r, \theta, z, t) \right) \frac{\partial}{\partial \theta} \left( \frac{Ro}{Re} W(z) + w(r, \theta, z, t) \right) \\
& + \left( \frac{Ro}{Re} W(z) + w(r, \theta, z, t) \right) \left( \frac{rRo}{Re} W'(z) + \frac{\partial w(r, \theta, z, t)}{\partial z} \right) \\
= & - \frac{r_a^{*2} \Omega^{*2} Ro^2}{l^*} \frac{\partial}{\partial z} \left( \frac{Ro^2}{Re^2} P(z) + p(r, \theta, z, t) \right) \\
& + \frac{\nu^* r_a^* \Omega^* Ro}{l^{*2}} \left\{ \frac{\partial^2}{\partial r^2} \left( \frac{Ro}{Re} W(z) + w(r, \theta, z, t) \right) + \frac{1}{r} \frac{\partial}{\partial r} \left( \frac{Ro}{Re} W(z) + w(r, \theta, z, t) \right) \right. \\
& \left. + \frac{1}{r^2} \frac{\partial^2}{\partial r^2} \left( \frac{Ro}{Re} W(z) + w(r, \theta, z, t) \right) + \frac{\partial^2}{\partial z^2} \left( \frac{Ro}{Re} W(z) + w(r, \theta, z, t) \right) \right\}, \tag{2.27}
\end{aligned}$$

$$\begin{aligned}
& \frac{r_a^* \Omega^* Ro}{l^*} \left\{ \frac{\partial}{\partial r} \left( \frac{rRo}{Re} U(z) + u(r, \theta, z, t) \right) + \frac{1}{r} \left( \frac{rRo}{Re} U(z) + u(r, \theta, z, t) \right) \right. \\
& \left. + \frac{1}{r} \frac{\partial}{\partial \theta} \left( \frac{rRo}{Re} V(z) + v(r, \theta, z, t) \right) + \frac{\partial^2}{\partial z^2} \left( \frac{Ro}{Re} W(z) + w(r, \theta, z, t) \right) \right\} = 0. \tag{2.28}
\end{aligned}$$

Applying the differentiations and linearisation with respect to perturbation quantities in equations (2.25)-(2.28) and subtracting the mean flow components gives following equations

$$\begin{aligned}
& \frac{r_a^{*2} \Omega^{*2} Ro^2}{l^*} \left\{ \frac{\partial u}{\partial t} + \frac{rRoU}{Re} \frac{\partial u}{\partial r} + \frac{RoU}{Re} u + \frac{RoV}{Re} \frac{\partial u}{\partial \theta} + \frac{RoW}{Re} \frac{\partial u}{\partial z} - \frac{2RoV}{Re} v + \frac{rRoU'w}{Re} \right\} \\
& - 2\Omega_D^* r_a^* Rov \\
= & - \frac{r_a^{*2} \Omega^{*2} Ro^2}{l^*} \frac{\partial p}{\partial r} + \frac{\nu^* r_a^* \Omega^* Ro}{l^{*2}} \left\{ \frac{\partial^2 u}{\partial r^2} + \frac{1}{r^2} \frac{\partial^2 u}{\partial \theta^2} + \frac{\partial^2 u}{\partial z^2} - \frac{u}{r^2} - \frac{u}{r^2} - \frac{2}{r^2} \frac{\partial v}{\partial \theta} \right\}, \tag{2.29}
\end{aligned}$$

$$\begin{aligned}
& \frac{r_a^{*2} \Omega^{*2} Ro^2}{l^*} \left\{ \frac{\partial v}{\partial t} + \frac{r RoU}{Re} \frac{\partial v}{\partial r} + \frac{RoU}{Re} v + \frac{RoV}{Re} \frac{\partial v}{\partial \theta} + \frac{RoW}{Re} \frac{\partial v}{\partial z} + \frac{2RoV}{Re} u + \frac{r RoV' w}{Re} \right\} \\
& + 2\Omega_D^* r_a^* Ro u \\
& = -\frac{r_a^{*2} \Omega^{*2} Ro^2}{l^* r} \frac{\partial p}{\partial \theta} + \frac{\nu^* r_a^* \Omega^* Ro}{l^{*2}} \left\{ \frac{\partial^2 v}{\partial r^2} + \frac{1}{r^2} \frac{\partial^2 v}{\partial \theta^2} + \frac{\partial^2 v}{\partial z^2} - \frac{v}{r^2} - \frac{v}{r^2} + \frac{2}{r^2} \frac{\partial u}{\partial \theta} \right\}, \tag{2.30}
\end{aligned}$$

$$\begin{aligned}
& \frac{r_a^{*2} \Omega^{*2} Ro^2}{l^*} \left\{ \frac{\partial w}{\partial t} + \frac{r RoU}{Re} \frac{\partial w}{\partial r} + \frac{RoW'}{Re} w + \frac{RoV}{Re} \frac{\partial w}{\partial \theta} + \frac{RoW}{Re} \frac{\partial w}{\partial z} \right\} \\
& = \frac{r_a^{*2} \Omega^{*2} Ro^2}{l^*} \frac{\partial p}{\partial z} + \frac{\nu^* r_a^* \Omega^* Ro}{l^{*2}} \left\{ \frac{\partial^2 w}{\partial r^2} + \frac{1}{r^2} \frac{\partial^2 w}{\partial \theta^2} + \frac{\partial^2 w}{\partial z^2} + \frac{w}{r} \right\}, \tag{2.31}
\end{aligned}$$

$$\frac{r_a^* \Omega^* Ro}{l^*} \left\{ \frac{\partial u}{\partial r} + \frac{u}{r} + \frac{1}{r} \frac{\partial v}{\partial \theta} + \frac{\partial^2 w}{\partial z^2} \right\} = 0. \tag{2.32}$$

Equations (2.33)-(2.35) are obtained after dividing each term of the equations (2.29)-(2.31) with  $\frac{r_a^{*2} \Omega^{*2} Ro^2}{l^*}$ . It should be noted that  $\frac{\nu^*}{l^{*2}} = \Omega^*$ ,  $Co = \frac{2\Omega_D^*}{\Omega^*}$  and

$$\frac{\nu^* r_a^* \Omega^* Ro}{l^*} \bigg/ \frac{r_a^{*2} \Omega^{*2} Ro^2}{l^{*2}} = \frac{\nu^*}{r_a^* l^* \Omega^* Ro} = \frac{\nu^*}{l^{*2} \Omega^* r_a Ro} = \frac{1}{Re},$$

Equation (2.36) is, on the other hand, obtained directly from (2.32).

$$\begin{aligned}
& \frac{\partial u}{\partial t} + \frac{r RoU}{Re} \frac{\partial u}{\partial r} + \frac{RoU}{Re} u + \frac{RoV}{Re} \frac{\partial u}{\partial \theta} + \frac{RoW}{Re} \frac{\partial u}{\partial z} - \left( \frac{2RoV}{Re} + \frac{Co}{Re} \right) v + \frac{r RoU' w}{Re} \\
& = -\frac{\partial p}{\partial r} + \frac{1}{Re} \left( \frac{\partial^2 u}{\partial r^2} + \frac{1}{r^2} \frac{\partial^2 u}{\partial \theta^2} + \frac{\partial^2 u}{\partial z^2} - \frac{u}{r^2} - \frac{2}{r^2} \frac{\partial v}{\partial \theta} \right), \tag{2.33}
\end{aligned}$$

$$\begin{aligned}
& \frac{\partial v}{\partial t} + \frac{r RoU}{Re} \frac{\partial v}{\partial r} + \frac{RoU}{Re} v + \frac{RoV}{Re} \frac{\partial v}{\partial \theta} + \frac{RoW}{Re} \frac{\partial v}{\partial z} + \left( \frac{2RoV}{Re} + \frac{Co}{Re} \right) u + \frac{r RoV' w}{Re} \\
& = -\frac{1}{Re} \frac{\partial p}{\partial \theta} + \frac{1}{Re} \left( \frac{\partial^2 v}{\partial r^2} + \frac{1}{r^2} \frac{\partial^2 v}{\partial \theta^2} + \frac{\partial^2 v}{\partial z^2} - \frac{v}{r^2} + \frac{2}{r^2} \frac{\partial u}{\partial \theta} \right), \tag{2.34}
\end{aligned}$$

$$\begin{aligned}
& \frac{\partial w}{\partial t} + \frac{r RoU}{Re} \frac{\partial w}{\partial r} + \frac{RoW'}{Re} w + \frac{RoV}{Re} \frac{\partial w}{\partial \theta} + \frac{RoW}{Re} \frac{\partial w}{\partial z} \\
& = \frac{\partial p}{\partial z} + \frac{1}{Re} \left( \frac{\partial^2 w}{\partial r^2} + \frac{1}{r^2} \frac{\partial^2 w}{\partial \theta^2} + \frac{\partial^2 w}{\partial z^2} + \frac{1}{r} \frac{\partial w}{\partial r} \right), \tag{2.35}
\end{aligned}$$

$$\frac{\partial u}{\partial r} + \frac{u}{r} + \frac{1}{r} \frac{\partial v}{\partial \theta} + \frac{\partial w}{\partial z} = 0. \quad (2.36)$$

In order to make these linearised equations separable in  $r$ ,  $\theta$  and  $t$  a parallel-flow approximation is introduced. Therefore, the variable  $r$  appearing in the coefficients of the linearised equations is replaced with  $Re/Ro$ . In other words, variations of the Reynolds number with radius are ignored. The terms of order  $(Ro/Re)^2$  are also neglected. However the term of the second derivative in the azimuthal direction is kept, this is because introducing the azimuthal wavenumber,  $\bar{\beta} = \beta Re/Ro$ , in the normal mode analysis distinguishes the  $Re^2$  terms in the denominator and these terms become comparable in size to other terms. The separable linearised equations are then

$$\begin{aligned} \frac{\partial u}{\partial t} + U \frac{\partial u}{\partial r} + \frac{RoU}{Re} u + \frac{RoV}{Re} \frac{\partial u}{\partial \theta} + \frac{RoW}{Re} \frac{\partial u}{\partial z} - \left( \frac{2RoV}{Re} + \frac{Co}{Re} \right) v + U' w \\ = -\frac{\partial p}{\partial r} + \frac{1}{Re} \left( \frac{\partial^2 u}{\partial r^2} + \frac{Ro^2}{Re^2} \frac{\partial^2 u}{\partial \theta^2} + \frac{\partial^2 u}{\partial z^2} \right), \\ \frac{\partial v}{\partial t} + U \frac{\partial v}{\partial r} + \frac{RoU}{Re} v + \frac{RoV}{Re} \frac{\partial v}{\partial \theta} + \frac{RoW}{Re} \frac{\partial v}{\partial z} + \left( \frac{2RoV}{Re} + \frac{Co}{Re} \right) u + V' w \\ = -\frac{1}{Re} \frac{\partial p}{\partial \theta} + \frac{1}{Re} \left( \frac{\partial^2 v}{\partial r^2} + \frac{Ro^2}{Re^2} \frac{\partial^2 v}{\partial \theta^2} + \frac{\partial^2 v}{\partial z^2} \right), \end{aligned} \quad (2.37)$$

$$\begin{aligned} \frac{\partial w}{\partial t} + U \frac{\partial w}{\partial r} + \frac{RoW'}{Re} w + \frac{RoV}{Re} \frac{\partial w}{\partial \theta} + \frac{RoW}{Re} \frac{\partial w}{\partial z} \\ = \frac{\partial p}{\partial z} + \frac{1}{Re} \left( \frac{\partial^2 w}{\partial r^2} + \frac{Ro^2}{Re^2} \frac{\partial^2 w}{\partial \theta^2} + \frac{\partial^2 w}{\partial z^2} \right). \end{aligned}$$

$$\frac{\partial u}{\partial r} + \frac{Ro}{Re} u + \frac{Ro}{Re} \frac{\partial v}{\partial \theta} + \frac{\partial w}{\partial z} = 0. \quad (2.38)$$

To make a normal-mode analysis as first introduced by Gustavsson (1979), the perturbation quantities are expanded in the normal-mode form, as given in (2.39). The normal mode forms are then substituted into (2.37)-(2.38) and a seventh order system of equations involving four differential equations is obtained. The seventh order ODE system is stated in primitive variables in (2.40)-(2.41) and consists of

three 2nd order ODEs and one 1st order ODE.

$$(u, v, w, p) = (\hat{u}(z), \hat{v}(z), \hat{w}(z), \hat{p}(z))e^{i(\alpha r + \bar{\beta}\theta - i\omega t)}. \quad (2.39)$$

Here  $\alpha$  is the radial wavenumber,  $\omega$  is the frequency and  $\bar{\beta}$  is the azimuthal wavenumber.

$$\begin{aligned} -\frac{1}{Re}\hat{u}'' + \frac{Ro}{Re}W\hat{u}' + \left(i\alpha U + i\beta V - i\omega + \frac{\alpha^2}{Re} + \frac{\beta^2}{Re} + \frac{Ro}{Re}U\right)\hat{u} \\ - \left(\frac{2Ro}{Re}V + \frac{Co}{Re}\right)\hat{v} + U'\hat{w} + i\alpha\hat{p} = 0, \\ -\frac{1}{Re}\hat{v}'' + \frac{Ro}{Re}W\hat{v}' + \left(i\alpha U + i\beta V - i\omega + \frac{\alpha^2}{Re} + \frac{\beta^2}{Re} + \frac{Ro}{Re}U\right)\hat{v} \\ + \left(\frac{2Ro}{Re}V + \frac{Co}{Re}\right)\hat{u} + V'\hat{w} + i\beta\hat{p} = 0, \\ -\frac{1}{Re}\hat{w}'' + \frac{Ro}{Re}W\hat{w}' + \left(i\alpha U + i\beta V - i\omega + \frac{\alpha^2}{Re} + \frac{\beta^2}{Re} + \frac{Ro}{Re}W'\right)\hat{w} + \hat{p}' = 0. \end{aligned} \quad (2.40)$$

$$\left(i\alpha + \frac{Ro}{Re}\right)\hat{u} + i\beta\hat{v} + \hat{w}' = 0. \quad (2.41)$$

Consistent with the analyses of Cooper *et al.* (2015), the perturbation quantities should be zero at the disk surface so that the perturbed flow components satisfy the partial-slip condition. Furthermore, the continuity equation (2.41) implies that the first derivative of  $\hat{w}$  should also be zero at the disk surface. All perturbation quantities are naturally set to zero at the far end of the physical domain to ensure that the disturbances are contained within the boundary layer. Therefore, the boundary conditions are

$$\hat{u}(z) = \hat{v}(z) = \hat{w}(z) = \hat{w}'(z) = \hat{p}(z) = 0 \quad \text{at } z = 0, \quad (2.42)$$

$$\hat{u}(z) \rightarrow 0, \quad \hat{v}(z) \rightarrow 0, \quad \hat{w}(z) \rightarrow 0 \quad \text{and} \quad \hat{p}(z) \rightarrow 0, \quad \text{as } z \rightarrow \infty. \quad (2.43)$$

The set of equations (2.37)-(2.38) with the boundary conditions leads to a dispersion relation

$$D(\alpha, \beta, \omega; Re, [\lambda, \eta]) = 0, \quad (2.44)$$

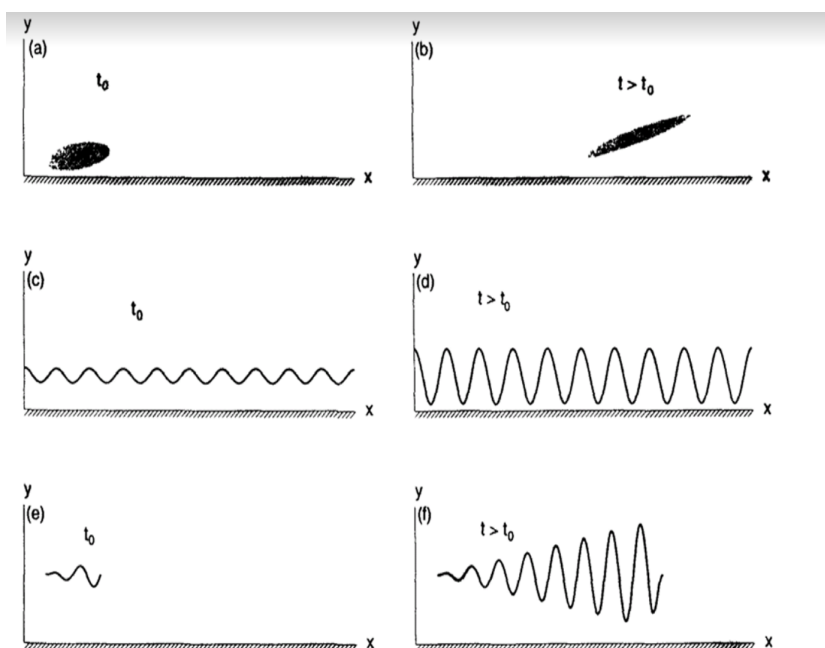


Figure 2.2: Evolution of an initial perturbation. (a,b) Temporal growth of a local perturbation; (c,d) temporal growth of a global periodic ; (e,f) spatial evolution of perturbation. Taken from Schmid & Henningson (2012).

where a non-trivial solution can be found for only specific combinations of the wavenumbers  $\alpha$ ,  $\omega$  &  $\beta$  for various values of the roughness parameters  $\lambda$  and  $\eta$ . The interpretation of the results depends on which of the parameters  $\alpha$  and  $\omega$ , or both, are considered as eigenvalues of the dispersion relation.

In a temporal stability analysis, the perturbations are applied in space and their evolution is observed in time. The analysis is established when the complex frequency  $\omega$  is the eigenvalue of equations (2.40)-(2.41) for a fixed real wavenumber  $\alpha$ , and the stability of the flow is determined by  $\text{Im}(\omega) < 0$ . In other words, the linear growth rate of the perturbations is defined by the imaginary part of the frequency whereas the temporal frequency is indicated by the real part. A comprehensive discussion on this type of analysis can be found in the classic textbook of Drazin & Reid (2004).

In contrast, if a disturbance is generated at a fixed position in space and it is the growth of the source that we are interested in, a spatial stability analysis is required, as will be performed throughout this thesis. This analysis was first applied

in a plasma physics problem by Landau (1946) and implemented for hydrodynamic stability problems by Watson (1962) and Gaster (1962). Some important studies using this method include those of Fasel (1976), Murdock (1977), Malik (1986) and Spalart *et al.* (1991), for example. In a spatial analysis, the complex radial wavenumber  $\alpha$  is the eigenvalue of the problem for a fixed real frequency  $\omega$ . It is also assumed that  $\beta$  is real and  $\mathcal{O}(1)$ . The frequency is set to zero,  $\omega = 0$ , as we are interested in stationary vortices rotating with the rough disk in the rotating frame of reference. The amplification of a normal mode in (2.39) is therefore given by  $-\text{Im}(\alpha) > 0$ . Furthermore, the orientation angle of the stationary vortices with respect to a circle centred on the axis of rotation and the number of spiral vortices on the disk surface are defined as

$$\epsilon = \tan^{-1}(\beta/\alpha_{real}). \quad (2.45)$$

$$n = \beta Re, \quad (2.46)$$

respectively, Spatial analyses have received the most significant attention in the literature as their results can be compared to experimental results in which the flow is perturbed at a reference point and the growth of the perturbation is observed as the fluid flows downstream. Figure 2.2 shows the temporal and spatial evolutions of a perturbation as an example. A comparison for the results of a temporal and a spatial analysis can be made by using the Gaster transformation, but this transformation is only valid for small growth rates (Gaster, 1962).

### 2.3.3. Derivation of the energy balance equations

Another useful method to analyse the stability of an initial perturbation is by measuring its kinetic energy in the volume of boundary layer. Equations for the kinetic energy of the disturbances are given in the work of Cooper & Carpenter (1997) for the particular case of the von Kármán flow. These equations extend to all flows in the BEK system considered in this study. A sketch of the derivation of these equation is given here and full details can be found in Cooper & Carpenter

(1997).

The linearised perturbation equations (2.40)-(2.41) are multiplied by the perturbation components  $\hat{u}$ ,  $\hat{v}$  &  $\hat{w}$ , respectively. The kinetic energy equation is then obtained from the sum of the resulting expressions and is stated as

$$\begin{aligned} & \left\{ \frac{\partial}{\partial t} + U \frac{\partial}{\partial r} + \frac{V}{Re} \frac{\partial}{\partial \theta} - \frac{RoW}{Re} \frac{\partial}{\partial z} \right\} K = \\ & - \hat{u}\hat{w} \frac{\partial U}{\partial z} - \hat{v}\hat{w} \frac{\partial V}{\partial z} + \frac{Ro}{Re} \hat{w}^2 \frac{\partial W}{\partial z} + \frac{RoU}{Re} \hat{u}^2 \\ & + \frac{RoU}{Re} \hat{v}^2 - \left[ \frac{\partial(\hat{u}\hat{p})}{\partial r} + \frac{1}{Re} \frac{\partial(\hat{v}\hat{p})}{\partial \theta} + \frac{\partial(\hat{w}\hat{p})}{\partial z} - \frac{Ro}{Re} \hat{u}\hat{p} \right] \\ & + \left[ \frac{\partial(\hat{u}_j \sigma_{ij})}{\partial x_i} - \sigma_{ij} \frac{\partial \hat{u}_j}{\partial x_i} \right]. \end{aligned} \quad (2.47)$$

Here,  $K = \frac{1}{2}(\hat{u}^2 + \hat{v}^2 + \hat{w}^2)$  and  $\sigma_{ij}$  are anti-symmetric viscous stress terms,

$$\sigma_{ij} = \frac{1}{Re} \left( \frac{\partial u_i}{\partial x_j} - \frac{\partial u_j}{\partial x_i} \right). \quad (2.48)$$

Repeated suffices in (2.47) indicate summation from 1 to 3. All  $\mathcal{O}(1/r)$  viscous terms in this equation are neglected to ensure consistency with the neglect of the  $\mathcal{O}(1/Re^2)$  terms in the perturbation equations. The perturbations are then averaged over a single time period, and azimuthal mode, and followed by an integration across the boundary layer. The steady and rotationally-symmetric nature of the energy is enforced by neglecting both  $t$  and  $\theta$  derivatives, leading to the energy integral equation

$$\begin{aligned} & \int_0^\infty \left[ \underbrace{U \frac{\partial \bar{K}}{\partial r}}_a + \underbrace{\frac{\partial(\hat{u}\hat{p})}{\partial r}}_b - \underbrace{\frac{\partial}{\partial r}(\hat{u}\bar{\sigma}_{11} + \hat{v}\bar{\sigma}_{12} + \hat{w}\bar{\sigma}_{13})}_c \right] dz \\ & = \int_0^\infty \underbrace{\left[ \left( -\hat{u}\hat{w} \frac{\partial U}{\partial z} \right) + \left( -\hat{v}\hat{w} \frac{\partial V}{\partial z} \right) + \left( \hat{w}^2 \frac{Ro}{Re} \frac{\partial W}{\partial z} \right) \right]}_I dz \\ & - \underbrace{\int_0^\infty \left( \sigma_{ij} \frac{\partial \hat{u}_j}{\partial x_i} \right) dz}_II + \underbrace{\int_0^\infty \left( \frac{Ro}{Re} \hat{u}\hat{p} \right) dz}_III + (\hat{w}\hat{p})_{\bar{w}} \\ & - \underbrace{\left[ \hat{u}\bar{\sigma}_{31} + \hat{v}\bar{\sigma}_{32} + \hat{w}\bar{\sigma}_{33} \right]}_IV_{\bar{w}} \end{aligned} \quad (2.49)$$

$$+ \underbrace{\int_0^\infty \frac{Ro}{Re} \frac{\partial \bar{K}}{\partial z} W dz + \int_0^\infty \frac{Ro}{Re} \bar{u}^2 U dz + \int_0^\infty \frac{Ro}{Re} \bar{v}^2 U dz}_{\text{V}}.$$

Overbars in the equation denote a period-averaged quantity, such that  $\overline{\hat{u}\hat{v}} = \hat{u}\hat{v}^* + \hat{u}^*\hat{v}$  where  $*$  indicates a complex conjugate and the  $\bar{w}$  subscripts denote quantities evaluated at the wall. For  $Ro = -1$ , this equation is identical to the energy integral equation of the von Kármán flow (Cooper & Carpenter, 1997; Cooper *et al.*, 2015). As discussed by Cooper & Carpenter (1997), the energy balance can be performed for any eigenmode of the perturbation equations and the energy balance equation is normalized to obtain

$$\begin{aligned} -2\alpha_i = & \underbrace{(P_1 + P_2 + P_3)}_{\text{I}} + \underbrace{D}_{\text{II}} + \underbrace{(PW_1 + PW_2)}_{\text{III}} \\ & \underbrace{(S_1 + S_2 + S_3)}_{\text{IV}} + \underbrace{(G_1 + G_2 + G_3)}_{\text{V}}, \end{aligned} \quad (2.50)$$

Physical interpretations of the terms in the equations (2.49)-(2.50) are given as

- (a) the average kinetic energy convected by the radial mean flow,
- (b) the work done by the perturbation pressure,
- (c) the work done by the viscous stress inside the boundary layer,
  - (I) the Reynolds stress energy production terms,  $\{P_i\}$ ,
  - (II) the viscous dissipation energy removal term,  $\{D\}$ ,
  - (III) pressure work terms,  $\{PW_i\}$ ,
  - (IV) contributions from the work done on the wall by the viscous stresses,  $\{S_i\}$ ,
  - (V) terms arising from the streamline curvature effects and the three dimensionality of the mean flow,  $\{G_i\}$ .

The terms  $PW_2$ ,  $S_1$ ,  $S_2$  and  $S_3$  in the energy balance equation (2.50) are identically zero due to the boundary conditions (2.42) for all the BEK system of flows.

---

The  $G_i$  terms are also identically zero for the Ekman flow,  $Ro = 0$ . The positive terms of the energy balance equation contribute to energy production and the negative ones remove energy from the system. A mode is spatially amplified ( $\alpha_i < 0$ ) when energy production outweighs the energy dissipation in the system.

# Chapter 3

## Numerical methods

In this chapter, a MATLAB boundary value problem solver, `bvp4c`, is used to solve the nonlinear steady mean flow equations (2.18) with boundary conditions (2.19); details are presented in §3.1. The eigenvalue value problem represented by the linear perturbation equations (2.40)-(2.41) is then solved with Chebyshev collocation method in §3.2.1. A sketch of the MATLAB implementations of these methods is also provided and full codes are given in Appendix A.

### 3.1. Matlab solver for the steady mean flow

The solution of the nonlinear mean flow equations is obtained in this study using the MATLAB function `bvp4c`. The numerical method of this function is based on a finite difference code implementing the three stage Lobatto IIIa formula, that can be viewed as an implicit Runge-Kutta formula with a continuous interpolant (Kierzenka & Shampine, 2001). Indeed, the Lobatto IIIa method is a collocation method that provides a  $C^1$  continuous solution that is fourth-order accurate uniformly in a finite interval  $[a, b]$ . The error estimation and mesh selection of the method are based on the residual of the continuous solution.

In the case of this study, the aim is to obtain the mean flow profiles  $U$ ,  $V$  &  $W$  by solving the first three mean flow governing equations (2.18)-(2.19). Note that the pressure term  $P$  is not required to perform the stability analysis (see (2.40)-

(2.41)) but, if required, it can be found from (2.18). Note also that there are precise analytical solutions of each mean flow component for the Ekman flow,  $Ro = 0$ , stated in (2.20), but for  $Ro \neq 0$ , no such analytical solution exists and a numerical analysis is required to solve the governing equations between  $Ro \in [-1, 1] \setminus \{0\}$ .

The governing mean flow equations are required to be transformed into a first order differential equation (ODE) system using five new differentiable functions in order to implement the MATLAB function `bvp4c`. These transformation functions are as follows

$$\phi_1(z) = U, \quad \phi_2(z) = U', \quad \phi_3(z) = V, \quad \phi_4(z) = V' \quad \text{and} \quad \phi_5(z) = W. \quad (3.1)$$

The transformed first order ODE system with the partial-slip boundary conditions is then stated as

$$\begin{aligned} \phi_1' &= \phi_2, \\ \phi_2' &= Ro(\phi_1^2 + \phi_2\phi_5 - \phi_3^2 + 1) - Co(\phi_3 - 1), \\ \phi_3' &= \phi_4, \\ \phi_4' &= Ro(2\phi_1\phi_3 + \phi_4\phi_5) + Co\phi_1, \\ \phi_5' &= -2\phi_1, \end{aligned} \quad (3.2)$$

$$\begin{aligned} \phi_1(0) &= \lambda\phi_2(0), & \phi_3(0) &= \eta\phi_4(0) \quad \text{and} \quad \phi_5(0) = 0, \\ \phi_1 &\longrightarrow 0, & \phi_3 &\longrightarrow 1, & \text{as } z &\longrightarrow \infty. \end{aligned} \quad (3.3)$$

Equations (3.2) and (3.3) represent a two-point boundary value problem. The key aspects of using the `bvp4c` function for this problem can be summarized as follows:

- (1) A solution guess for the boundary value problem solver `bvp4c` is obtained in an initial finite interval using the MATLAB function `bvpinit`.
- (2) The solution of boundary value problem is then evaluated in this interval using a `bvp4c` function.

- (3) The solution is then extended over larger intervals (domain) by continuation, i.e, the solution of former interval is used as a solution guess for the next.
- (4) The process repeats until the desired domain size is achieved.

To determine the domain size that accurately approximates the infinite domain of the mean flow equations, the `bvp4c` method is applied on a continuously extended domain size until the computed values of  $\phi_1(0)$  &  $\phi_3(0)$  for each domain size differ in the sixth decimal place only. It is found that a domain of integration  $z \in [0, 20]$  is sufficiently large for all flows in the BEK system. This length of the interval is consistent with the domain size obtained by Van de Vooren *et al.* (1987) for the Bödewadt flow.

It is also worthwhile to note that the steady mean flow profiles of the rotating flows have been widely solved using a shooting method. For example, the shooting method is used by Van de Vooren *et al.* (1987) for the problem of an immobile disk in a rotating fluid and by Lingwood & Garrett (2011) for a mass injection problem onto a rotating disk. For more details of this method one can see the studies of Lingwood (1995), Jasmine (2003) and Appelquist (2014). However, using a shooting method requires guesses for  $\phi_2(0)$  &  $\phi_4(0)$  individually, which is commonly hard to determine. Therefore, the computed values of  $\phi_2(0)$  &  $\phi_4(0)$ , in the case of different surface roughness distributions, that would be helpful for the implementation of a shooting method are presented in Chapters 4, 5 and 6 of this thesis along with the computed mean flow profiles. The value of  $\phi_4(0)$  is also important for calculation of the resisting torque (2.21).

## 3.2. Chebyshev spectral methods

The shooting method has been widely used in the literature to solve linear governing perturbation equations, however this approach estimates a single eigenvalue at each run and the accuracy of the estimate is strictly dependent on the initial guesses of the parameters, which are often difficult to determine. Moreover, the governing

equations cannot be solved directly with this method because they should be transformed into an ODE system, that requires defining suitable transformation variables. Additionally, only one eigenvalue can be estimated at each run in this method. All other eigenvalues should be determined iteratively. The most commonly used version of the method is introduced by Lessen *et al.* (1968) for an instability analysis of pipe flows and it is used first by Malik (1986) for an instability analysis of the von Kármán flow. More recently it has also been used by Lingwood (1995), Garrett & Peake (2002) and Lingwood & Garrett (2011).

A Chebyshev spectral method on the other hand is able to compute the entire spectrum of eigenvalues in one calculation, and this allows all instability modes to be obtained simultaneously. Furthermore, the approach uses the primitive forms of the governing equations. Thereby, it is chosen in this study as a solution method of the linear governing instability equations (2.40) - (2.41). The approach should not in principle give different results to the shooting method, and the Chebyshev approach is chosen here only for convenience. However, Garrett *et al.* (2016) has recently reported some numerical discrepancies between the two approaches, particularly in the prediction of the Type II mode.

### 3.2.1. Overview of the spectral methods

The full theoretical background of the spectral methods used is given by Peyret (2013) and here we summarize his detailed description. The early uses of Chebyshev spectral methods in hydrodynamic stability problems were based on Galerkin and tau formulations motivated by their high degree of accuracy. For example, Orszag (1971) used the methods for solutions of the Orr-Sommerfeld equations of 2-D Poiseuille flow. A similar study has been performed by Bridges & Morris (1984) to find the nonlinear eigenvalues of the same problem. However, within these approaches the derivatives of the eigenfunctions are always calculated in Chebyshev space and for this reason major modifications may be required if a new coordinate transformation is involved in the problem. Such problems appear in the stability of vortex flows subject to asymmetric disturbances (Howard & Gupta, 1962).

Therefore, the third formulation of Chebyshev methods, the Chebyshev collocation method, has gained more interest in the literature because no major changes are needed if a new coordinate transformation is involved. In this formulation, all the derivatives are calculated in physical spaces.

The Chebyshev collocation method has been used in many different applications. For example, it is used for the global stability of uniform flow around a circular cylinder by Zebib (1984) and has been applied to the instability problem of the trailing line vortex by Khorrami (1991). Khorrami *et al.* (1989) also studied the stability of swirling flows and provide extensive details on the application of the methods. The method is implemented for the BEK system of flows in this thesis and largely follows the details of Khorrami *et al.* (1989).

Before presenting the implementation of the method, a summary of the theoretical background for the Chebyshev methods is presented. This is necessary as they are less common than the shooting method and deserve a comprehensive discussion. Spectral methods are in general a class of weighted residual methods and approximate solutions are defined as a truncated series expansion. The error or residual of the approximations should be set approximately to zero (Finlayson, 2013). This is satisfied through the following process.

The truncated series expansion of a function  $u(x)$  defined on the interval  $[a, b]$  for given orthogonal basis functions  $\varphi_k(x)$  is stated in (3.4). The trigonometric functions  $e^{ikx}$  for periodic problems and Chebyshev  $T_k(x)$  or Legendre  $L_k(x)$  polynomials for non-periodic problems are usually used as orthogonal basis functions in a spectral analysis. The expansion coefficients denoted by  $\hat{c}_k$  are the unknowns of the approximation.

$$u_N(x) = \sum_{k=0}^N \hat{c}_k \varphi_k(x), \quad a \leq x \leq b. \quad (3.4)$$

The residual  $R_N(x)$  is defined as

$$R_N(x) = \mathcal{L}u_n - f, \quad (3.5)$$

where  $u_N(x)$  is the approximate solution of the differential equation

$$\mathcal{L}u - f = 0, \quad (3.6)$$

and  $\mathcal{L}$  is a partial differential operator subject to the appropriate boundary conditions. It is assumed that  $f$  is a continuous function. The residual then is forced to be zero by setting the following scalar product to zero,

$$(R_N, \psi_i)_{w_*} = \int_a^b R_N \psi_i w_* dx = 0, \quad i \in I_N. \quad (3.7)$$

Here,  $\psi_i(x)$  are the weighting functions and  $w_*$  is the weight. The dimension of the discrete set  $I_N$  is the number of collocation points  $x_i$ . The distinct formulation types of the spectral methods are determined by the choice of the weighting functions and the weight. For Galerkin and tau formulations the weighting functions are the same as the basis functions and the weight is the same weight associated with orthogonality of the basis functions. For the Chebyshev collocation method they are chosen as

$$\psi_i(x) = \delta(x - x_i) \quad \text{and} \quad w_* = 1, \quad (3.8)$$

where  $\delta$  is the Dirac delta-function and  $x_i$  are selected collocation points in  $[a, b]$ .

It is now clear from (3.7) and (3.8) that

$$R_N(x_i) = 0, \quad (3.9)$$

which also implies, from definition of the residual, that

$$u_N(x_i) = u(x_i), \quad i = 0, \dots, N. \quad (3.10)$$

The final equation raises an algebraic system of  $N + 1$  coefficients  $\hat{c}_k$  defined as follows

$$\sum_{k=0}^N \hat{c}_k \varphi_k(x_i) = u(x_i), \quad i = 0, \dots, N. \quad (3.11)$$

The main advantage of spectral methods is to obtain a higher degree of accuracy

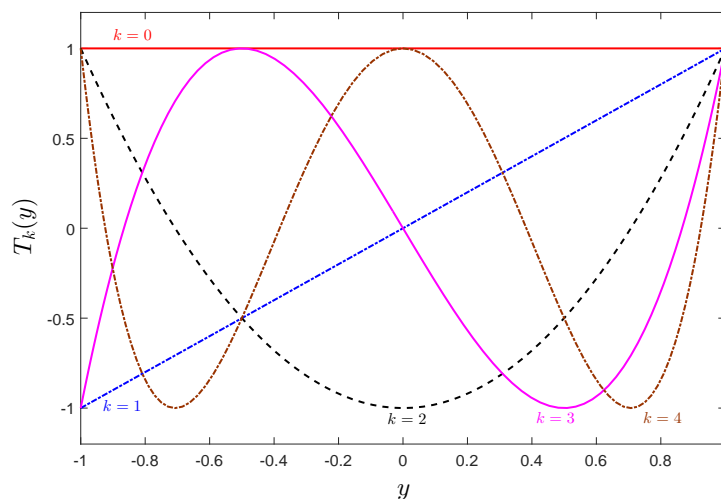


Figure 3.1: The first few Chebyshev polynomials of first kind.

when compared to the shooting method. The error between  $u(x)$  and  $u_N(x)$  is

$$\|u - u_N\| \leq \frac{c}{N^\Gamma},$$

where  $\Gamma$  is the number of continuous derivatives of  $u(x)$ ,  $c$  is a constant and  $N$  is the number of collocation points (Canuto *et al.*, 1988). Therefore, the degree of accuracy is determined by the smoothness of the exact solution  $u(x)$  for a sufficiently large number of the collocation points. A comparison of the shooting and Chebyshev methods is presented by Appelquist (2014) in the case of the von Kármán flow.

### 3.2.2. Implementation of Chebyshev collocation method

The Chebyshev collocation method is based on the Chebyshev polynomials defined recursively in (3.12) on the interval  $y \in [-1, 1]$ .

$$\begin{aligned} T_0(y) &= 1, \\ T_1(y) &= y, \\ T_{k+1}(y) &= 2yT_k(y) - T_{k-1}(y). \end{aligned} \tag{3.12}$$

Because the linear equations (2.40)-(2.41) governing the BEK system of flows involve second order ODEs, only the first and second derivatives of the Chebyshev

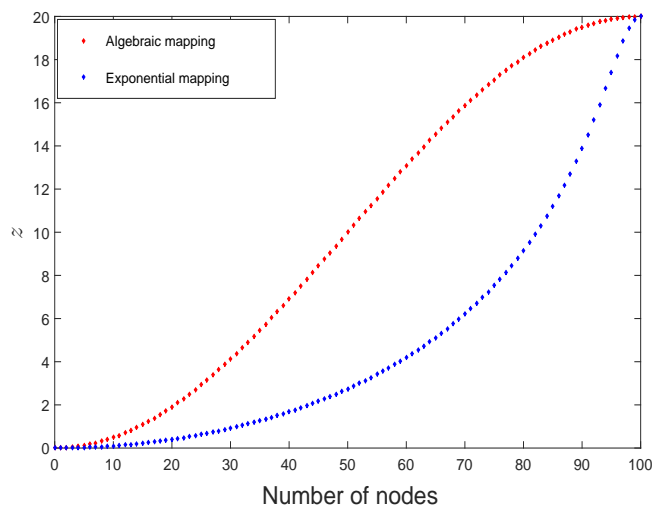


Figure 3.2: Comparable distributed nodes on the rotational disk geometry.

polynomials are needed and they can be defined in a recurrence relation as

$$\begin{aligned}
 T_0'(y) &= 0, & T_0''(y) &= 0, \\
 T_1'(y) &= 1, & T_1''(y) &= 0, \\
 T_2'(y) &= 4T_1'(y), & T_2''(y) &= 4T_1''(y), \\
 T_k'(y) &= 2T_{k-1}(y) + 2yT_{k-1}'(y) - T_{k-2}'(y), \\
 T_k''(y) &= 4T_{k-1}'(y) + 2yT_{k-1}''(y) - T_{k-2}''(y),
 \end{aligned}$$

for  $k = 3, 4, \dots, N$ . Here, superscripts ' and '' denote the first and second derivatives with respect to  $y$ .

In order to solve the eigenvalue problem (2.40)-(2.41), with the aim of obtaining the eigenvalues of the radial wavenumber  $\alpha$  and the corresponding eigenfunctions of the perturbation quantities  $(\hat{u}, \hat{v}, \hat{w}, \hat{p})$ , the Chebyshev expansions of these quantities should be introduced at a number of points in the physical domain of the BEK system of flows, called collocation points.

The determination of these collocation points is based on a transformation of the Gauss-Lobatto collocation points  $y_j$ , defined in (3.13) at  $N + 1$  number of points in the interval  $[-1, 1]$  into the physical domain  $[0, 20]$ .

$$y_j = -\cos\left(\frac{j\pi}{N}\right), \quad j = 0, 1, \dots, N. \quad (3.13)$$

An exponential mapping function described in (3.14) is used in this thesis to distribute 100 collocation points between the lower disk surface,  $z = 0$ , the top of the domain,  $z_{max} = 20$ . The exponential mapping transformation distributes the collocation points mainly into the boundary layer. This is necessary in a boundary layer flow because the discrepancies of the quantities are high and more calculations should be performed near the lower surface to ensure a higher degree of accuracy. A comparison between the exponential mapping and an algebraic mapping is presented in Figure (3.2).

$$\begin{aligned} z &= -4\log\left(\frac{y-A}{B}\right), \\ A &= -1 - B, \\ B &= 2/(e^{-\frac{z_{max}}{4}} - 1), \end{aligned} \tag{3.14}$$

where  $z_{max} = 20$  in this case. In the physical space of the rotating disk flows, the Chebyshev polynomials and their derivatives are constructed using the chain rule as

$$\begin{aligned} S_k(z) &= T_k(y), \\ S'_k(z) &= \frac{dT_k(y)}{dz} = T'_k(y) \frac{dy}{dz}, \\ S''_k(z) &= \frac{d^2T_k(y)}{dz^2} = T''_k(y) \left(\frac{dy}{dz}\right)^2 + T'_k(y) \frac{dy^2}{dz^2}. \end{aligned} \tag{3.15}$$

It should be noted that superscripts ' and '' denote the first and second derivatives of  $S_k(z)$  and  $T_k(y)$  with respect to  $z$  and  $y$ , respectively. The truncated series of the perturbation quantities ( $\hat{u}, \hat{v}, \hat{w}, \hat{p}$ ) and of their derivatives at collocation points  $z_j$  are given in (3.16)-(3.18) as the sum of the contributions of all the transformed Chebyshev polynomials.

$$\begin{aligned} \hat{u}(z_j) &= \sum_{k=0}^N \hat{c}_k^{\hat{u}} S_k(z_j), & \hat{v}(z_j) &= \sum_{k=0}^N \hat{c}_k^{\hat{v}} S_k(z_j), \\ \hat{w}(z_j) &= \sum_{k=0}^N \hat{c}_k^{\hat{w}} S_k(z_j), & \hat{p}(z_j) &= \sum_{k=0}^N \hat{c}_k^{\hat{p}} S_k(z_j), \end{aligned} \tag{3.16}$$

$$\begin{aligned}
\hat{u}'(z_j) &= \sum_{k=0}^N \hat{c}_k^{\hat{u}} S'_k(z_j), & \hat{v}'(z_j) &= \sum_{k=0}^N \hat{c}_k^{\hat{v}} S'_k(z_j), \\
\hat{w}'(z_j) &= \sum_{k=0}^N \hat{c}_k^{\hat{w}} S'_k(z_j), & \hat{p}'(z_j) &= \sum_{k=0}^N \hat{c}_k^{\hat{p}} S'_k(z_j),
\end{aligned} \tag{3.17}$$

$$\begin{aligned}
\hat{u}''(z_j) &= \sum_{k=0}^N \hat{c}_k^{\hat{u}} S''_k(z_j), & \hat{v}''(z_j) &= \sum_{k=0}^N \hat{c}_k^{\hat{v}} S''_k(z_j), \\
\hat{w}''(z_j) &= \sum_{k=0}^N \hat{c}_k^{\hat{w}} S''_k(z_j), & \hat{p}''(z_j) &= \sum_{k=0}^N \hat{c}_k^{\hat{p}} S''_k(z_j).
\end{aligned} \tag{3.18}$$

The perturbation quantities should be zero at the disk surface so that the perturbed flow  $U + \hat{u}$  etc. satisfy the partial-slip condition mathematically imposed on the steady flow. Furthermore, the continuity equation (2.41) implies that the first derivative of  $\hat{w}$  should also be zero at the disk surface. All perturbation quantities are naturally set to be zero at the far end of the physical domain.

Inserting the Chebyshev expansions of the perturbation quantities along with the boundary conditions into the linearised governing equations (2.40)-(2.41) gives a generalized eigenvalue problem for the wavenumber  $\alpha$  of the form

$$(A_2 \alpha^2 + A_1 \alpha + A_0) \mathcal{V} = 0. \tag{3.19}$$

The matrices  $A_2$ ,  $A_1$  and  $A_0$  are of size  $4(N+1) \times 4(N+1)$ , where 4 is the number of unknown quantities and  $\mathcal{V}$  is the matrix of the eigenfunctions. The form of the matrices are stated in (3.20)-(3.22). The complex parameter  $\varepsilon$  in the matrices  $A_2$  and  $A_1$  is set to  $\varepsilon = -20i$ , where  $i = \sqrt{-1}$ , this ensures that the boundary conditions are properly imposed. MATLAB includes a very efficient solver of this generalized eigenvalue problem (*polyeig* function) and that is used here to develop the spectral code in order to compute the solutions of the dispersion relation (2.44). This is done for specific combinations of the wavenumbers  $\alpha$ ,  $\omega$  &  $\beta$  for various values of the roughness parameters  $\lambda$  &  $\eta$ .

In the code the solutions and eigenvalues are computed for fixed values of  $Re$  and iteratively changed values of  $\beta$ . For each  $\beta$  the modes are sorted in a descending

---

order of  $\text{Im}(\alpha_i)$  to select the mode with smallest imaginary part as a branch point and the iteration runs until a branch point with zero imaginary part is found. That is a neutral point on the neutral curve. This process is then repeated iteratively for a wide range of  $Re$  until the entire neutral curve of convective instability is obtained. The details of the code are presented in [Appendix A](#).

$$\mathbf{A}_2 = \begin{pmatrix}
S_0(z_0) & 0 & 0 & 0 & \dots \\
0 & S_N(z_0) & 0 & 0 & \dots \\
0 & 0 & S_N(z_0) & 0 & \dots \\
0 & 0 & 0 & S_N(z_0) & \dots \\
(1/Re)S_0(z_1) & 0 & 0 & 0 & \dots \\
0 & (1/Re)S_0(z_1) & 0 & 0 & \dots \\
0 & 0 & (1/Re)S_0(z_1) & 0 & \dots \\
0 & 0 & 0 & (1/Re)S_0(z_1) & \dots \\
\vdots & \vdots & \vdots & \vdots & \dots \\
S_N(z_N) & 0 & 0 & 0 & \dots \\
0 & S_N(z_N) & 0 & 0 & \dots \\
0 & 0 & S_N(z_N) & 0 & \dots \\
0 & 0 & S'_N(z_N) & 0 & \dots
\end{pmatrix} \tag{3.20}$$

$$A_1 = \begin{pmatrix} \varepsilon S_N(z_0) & 0 & 0 & 0 & \dots \\ 0 & \varepsilon S_N(z_0) & 0 & 0 & \dots \\ 0 & 0 & \varepsilon S_N(z_0) & 0 & \dots \\ 0 & 0 & 0 & \varepsilon S_N(z_0) & \dots \\ iUS_0(z_1) & 0 & 0 & 0 & \dots \\ 0 & iUS_0(z_1) & 0 & 0 & \dots \\ 0 & 0 & iUS_0(z_1) & 0 & \dots \\ iS_0(z_1) & 0 & 0 & 0 & \dots \\ \vdots & \vdots & \vdots & \vdots & \dots \\ \varepsilon S_N(z_N) & 0 & 0 & 0 & \dots \\ 0 & \varepsilon S_N(z_N) & 0 & 0 & \dots \\ 0 & 0 & \varepsilon S_N(z_N) & 0 & \dots \\ 0 & 0 & \varepsilon S'_N(z_N) & 0 & \dots \end{pmatrix} \quad (3.21)$$

$$\mathbf{A}_0 = \begin{pmatrix}
\varepsilon S_N(z_0) & 0 & 0 & 0 & \dots \\
0 & \varepsilon S_N(z_0) & 0 & 0 & \dots \\
0 & 0 & \varepsilon S_N(z_0) & 0 & \dots \\
0 & 0 & 0 & \varepsilon S_N(z_0) & \dots \\
(Mx(z_1) + U(z_1)Ro/Re)S_0(z_1) + \frac{RoW(z_1)}{Re}S'_0(z_1) - \frac{1}{Re}S''_0(z_1) & -(1/Re)(2RoV(z_1) + Co)S_0(z_1) & U'(z_1)S_0(z_1) & 0 & \dots \\
(1/Re)(2RoV(z_1) + Co)S_0(z_1) & (Mx(z_1) + U(z_1)Ro/Re)S_0(z_1) + \frac{RoW(z_1)}{Re}S'_0(z_1) - \frac{1}{Re}S''_0(z_1) & V'(z_1)S_0(z_1) & i\beta S_0(z_1) & \dots \\
0 & 0 & (Mx(z_1) + W'(z_1)Ro/Re)S_0(z_1) + \frac{RoW(z_1)}{Re}S'_0(z_1) - \frac{1}{Re}S''_0(z_1) & S'_0(z_1) & \dots \\
(Ro/Re)S_0(z_1) & i\beta S_0(z_1) & S'_0(z_1) & 0 & \dots \\
\vdots & \vdots & \vdots & \vdots & \dots \\
\varepsilon S_N(z_N) & 0 & 0 & 0 & \dots \\
0 & \varepsilon S_N(z_N) & 0 & 0 & \dots \\
0 & 0 & \varepsilon S_N(z_N) & 0 & \dots \\
0 & 0 & \varepsilon S'_N(z_N) & 0 & \dots
\end{pmatrix} \tag{3.22}$$

$$Mx(z_j) = i\beta V(z_j)/Re - i\omega + \beta^2/Re^3.$$

# Chapter 4

## Effect of azimuthally anisotropic roughness on the BEK family of boundary layers

### 4.1. Overview

This chapter is concerned with the effects of azimuthally anisotropic roughness - radial grooves - on the convective instability mechanism within the general class of rotating BEK boundary-layers. Viscous and streamline-curvature effects are included and local linear stability analyses are conducted for the boundary-layer flows parametrised by a Rossby number  $Ro$  between -1 to 1. Furthermore, an energy analysis is performed to confirm the results of the linear stability analysis.

The effects of radial grooves on the solutions of the steady mean flow equations are discussed in §4.2. Section 4.3 includes the discussions on the convective instability analysis. The neutral curves based on the solutions of the perturbation equations (2.40) -(2.41) with boundary conditions (2.42) are presented in §4.3.1. In §4.3.2 effects of surface roughness on the growth rates,  $|\alpha_i|$ , of each instability mode are discussed. The results of an energy analysis are presented in §4.4. Finally, absolute instability is discussed briefly in §4.5.

## 4.2. The steady mean flow solutions

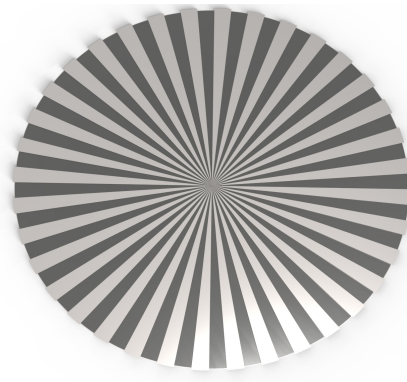


Figure 4.1: Radial grooves over a disk.

In this section, we solve the steady mean flow equations (2.18) with the primary aim of studying the effects of the azimuthally anisotropic roughness on the mean flow profiles of the BEK family of boundary layers. The secondary aim of this section is to compare these effects with those of the active drag control mechanisms applied on the BEK system of flows; the surface suction technique studied by Lingwood & Garrett (2011) and the uniform distribution of magnetic field technique studied by Jasmine & Gajjar (2005).

The azimuthally anisotropic surface roughness corresponds to radial grooves on the disk surface. Therefore, we set the roughness parameters in the partial-slip boundary conditions (2.19), obtained under the MW model, to  $\lambda > 0$ ,  $\eta = 0$ . The governing equations of the steady mean flows for each boundary layer in the BEK system are parametrised by the Rossby number. For each flow within the system, except the Ekman flow, we solve these governing equations with the MATLAB function described in §3.1. For the Ekman flow, the precise analytical solution of each mean flow component is stated in (2.20).

The computed mean flow profiles are in the radial direction,  $U$ -component; azimuthal direction,  $V$ -component; and axial direction,  $W$ -component. They are presented in this section for different sizes of radial grooves. The initial values of  $U'(0)$  and  $V'(0)$  are presented in Table 4.1 for various values of roughness parameter  $\lambda$ .

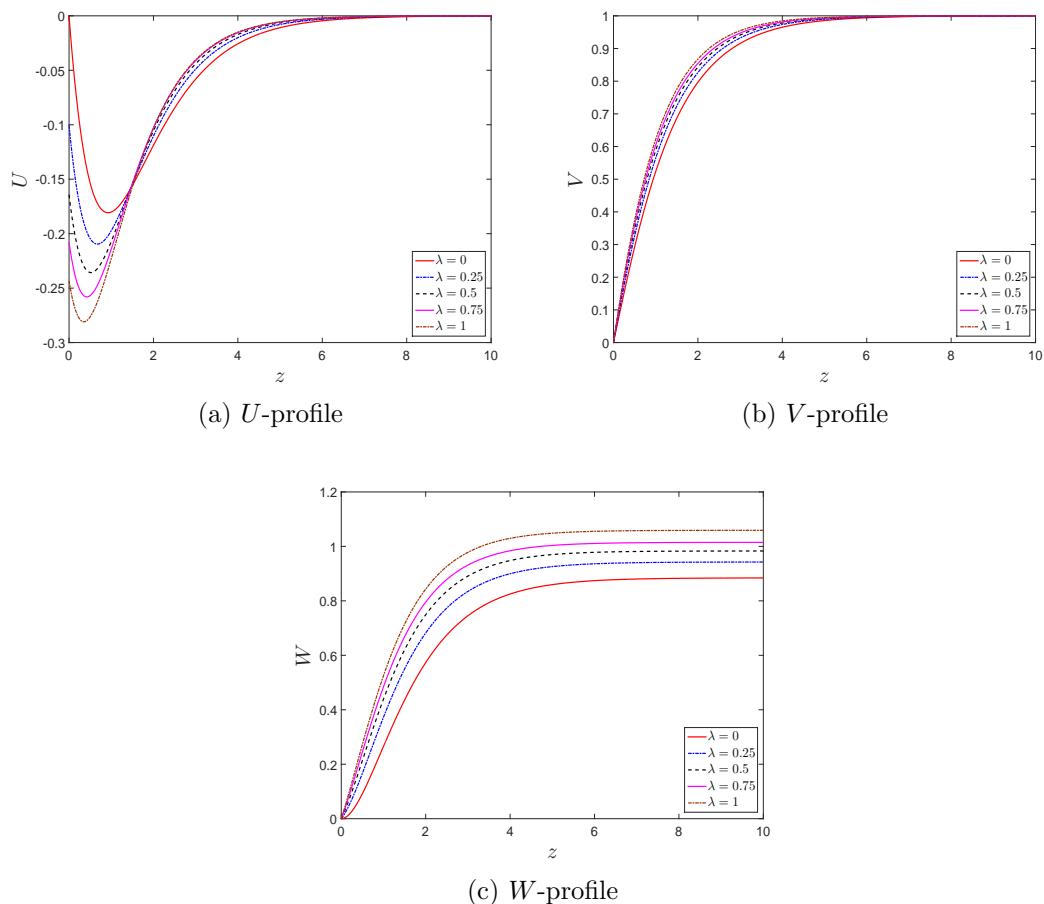


Figure 4.2: Mean-flow components of the von Kármán flow in the case of azimuthally-anisotropic roughness (radial grooves,  $\eta = 0$ ).

Our initial values for the von Kármán flow are identical those presented by Miklavcic & Wang (2004).

The important properties of the mean flow profiles, which are potentially affected by increased surface roughness can be listed as: the oscillatory behaviour of each flow component, the boundary layer thickness, the size of the radial wall jet and the amount of fluid entrained into the boundary layer. The size of the radial wall jet depends the maximum value of radial component  $U$  in the flow field. The amount of fluid entrained into the boundary layer depends on the magnitude of the  $W$  component. Another important physical property that is worthwhile to note is the resisting torque on the disk as defined by (2.21).

The oscillatory behaviour of the mean flow components is important because

The von Kármán layer,  $Ro = -1$

Parameter	$U'(0)$	$V'(0)$
$\lambda = 0$	-0.510232616	0.615922011
$\lambda = 0.25$	-0.407302858	0.732947507
$\lambda = 0.5$	-0.328395172	0.791387076
$\lambda = 0.75$	-0.277176378	0.836488964
$\lambda = 1$	-0.243259325	0.879697426

$Ro = -0.5$

Parameter	$U'(0)$	$V'(0)$
$\lambda = 0$	-0.857041159	0.907317540
$\lambda = 0.25$	-0.672583324	1.083902785
$\lambda = 0.5$	-0.549620619	1.191662485
$\lambda = 0.75$	-0.463249007	1.263211219
$\lambda = 1$	-0.399729902	1.313836983

$Ro = 0.5$

Parameter	$U'(0)$	$V'(0)$
$\lambda = 0$	-1.017626469	0.961193351
$\lambda = 0.25$	-0.857841282	1.142541358
$\lambda = 0.5$	-0.751302313	1.289667892
$\lambda = 0.75$	-0.673907900	1.415161509
$\lambda = 1$	-0.614567802	1.525693670

The Bödewadt layer,  $Ro = 1$

Parameter	$U'(0)$	$V'(0)$
$\lambda = 0$	-0.941970896	0.772885383
$\lambda = 0.25$	-0.923425784	0.900014755
$\lambda = 0.5$	-0.986879150	1.120196486
$\lambda = 0.75$	-1.280383135	1.707716448

Table 4.1: The initial values of  $U'$  and  $V'$  at the disk surface for various  $Ro$ , in the case of azimuthally-anisotropic roughness (radial grooves,  $\eta = 0$ ).

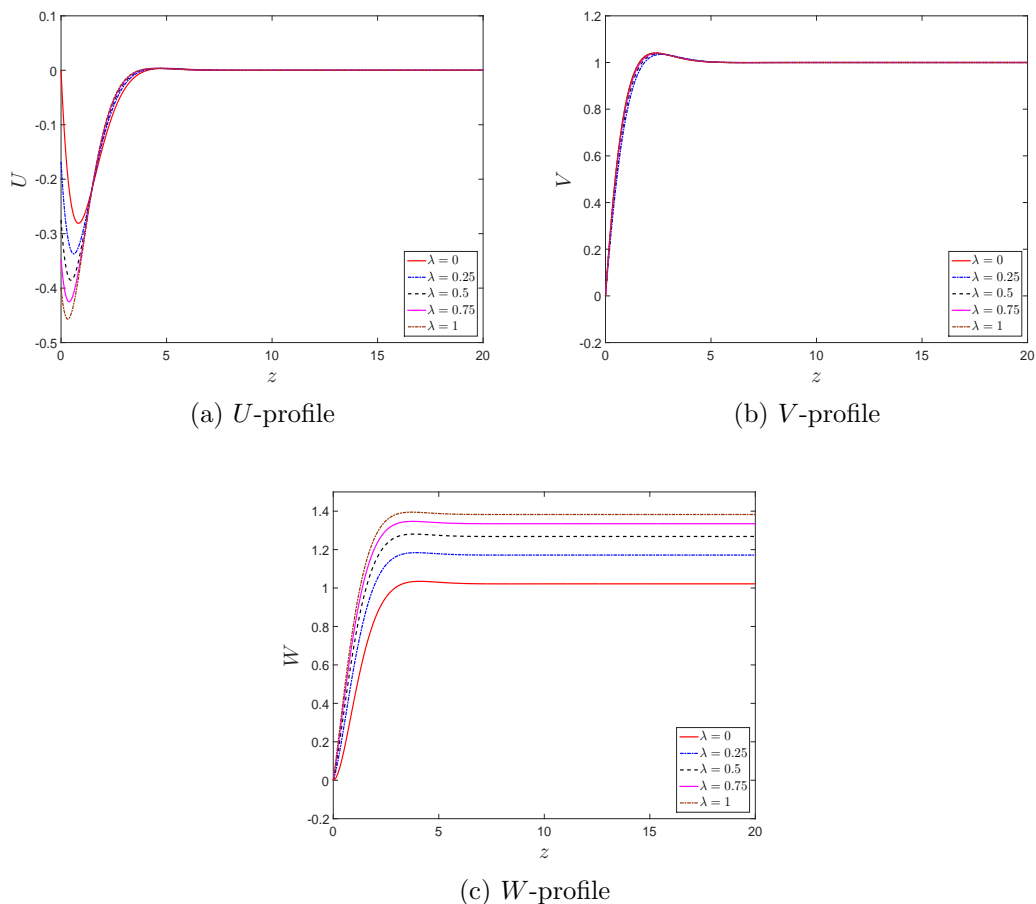


Figure 4.3: Mean-flow components for  $Ro = -0.5$  in the case of azimuthally-anisotropic roughness (radial grooves,  $\eta = 0$ )

the presence of inflectional points leads to the Type I instability mechanism, that is, the cross-flow instability (Saric & Reed, 2003). Lingwood & Garrett (2011) report that in the smooth case the mean flow components of the BEK system of flows are oscillatory through the boundary layer, although to a reduced extent as the flows change from the Bödewadt flow to the von Kármán one, i.e. as  $Ro$  decreases from unity to minus unity. In the azimuthally anisotropic rough case, it can be seen from Figures 4.2-4.6 that the oscillatory behaviour of each mean flow component is amplified for all flows of the BEK system as the roughness parameter  $\lambda$  is increased. This observation is in contrast to the effects of increased surface suction (Lingwood & Garrett, 2011) for all flows of the system and an increase in the uniform magnetic field applied to the von Kármán flow (Jasmine & Gajjar, 2005). In both of these

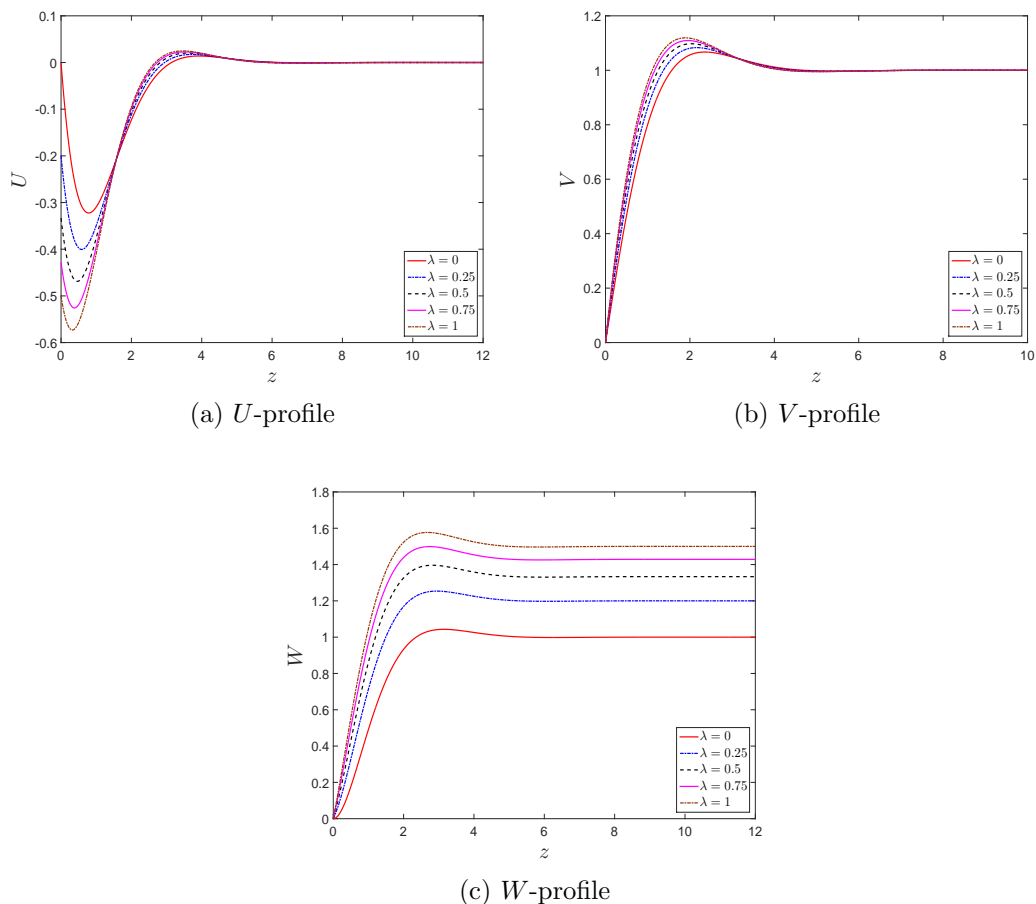


Figure 4.4: Mean-flow components of the Ekman flow ( $Ro = 0$ ) in the case of azimuthally-anisotropic roughness (radial grooves,  $\eta = 0$ ).

studies the amplification of their mean flow components reduce with an increase in their parameters.

The maximum value of the radial component,  $U$ , for all  $Ro$  increases for larger values of roughness parameter  $\lambda$  as is evident from Figures 4.2(a)-4.6(a). In other words, increased radial grooves acts to increase the radial wall jet. This is physically sensible as the radial component  $U$  would be channelled along the radial direction by radial grooves. The growth rate of the maximum value increases substantially as  $Ro$  changes from -1, the von Kármán flow, to 1, the Bödewadt flow. These figures also show that the location of the maximum value of  $U$  moves towards the disk surface with increased roughness. Therefore, we also interpret that the thickness of the boundary layer for all  $Ro$  reduces for increased roughness. These changes of the

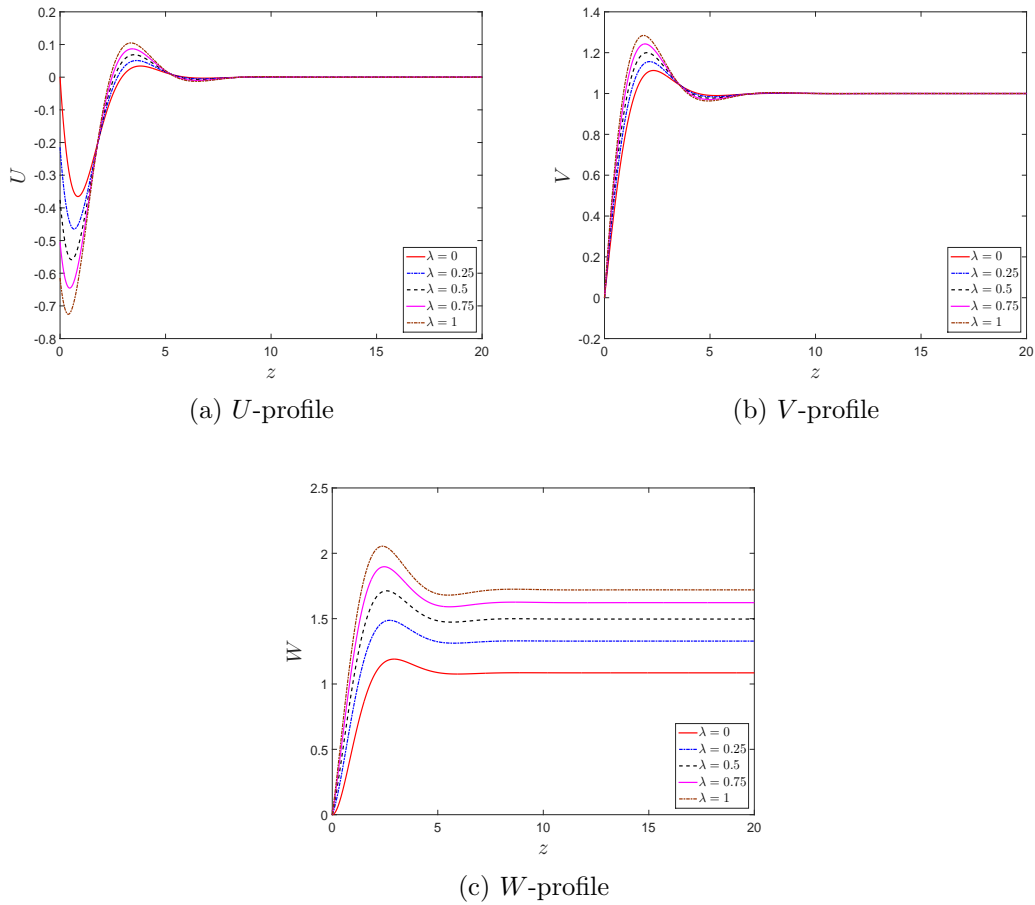


Figure 4.5: Mean-flow components for  $Ro = 0.5$  in the case of azimuthally-anisotropic roughness (radial grooves,  $\eta = 0$ ).

$U$  profile are again in contrast to those observed in the smooth case for increased surface suction and increased uniform magnetic field cases.

It is found by Lingwood & Garrett (2011) that surface suction reduces the magnitude of axial flow in the far-field for  $Ro \geq 0$ , and increases it for  $Ro < 0$ . However, Figures 4.2(c)-4.6(c) show that azimuthally anisotropic roughness on the disk surface increases the magnitude of the axial flow for increased  $\lambda$  for all flows of the BEK system with the exception of the Bödewadt flow. In the Bödewadt flow, the magnitude of the axial flow in the far-field become decreases, when compared to the smooth case, after a threshold of roughness parameter has been reached. This threshold appears to be around  $\lambda = 0.5$ . Therefore, we predict that the amount of fluid entrained into the boundary layer increases for all  $Ro$  as the roughness is

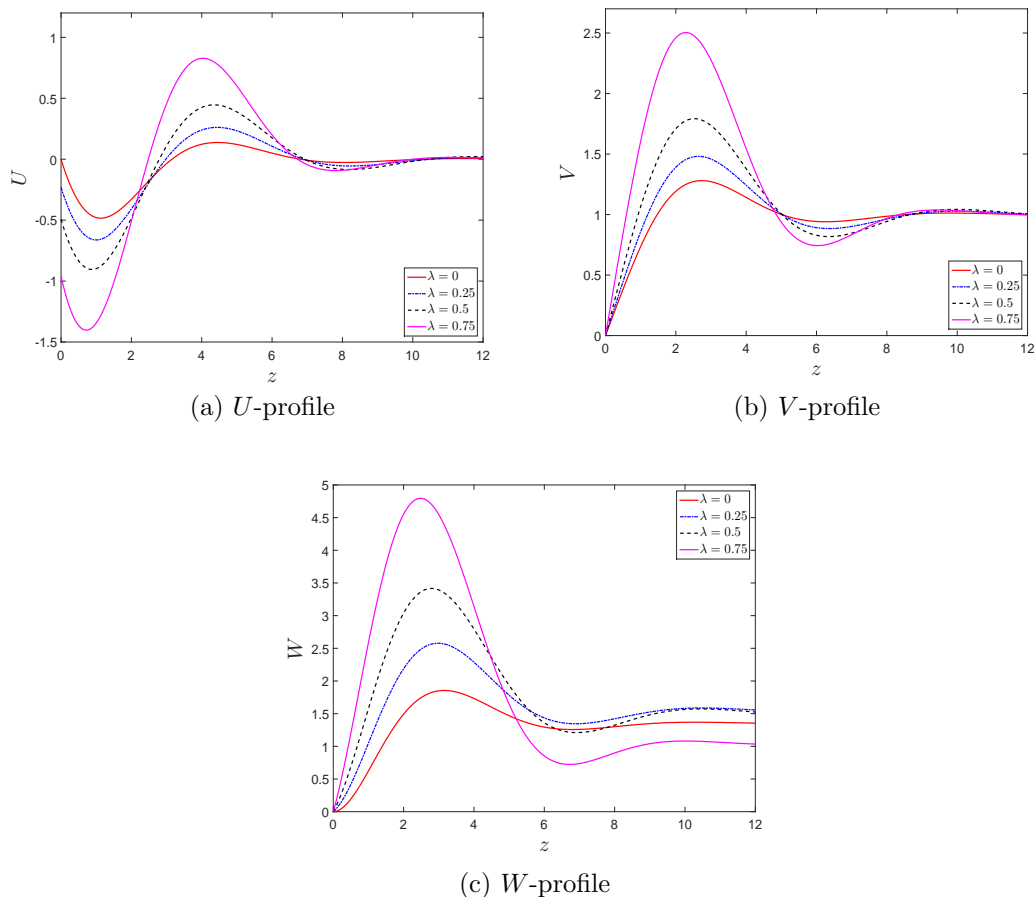


Figure 4.6: Mean-flow components of the Bödewadt flow ( $Ro = 1$ ) in the case of azimuthally-anisotropic roughness (radial grooves,  $\eta = 0$ ).

increased with the exception of the Bödewadt case.

The effects of radial grooves on the azimuthal velocity profile  $V$  are presented in Figures 4.2(b)-4.6(b), and notable changes are not observed. These figures reveal that the oscillatory behaviour of the component moves upwards in the axial direction and the amplification rate is gradually increased as the roughness parameter  $\lambda$  is increased. The wall value of the component is unchanged for all  $Ro$  due to a direct implication of the partial slip boundary conditions (2.19) at  $\eta = 0$ . Moreover, the resisting torque  $T$  given in (2.21) is related to the initial value of the derivative of this component. Miklavcic & Wang (2004) reported that increasing  $\lambda$  increases the torque substantially in the case of the von Kármán flow and it is seen from Table 4.1 that it is true at all  $Ro \neq 0$  in the BEK system. In the Ekman case, the torque

is equal to zero as might be expected in this system with zero torque between the upper and lower flows.

A summary of the main findings in this section for each particular flow in the BEK system indicate that the effect of azimuthally-anisotropic roughness on the jets are consistent with those obtained by Cooper *et al.* (2015) for the von Kármán layer. That is, increased radial grooves act to increase the magnitude of the wall and radial jets. Furthermore, the effects of increased roughness on the oscillatory behaviours of the flow components are opposite to the responses seen from the addition of surface mass flux and the distribution of uniform magnetic field. Similarly, we obtain an increase in the amount of fluid entering the boundary layers for the majority of the flows in the BEK system.

### 4.3. The convective instability analysis

In this section we are concerned with the occurrence of convective instabilities in the case of the surface grooves distributed in a radial direction over the rotating disk. The convective instability is determined by the computed solutions of the perturbation equations (2.40)-(2.41) using the spectral Chebyshev method described in §3.2. We analyse the characteristics of convective instability in terms of neutral curves in §4.3.1 and growth rates in §4.3.2. We suppose in the first instance that the flow is not absolutely unstable. As a result, in the Briggs-Bers procedure (Briggs (1964) & Bers (1975)) we can set the imaginary part of the frequency to zero, so that  $\omega_i = 0$ . To produce neutral curves of convective instability we also insist that the vortices rotate with the lower disk surface, thereby the real part of the frequency is set to  $\omega_r = 0$ , and the radial wavenumber  $\alpha$  and the azimuthal wavenumber  $\beta$  are computed.

#### 4.3.1. Neutral curves

In this section we present neutral curves for the boundary layer flows belonging to the BEK system in  $(Re, \alpha_r)$ ,  $(Re, n)$  and  $(R, \epsilon)$ -planes. Each curve encloses

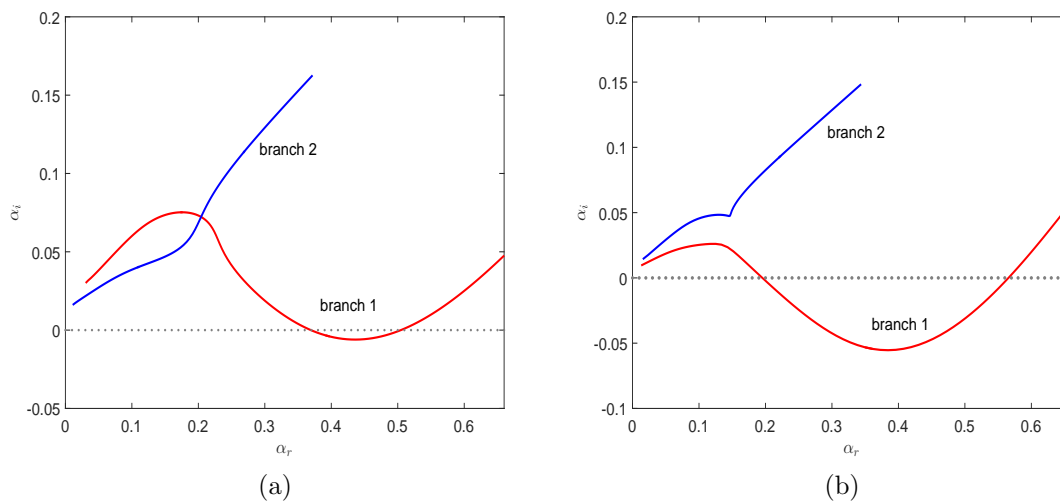


Figure 4.7: The two spatial branches showing region of crossflow instability for the Ekman flow in the case of  $\lambda = 0.5$ ; (a) at  $Re = 227$ , (b) at  $Re = 500$ .

a region in which the boundary layers are convectively unstable. As discussed in Chapter §1, two instability modes are found to determine the convective instability characteristic of each flow in the BEK system. These modes are the Type I mode of instability (due to an inflectional crossflow velocity component) and the Type II mode of instability (due to the streamline curvature); this was shown by Malik (1986), Hall (1986) and Lingwood (1995) for rotating disk flows. The convective instability is indicated by a branch region lying below the  $\alpha_r$ -axis. Figure 4.7(a) shows two spatial branches in the case of a moderate roughness level,  $\lambda = 0.5$  for the Ekman flow in the complex  $\alpha$  plane at  $Re = 227$ , where an exchange of modes is observed. The region of convective instability is now determined by the modified branch 1. The minima of the modified branch 1 moves downwards as  $Re$  is increased and the branch points crossing the  $\alpha_r$ -axis move apart, causing the widening of the regions of instability. The modified branches at  $Re = 500$  are shown in Figure 4.7(b). Only one lobe maps out the neutral curve as there is only one minima of the modified branch 1. This lobe characterises the Type I instability mode. This spatial branch behaviour is typical for each flow in the BEK system in the case of azimuthally anisotropic surface roughness.

The governing equations of each flow in the BEK system are parametrised by

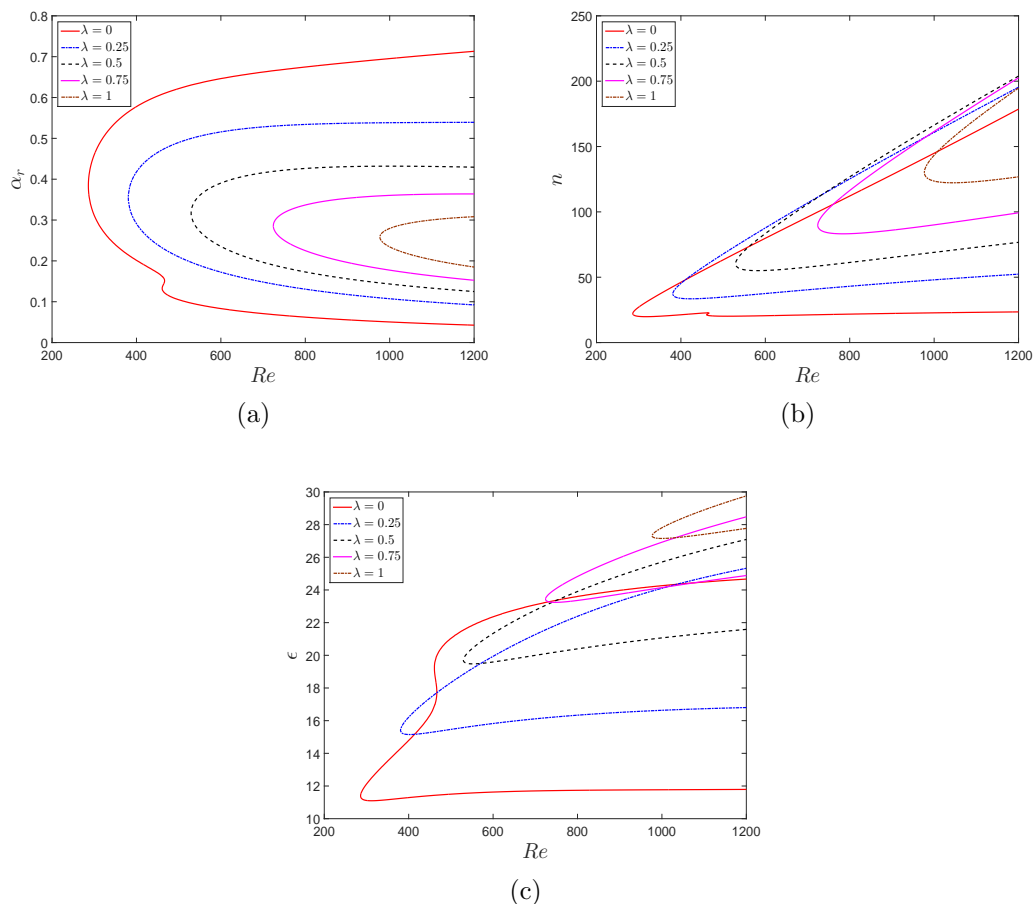


Figure 4.8: Neutral curves of the convective instability of the von Kármán flow in the case of azimuthally-anisotropic roughness (radial grooves,  $\eta = 0$ ).

the Rossby number,  $Ro$ , in the perturbation equations (2.40)-(2.41). The obtained equations of each flow are solved with a MATLAB code written for this study by using the spectral Chebyshev method. The details of the code and method are discussed in §3.2.1.

We begin our discussion by presenting neutral curves of the von Kármán flow in the case of azimuthally anisotropic roughness in Figure 4.8. These curves are consistent with those of Cooper *et al.* (2015) and we include them in this study for completeness of the BEK system and verification of our newly written code. It is seen from Figure 4.8(a) that radial grooves have a strong stabilising effect on both the Type I and Type II modes in terms of the critical Reynolds number and the width of the instability region. We observe that the lower lobe of the neutral

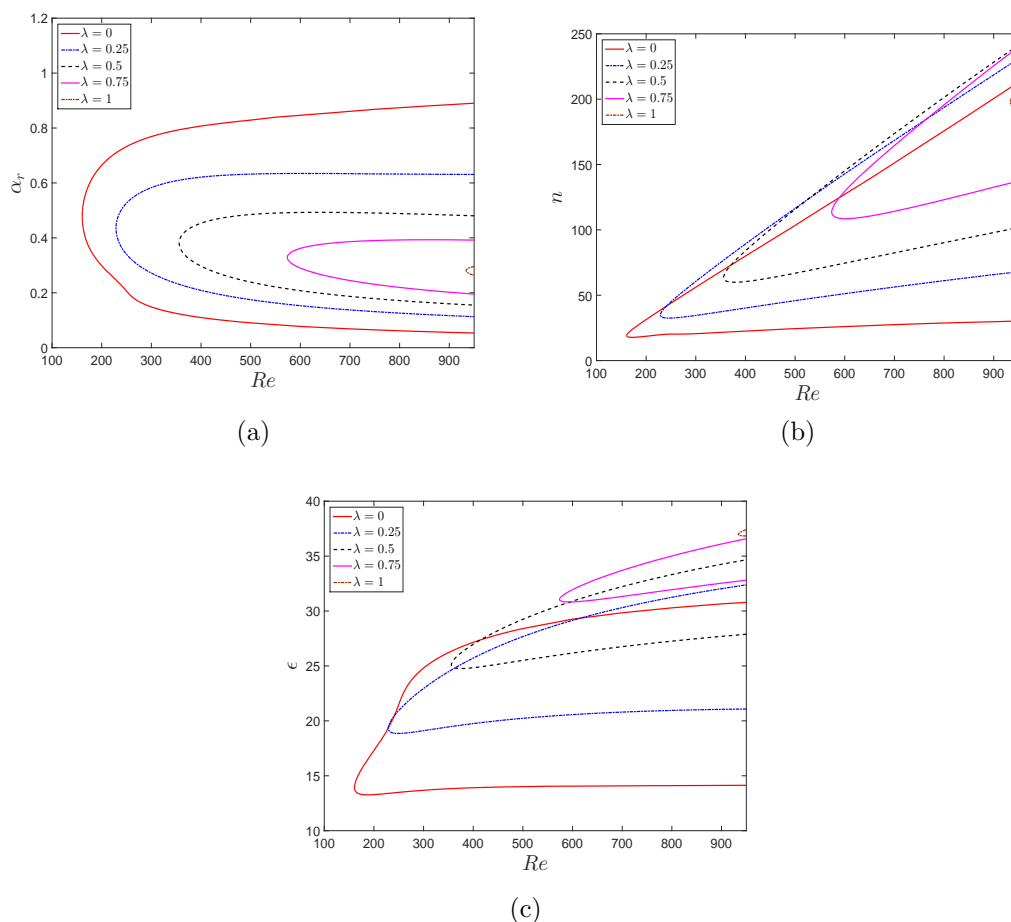


Figure 4.9: Neutral curves of the convective instability for  $Ro = -0.5$  in the case of azimuthally-anisotropic roughness (radial grooves,  $\eta = 0$ ).

curve vanishes immediately in the presence of even modest levels of roughness. In other words, the Type II mode is suppressed and the Type I mode is the dominant instability mechanism for the von Kármán flow in the case of azimuthally anisotropic roughness. The two other parameters that are helpful to understand the effects of surface roughness are the number of the stationary vortices  $n$  and the vortex angle  $\epsilon$ . Figures 4.8(b)-(c) show that the number of vortices  $n$  and the vortex angle  $\epsilon$  substantially increase along both the upper and lower branches in contrast with the strong stabilizing effect for increased roughness. Further analysis of these curves has been discussed by Cooper *et al.* (2015).

We then produce neutral curves of the related flow of the BEK system for  $Ro = -0.5$  in which both the disk and the fluid rotate with different angular velocities.

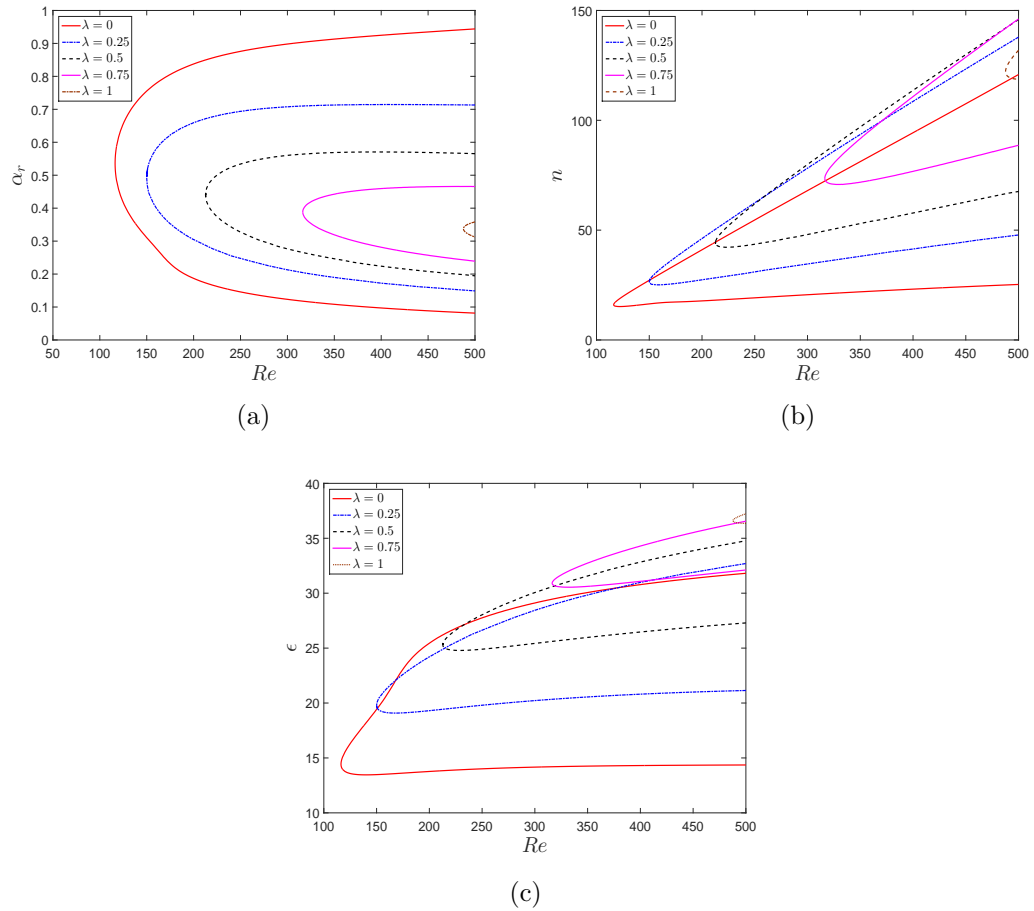


Figure 4.10: Neutral curves of the convective instability of the Ekman flow in the case of azimuthally-anisotropic roughness (radial grooves,  $\eta = 0$ ).

Figure 4.9(a) shows the strong stabilisation effect of radial grooves on both of the instability modes and the Type II mode vanishes as the roughness is increased. Although a stabilisation effect is observed, the convective instability of  $Ro = -0.5$  onsets at lower Reynolds numbers at each of roughness level compared to the von Kármán flow case. Moreover, it is clear from Figures 4.9(b)-(c) that the number of vortices and the vortex angle increase along both branches as in the von Kármán flow with increased roughness.

Figure 4.10 represents the neutral curves of the Ekman flow,  $Ro = 0$ , that occur when the disk and the fluid rotate with the same angular velocity,  $\Omega_D^* = \Omega_F^*$ . Figure 4.10(a) reveals that the response of the Ekman flow to radial grooves is similar to those of the previous flows discussed. Indeed, radial grooves lead to a strong

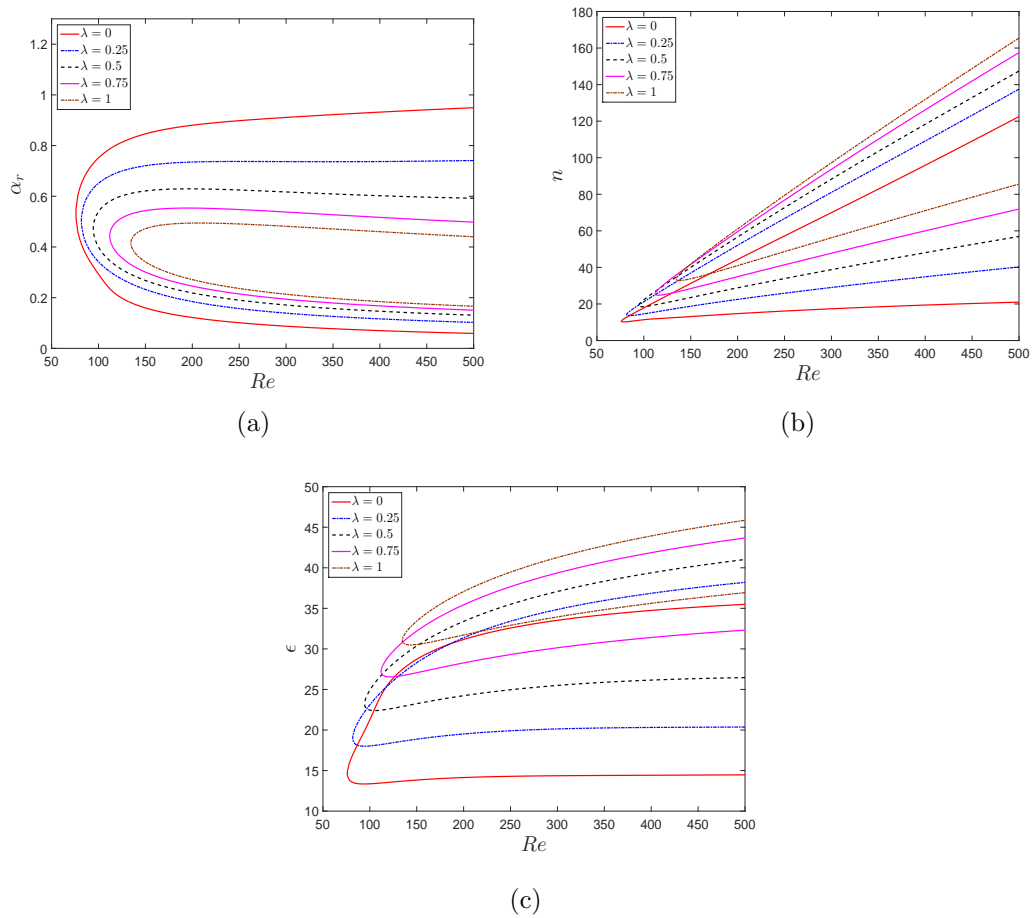


Figure 4.11: Neutral curves of the convective instability for  $Ro = 0.5$  in the case of azimuthally-anisotropic roughness (radial grooves,  $\eta = 0$ ).

stabilisation of the Type I and Type II modes in terms of the critical Reynolds number and in terms of the width of the unstable region. In other words, the onset of the convective instability is delayed to occur at a higher Reynolds number as the roughness parameter  $\lambda$  is increased. However, these critical values of Reynolds number are smaller than those of the von Kármán and  $Ro = -0.5$  flows at each particular level of azimuthally anisotropic roughness. Neutral curves of the Ekman flow in terms of the stationary vortices are represented in Figure 4.10(b). There is a slight variation in the number of vortices along the upper branch of the neutral curve and an increase in the number of vortices along the lower branch as the roughness is increased. Similarly, Figure 4.10(c) shows that behaviour of the vortex angle of the Ekman flow increases for larger values of the roughness parameter  $\lambda$ .

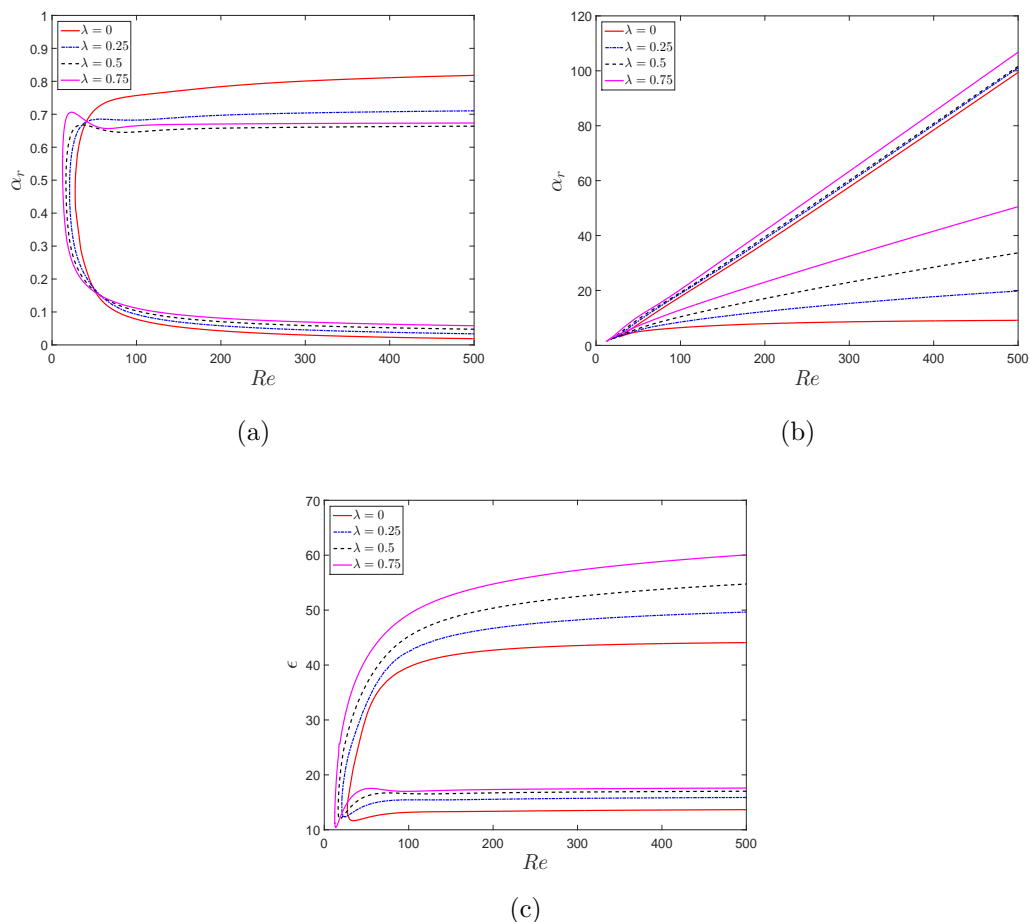


Figure 4.12: Neutral curves of the convective instability of the Bödewadt flow in the case of azimuthally-anisotropic roughness (radial grooves,  $\eta = 0$ ).

We present neutral curves of the related flow for  $Ro = 0.5$  in Figure 4.11. Figure 4.11(a) reveals that radial grooves maintain their strong stabilising effect on this flow in terms of the critical Reynolds number and the width of unstable region. However, the effect is weaker compared to the effect of radial grooves on the Ekman and the other flows of the system discussed so far in terms of critical the Reynolds number. Moreover, the two lobed structure of the neutral curves in the case of a smooth surface,  $\lambda = 0$ , again disappears for even modest levels of roughness. The increase in the number of vortices  $n$  and the vortex angle  $\epsilon$  have a similar pattern to the von Kármán and Ekman flows, as evidenced in Figures 4.11(b)-(c). That is, these values increase substantially for increased surface roughness levels.

The last flow that we discuss is the Bödewadt flow,  $Ro = 1$ , that is the case

Parameter	$Ro = 0.69$	$Ro = 0.7$	$Ro = 0.71$
$\lambda = 0$	58.32	57.38	56.46
$\lambda = 1$	61.22	58.30	55.48

Table 4.2: Critical values of observable parameters at the onset of convective instability of Type I mode for the flows around  $Ro = 0.7$ .

of the BEK system where  $\Omega_D^* = 0$  and  $\Omega_F^* \neq 0$ . Figure 4.12 shows the neutral curves of the Bödewadt flow for a radially grooved disk with roughness parameter  $\lambda = 0 - 0.75$  in 0.25 increments. The calculations could not be performed for  $\lambda = 1$  due to inconsistency of the numerical code at this level of the roughness. Only a one lobed structure is seen in the neutral curves of the Bödewadt layer. This arises from the crossflow instability, the Type I mode.

It is seen from Figure 4.12(a) that the response of the Bödewadt flow to radial grooves, azimuthally-anisotropic roughness, is completely different than for the previous flows in the system in terms of the critical Reynolds number for the onset of the Type I mode. Indeed, the response is destabilising. The critical Reynolds number is seen to be reduced as the roughness parameter  $\lambda$  increased. In contrast to the early onset of the convective instability (a clear destabilising effect), radial grooves are seen to narrow the unstable region, which is a stabilising effect in some respects.

Figure 4.12(b) represents neutral curves of the Bödewadt flow in terms of the stationary vortices. Despite the destabilisation of the critical Reynolds number, there is a slight variation in the number of vortices along the upper branch of the neutral curve and a substantial increase of the number of vortices along the lower branch as the roughness is increased. On the other hand, Figure 4.12(c) clearly details the increase in the value of vortex angle as the roughness level is increased. Therefore, the response of the Bödewadt flow to radial grooves in terms of the number of vortices and the vortex angle are similar to other flows in the system.

Comparing the effect of radial grooves on the flows of the BEK system, it can be seen that the strength of the stabilising effect is sensitive to the Rossby number and

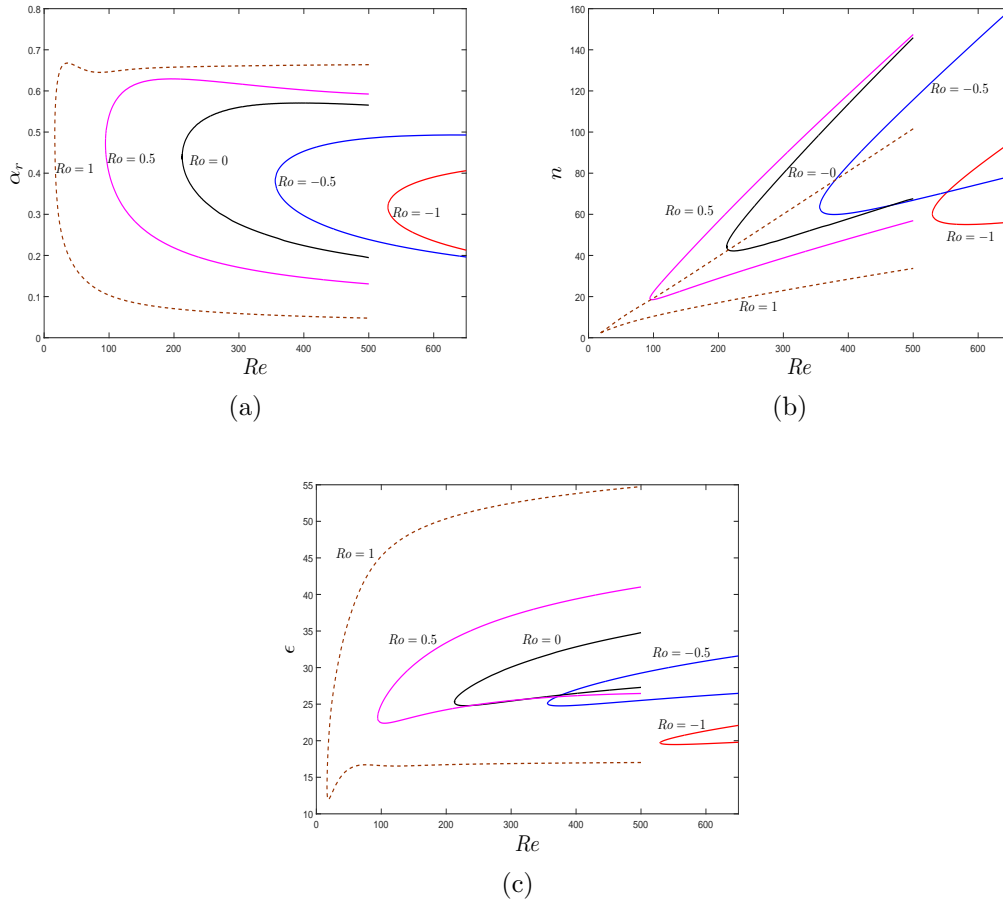


Figure 4.13: Neutral curves of convective instability for a range of flows within the BEK system in the case of a moderate value of azimuthally-anisotropic roughness parameter,  $\lambda = 0.5$ .

it is seen to decrease continuously from the von Kármán flow,  $Ro = -1$ , towards the Bödewadt flow,  $Ro = 1$  and turns to a destabilising effect after a particular Rossby number in this interval. Table 4.2 presents the critical Reynolds numbers of the Type I mode for determination of this particular point by comparing the smooth case and  $\lambda = 1$  roughness case. It is clear that the stabilizing effect of radial grooves on the onset of convective instability is reversed around  $Ro \approx 0.7$ . That is, radial grooves are stabilizing for  $Ro \in [-1, 0.7]$  with reduced sensitivity, with decreased  $Ro$ , until it turns into a destabilising effect whilst  $Ro \in (0.7, 1]$ . It is also worthwhile to compare the changes in the stability characteristic of all flows in the BEK system in the case of a moderately rough disk surface. The changes in the

case of a smooth surface are well established by Lingwood (1997). By following her idea, we present neutral curves of the related flows for a moderate level of roughness parameter,  $\lambda = 0.5$  in Figure 4.13.

Figure 4.13(a) clearly shows that the flows become increasingly unstable in terms of critical Reynolds number, and the width of the unstable region, as the Rossby number increases from the von Kármán layer,  $Ro = -1$ , to the Bödewadt layer,  $Ro = 1$ . This behaviour of the flows on a radially grooved disk is similar to that obtained in the smooth disk case (Lingwood, 1997). However, we do not obtain the two lobed structure of neutral curves for all Rossby numbers for this level of the roughness. This indicates that the Type II mode is suppressed in the case of azimuthally anisotropic roughness for all the flows within the BEK system.

Figure 4.13(b) shows the number of vortices  $n$  plotted against the Reynolds number. Clearly, the number of vortices  $n$  increases for the Rossby numbers from -1 to -0.5 and changes its behaviour when the Rossby numbers is in the range -0.5 to 1. We observe that the vortex angle at the critical Reynolds number increases continuously as the Rossby number increases from the von Kármán layer,  $Ro = -1$ , to the Ekman layer,  $Ro = 0$  and slightly decreases from the Ekman layer to the Bödewadt,  $Ro = 1$  as shown in Figure 4.13(c).

The numerical predictions of the critical parameters at the onset of convective instability for the Type I mode are presented in Table 4.3 for each flow discussed previously. The critical values of the smooth case have very close agreement with the existing results in the literature for the BEK system and those due to Cooper *et al.* (2015) for the rough rotating disk, these are taken as validation of our code.

### 4.3.2. The growth rates

We now consider the effect of radial grooves on the growth rates of the instability modes of the BEK system of boundary layer flows. However, as predicted by Lingwood & Garrett (2011) absolute instability onsets at very small Reynolds numbers in the Bödewadt flow and leads to a “branch exchange” that makes it impossible to find the location of maximum amplification of either instability modes. Therefore,

The von Kármán layer,  $Ro = -1$ 

Parameter	$Re$	$n$	$\epsilon$
$\lambda = 0$	<b>286.05</b> (460.92)	<b>22.20</b> (21.28)	<b>11.40</b> (19.28)
$\lambda = 0.25$	<b>380.68</b> (-)	<b>37.21</b> (-)	<b>15.41</b> (-)
$\lambda = 0.5$	<b>529.54</b> (-)	<b>60.12</b> (-)	<b>19.72</b> (-)
$\lambda = 0.75$	<b>724.36</b> (-)	<b>89.39</b> (-)	<b>23.46</b> (-)
$\lambda = 1$	<b>976.85</b> (-)	<b>130.39</b> (-)	<b>27.31</b> (-)

The related layer for  $Ro = -0.5$ 

Parameter	$Re$	$n$	$\epsilon$
$\lambda = 0$	<b>160.81</b> (-)	<b>19.09</b> (-)	<b>13.97</b> (-)
$\lambda = 0.25$	<b>228.85</b> (-)	<b>34.89</b> (-)	<b>19.35</b> (-)
$\lambda = 0.5$	<b>355.89</b> (-)	<b>63.78</b> (-)	<b>25.13</b> (-)
$\lambda = 0.75$	<b>573.80</b> (-)	<b>114.14</b> (-)	<b>31.08</b> (-)
$\lambda = 1$	<b>933.82</b> (-)	<b>197.54</b> (-)	<b>36.99</b> (-)

The Ekman layer,  $Ro = 0$ 

Parameter	$Re$	$n$	$\epsilon$
$\lambda = 0$	<b>116.26</b> (-)	<b>16.04</b> (-)	<b>14.33</b> (-)
$\lambda = 0.25$	<b>149.99</b> (-)	<b>26.60</b> (-)	<b>19.48</b> (-)
$\lambda = 0.5$	<b>212.70</b> (-)	<b>44.30</b> (-)	<b>25.21</b> (-)
$\lambda = 0.75$	<b>316.38</b> (-)	<b>73.55</b> (-)	<b>30.37</b> (-)
$\lambda = 1$	<b>487.69</b> (-)	<b>122.18</b> (-)	<b>36.67</b> (-)

The related layer for  $Ro = 0.5$ 

Parameter	$Re$	$n$	$\epsilon$
$\lambda = 0$	<b>75.89</b> (-)	<b>10.52</b> (-)	<b>14.63</b> (-)
$\lambda = 0.25$	<b>81.75</b> (-)	<b>14.18</b> (-)	<b>18.99</b> (-)
$\lambda = 0.5$	<b>94.47</b> (-)	<b>19.19</b> (-)	<b>23.19</b> (-)
$\lambda = 0.75$	<b>112.02</b> (-)	<b>25.52</b> (-)	<b>27.26</b> (-)
$\lambda = 1$	<b>134.57</b> (-)	<b>33.59</b> (-)	<b>31.07</b> (-)

The Bödewadt layer,  $Ro = 1$ 

Parameter	$Re$	$n$	$\epsilon$
$\lambda = 0$	<b>27.38</b> (-)	<b>3.12</b> (-)	<b>14.32</b> (-)
$\lambda = 0.25$	<b>20.82</b> (-)	<b>2.53</b> (-)	<b>14.90</b> (-)
$\lambda = 0.5$	<b>16.40</b> (-)	<b>1.99</b> (-)	<b>13.75</b> (-)
$\lambda = 0.75$	<b>12.41</b> (-)	<b>1.45</b> (-)	<b>12.03</b> (-)

Table 4.3: Critical values of observable parameters at the onset of convective instability of both modes for the boundary layers in the BEK system in the case of azimuthally-anisotropic roughness (radial grooves). Type I and (Type II). The most dangerous mode is indicated as bold text in terms of critical Reynolds number.

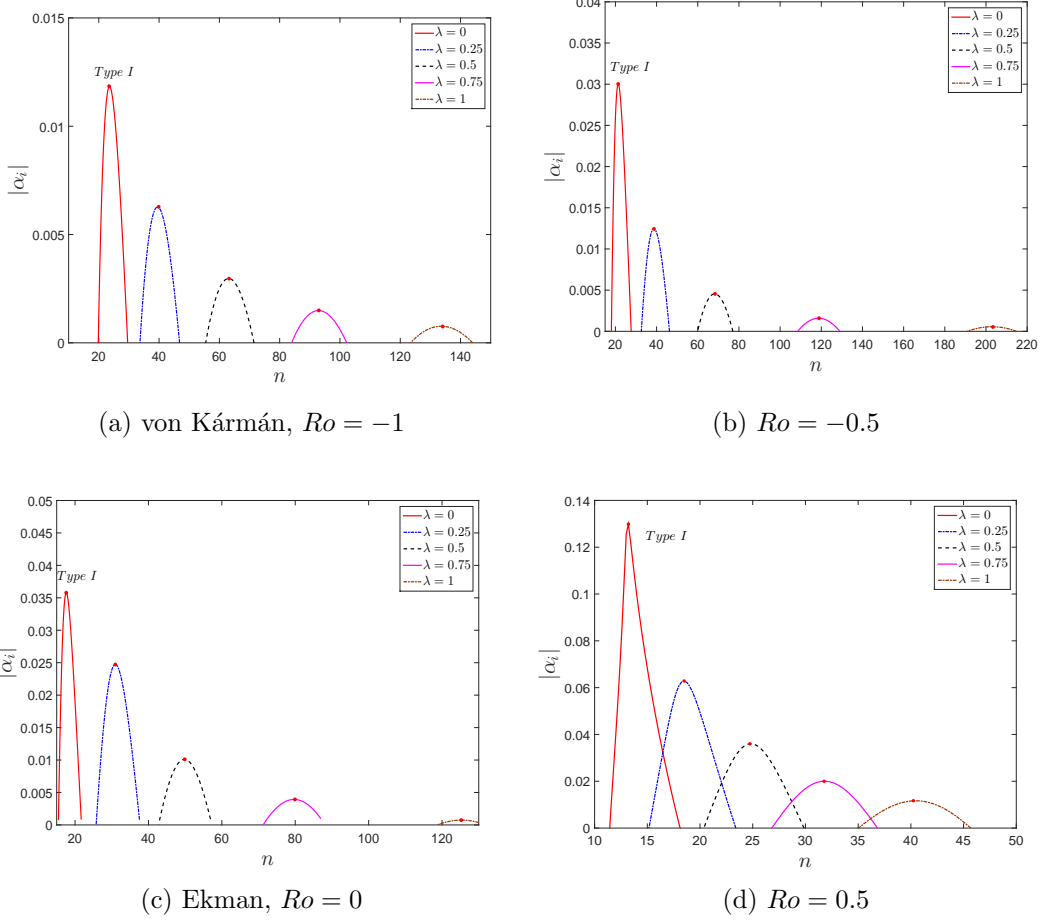


Figure 4.14: Growth rates of Type I instability mode within the BEK boundary layer flows as a function of the vortex number  $n$  at  $Re = Re_{critical} + 25$  in the case of radial grooves, azimuthally-anisotropic roughness. The red dots indicate the most rapidly growing mode.

equivalent plots of the convective growth rates at some level of roughness for the Bödewadt flow are not possible to produce.

The growth rate of the instability modes is measured as the absolute value of the negative imaginary part of the radial wavenumber,  $|\alpha_i|$ , at the particular values of number of vortices  $n$ . Since the Type II mode vanishes at even modest levels of radial grooves in each flow of the BEK system, we only present here the growth rates of the Type I instability mode. Figure 4.14 shows growth rates of the Type I instability mode within these layers at  $Re = Re_{critical} + 25$ , at a fixed distance into the neutral curve, as a function of the vortex number  $n$  for each level of roughness. Figure 4.14 clearly shows the stabilising effect of radial grooves on the Type I mode

of each flow. Furthermore, the most rapidly growing mode is of particular interest as it would be the most likely to dominate and be observed in experiments. Clearly, it can be determined from this presentation of the growth modes. The figure shows that the maximum growth rate shifts to higher values of  $n$ , indicating an increase in the number of vortices as an effect of increased surface roughness level. In contrast to that substantial increase, the value of the maximum growth rate decreases for increased roughness, that is a stabilising effect of the roughness.

These results are consistent with the critical parameters obtained for each layer as stated in Table 4.3. A similar discussion of the growth rates for the von Kármán flow has been provided by Cooper *et al.* (2015) and we include our results for this flow as a validation.

## 4.4. Energy Analysis

In this section, we present the results of solving the energy balance equation (2.50) following the work of Cooper & Carpenter (1997), Cooper *et al.* (2015), and Garrett *et al.* (2016) for the three-dimensional disturbances  $(\hat{u}, \hat{v}, \hat{w}, \hat{p})$  of the three-dimensional mean flow  $(U, V, W)$  in the case of azimuthally anisotropic surface roughness. The aim is to establish the underlying physical mechanisms behind the effects of radially grooved disks on the BEK system of boundary layer flows.

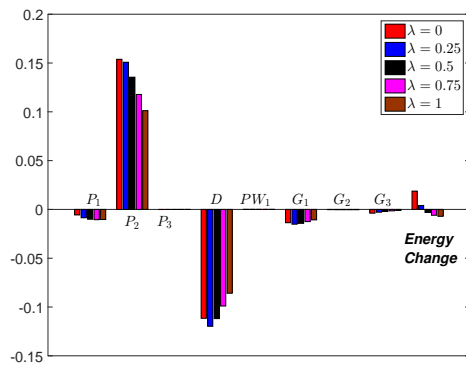
We begin by considering the energy balance equation (2.49) of any eigenmode of the perturbation equations (2.40)-(2.41). The positive terms in that equation contribute to the energy production whereas the negative terms remove energy from the system. The eigenmode is amplified ( $\alpha_i < 0$ ) if energy production exceeds the energy dissipation in the system. The effect of surface roughness on the instability modes can be interpreted from this formulation by calculating the energy change of the system, that is the sum of the energy production and dissipation terms. Increased energy change for higher values of the roughness parameters indicates a destabilisation effect on the modes. In contrast a reduced energy change indicates a stabilisation effect. However, as discussed in §4.3.1, the Type II mode disappears

at even modest sizes of radial grooves in each flow of the BEK system. Therefore, we only discuss the energy balance for the Type I mode in the case of azimuthally anisotropic roughness.

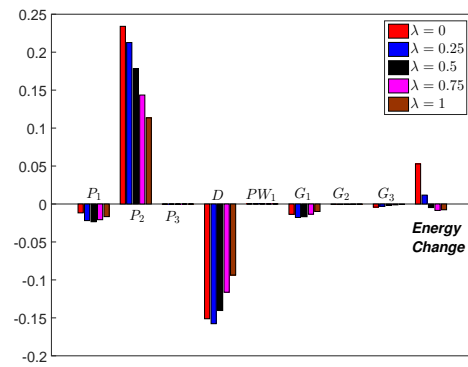
We perform energy balance calculations for the BEK system of boundary layer flows at the location of the maximum amplification discussed in the previous section at  $Re = Re_{critical} + 25$ . Here  $Re_{critical}$  is the critical Reynolds number presented in Table 4.3 for the onset of the Type I mode of instability. However, as predicted by Lingwood & Garrett (2011) absolute instability onsets at very small Reynolds numbers in the Bödewadt flow and leads to a “branch exchange” that makes it impossible to find the location of maximum amplification of either instability mode. Therefore, we instead perform the energy balance calculations for the Bödewadt flow at fixed  $Re = 400$  with number of vortices  $n = 85$  for the Type I mode. This value of  $n$  is chosen such that the point of interest is outside of the absolutely unstable region at  $Re = 400$ .

Figure 4.15 shows the energy balance calculations for a range radial grooved disks. Here, the results are normalized by the mechanical energy flux of the most energetic mode within each figure and so comparisons can be made at different values of  $\lambda$ . Two different figures can not however be directly compared. Clearly, there is a stabilisation effect on the Type I mode for the flows of  $Ro = -1, -0.5, 0$ , and  $0.5$ . This effect arises mainly from the reduction in the energy production term  $P_2$  and in the energy dissipation term  $D$ . However, it is also worth noting that the reductions in these terms decrease while the Rossby number changes from negative values to positive values. Moreover, after a certain value of the Rossby number these terms begin to increase. Also, the energy removing effects of the terms arising from the streamline curvature effects and the three dimensionality of the mean flow turns into an energy production for positive values of the Rossby number. In other words, these terms contribute to energy production in the system. As a result, destabilisation effects are observed for the Bödewadt flow as is evidenced in the Figure 4.15(e).

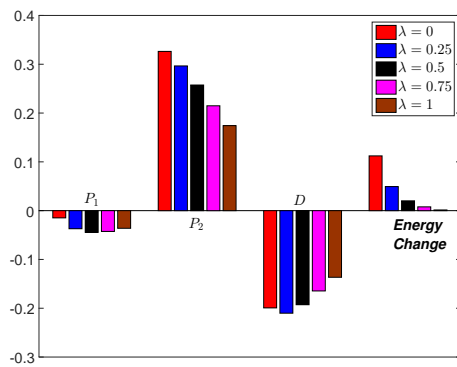
As proposed by Cooper *et al.* (2015) some explanations about the energy trends of the BEK system of flows can be provided by analysing the form of the disturbance



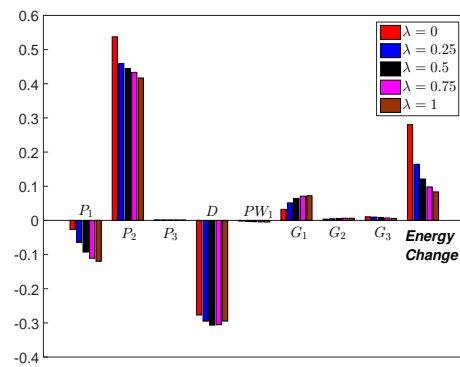
(a) von Kármán,  $Ro = -1$



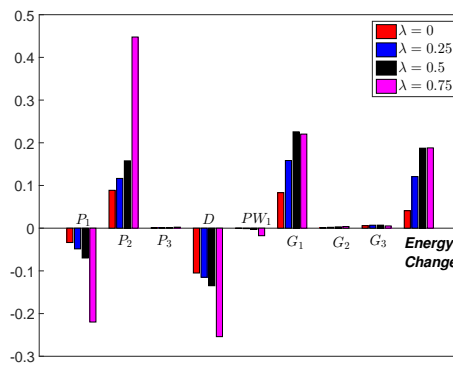
(b)  $Ro = -0.5$



(c) Ekman,  $Ro = 0$



(d)  $Ro = 0.5$



(e) Bödewadt,  $Ro = 1$

Figure 4.15: Energy balance at the location of maximum amplification of the BEK boundary layer flows at  $Re = Re_{critical} + 25$ , except the Bödewadt flow for radially anisotropic roughness. For the Bödewadt flow,  $Re = 400$  and  $n = 85$ . The terms are normalised by the mechanical energy flux of the most dangerous mode within each figure.

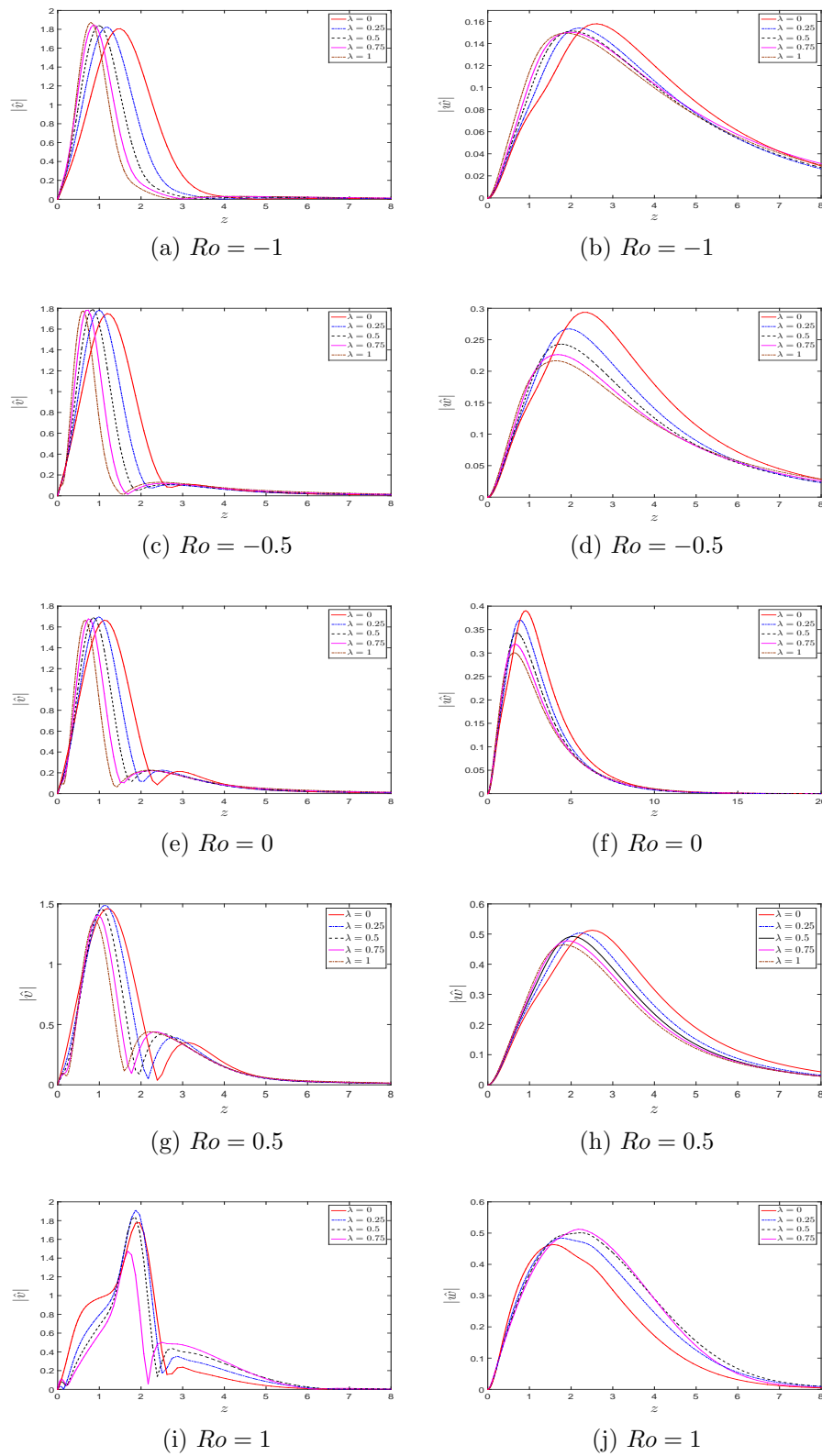


Figure 4.16: Type I mode profiles for the azimuthal and the axial disturbance velocity profiles of the BEK flows at the location of maximum amplification of the BEK boundary layer flows in the case of a radially grooved disk at  $Re = Re_{critical} + 25$ , except for the Bödewadt flow for radially anisotropic roughness. For the Bödewadt flow,  $Re = 400$  and  $n = 85$ .

	Ekman flow, $Ro = 0$	Bödewadt flow, $Ro = 1$
$\lambda = 0$	219 ~ 220	27 ~ 28
$\lambda = 0.25$	932 ~ 933	20 ~ 21
$\lambda = 0.5$	> 1000	15 ~ 16
$\lambda = 0.75$	> 1000	12 ~ 13
$\lambda = 1$	> 1000	not applicable

Table 4.4: Critical Reynolds number for the stationary Type I mode interacting with the absolute instability region inside the neutral curves of the BEK system of flows in the case of radial grooves.

velocity profiles. The important disturbance profiles are the azimuthal velocity perturbation,  $\hat{v}$ , and the axial velocity perturbation,  $\hat{w}$ , which contribute to the dominant energy production term  $P_2$ . The magnitudes of these two disturbance profiles are presented in Figure 4.16 for the BEK system of flows in the case of a radially grooved disk for the Type I instability mode. It is seen from this figure that the general form of both the disturbance profiles are not changed with the profiles being simply translated towards the wall as the roughness is increased. The strong decrease of the  $P_2$  term for the flows with negative Rossby numbers, including  $Ro = 0$ , is due to a reduction in the amplitude of the axial velocity perturbation,  $\hat{w}$ . For the positive Rossby number flows, the decrease of the  $P_2$  term is due to the reductions in the amplitude of the disturbance profiles  $\hat{v}$  and  $\hat{w}$  with increased roughness.

## 4.5. Absolute instability

Mack (1985) showed the existence of another linear instability mode, the Type III mode, in rotating-disk boundary layer flows. As identified by Lingwood (1997), the Type III mode coalesces with a travelling Type I cross-flow instability mode and generates a local absolute instability. If one of the coalescing modes can be suppressed,

the onset of absolute instability could be delayed to higher Reynolds numbers. However, the effects of surface roughness on the absolute instability should be considered in an additional and highly focused study which includes consideration of all traveling Type I modes. This is beyond the scope of this study as we remain concerned with only stationary Type I modes. In view of our study, the absolute instability mechanism limits our findings as it leads to a “branch exchange” that makes it impossible to determine the location of maximum amplification in any instability modes. We therefore are not able to produce growth rate curves of the instability modes and conduct an energy analysis at the location of the maximum amplification when the convective instability region is crossed by the absolute instability region at a particular Reynolds number.

Table 4.4 shows the critical Reynolds numbers at which the convective instability region starts to interact with the absolute instability in the case of radial grooves for the Ekman and Bödewadt flows. It is clear that the onset of the interaction is delayed extensively to higher Reynolds number for the Ekman flow compared to the smooth cases. We do not observe the interactions for  $\lambda \geq 0.5$  up to  $Re = 1000$  which is consistent with a strong delaying effect. However, radial grooves seem not to be effective in the case of the Bödewadt flow,  $Ro = 1$ , consistent with the observed destabilisation effect of roughness on this flow. Indeed, these results lead to the prediction that azimuthally anisotropic surface roughness can be used to restrict the onset of absolute instability to higher Reynolds numbers compared to a smooth disk for the majority of the BEK flows.

## 4.6. Conclusion

In this chapter we have investigated the effects of azimuthally anisotropic roughness (radial grooves) on the convective instability of stationary disturbances in the BEK family of boundary layer flows. We have presented solutions of the mean flow equations obtained using the partial-slip approach of Miklavcic & Wang (2004) without modification. The computed mean flow components are in strong agreement

with those in the literature for the smooth surface cases at all values of  $Ro$ . The computed mean flow components of the von Kármán flow for the azimuthally rough disk surfaces are identical to those presented by Cooper *et al.* (2015). Our findings have revealed that azimuthally-anisotropic roughness acts to increase the amplification of the oscillatory behaviour of the steady flows through the axial direction and also increase the magnitudes of the radial and wall jets.

We then conducted a linear stability analyses and revealed that azimuthally-anisotropic roughness has a strong stabilising effect on both the Type I and Type II instabilities in terms of postponing the onset of the convective instability and width of the unstable area enclosed by the neutral curves for  $Ro \in [-1, 0.7]$ , although it has a marginally destabilising effect for  $Ro \in (0.7, 1]$ . This rather disappointing destabilising result might be a result of significantly increased oscillatory behaviour of the mean flow solutions as Rossby number is increased towards 1.

For the number of the vortices  $n$  and the vortex angle  $\epsilon$  we have seen that increased surface roughness at all  $Ro$  acts to increase these parameters. We have also presented supporting results to the effects of radial grooves by considering the growth rates of each instability mode and have conducted an energy balance analysis at the locations of the maximum amplifications for particular flows in the system. Our findings indicate that azimuthally anisotropic surface roughness could be a possible stabilisation mechanism that could be used to delay the onset of absolute instability on the majority of the BEK system flows.

The observed stabilising effect of radial grooves on the instability modes are similar to effects of other flow-control methodologies for the BEK system: the surface suction technique as studied theoretically by Lingwood & Garrett (2011) and imposing increased uniform magnetic field normal to the disk as studied by Jasmine & Gajjar (2005). Furthermore, we find that the response of the physical mechanisms that lead to transition in the boundary layer is sensitive to the Rossby number of the system as with the surface suction technique.

# Chapter 5

## Effect of radially anisotropic roughness on the BEK family of boundary layers

### 5.1. Overview

This chapter is concerned with the effects of radially anisotropic roughness - concentric grooves - on the convective instability mechanism within the general class of rotating BEK boundary-layers. Viscous and streamline-curvature effects are included and local linear stability analyses are conducted for the boundary-layer flows parametrised by a Rossby number  $Ro$  between minus unity to positive unity. Furthermore, an energy analysis is performed to confirm the results of linear stability analysis.

In §5.2 the effects of concentric grooves on the solutions of the steady mean flow equations are described, and the convective instability analysis is discussed in §5.3. We produce the neutral curves based on the solutions of the perturbation equations (2.40) -(2.41) in §5.3.1, and discuss the effects of surface roughness on the growth rates,  $|\alpha_i|$ , of each instability mode in §5.3.2. The results of the energy analysis are presented in §5.4. Finally, absolute instability is discussed briefly in §5.5.

## 5.2. The steady mean flow solutions



Figure 5.1: Concentric grooves over a disk.

The purpose of this section is to present the solutions of the steady mean flow equations (2.18) with the primary aim of investigating the effects of the radially anisotropic roughness on the mean flow profiles of the BEK family of the boundary layers. The secondary aim of this section is to compare these effects with those of other passive drag control mechanisms applied to the BEK system of flows; the surface suction technique studied by Lingwood & Garrett (2011) and the uniform distribution of a magnetic field studied by Jasmine & Gajjar (2005).

The radially anisotropic surface roughness has a pattern of concentric circles - concentric grooves - on the disk. These grooves can be modelled mathematically by setting roughness parameters in the partial-slip boundary conditions (2.19) obtained under the MW model to  $\eta > 0$ ,  $\lambda = 0$ . The governing equations of the steady mean flow profiles of each boundary layer in the BEK system are distinguished by the Rossby number. For each non-zero Rossby number flow within the system, the MATLAB function described in §3.1 is used to solve these governing equations. However, we do not need to perform numerical computations for the case when  $Ro = 0$ , the Ekman flow, as there are precise analytical solutions of each mean flow component for the zero Rossby number flow which are stated in (2.20).

We present computed mean flow profiles for different sizes of concentric grooves. The radial mean flow component  $U$  is presented in Figures 5.2(a)-5.6(a) and the

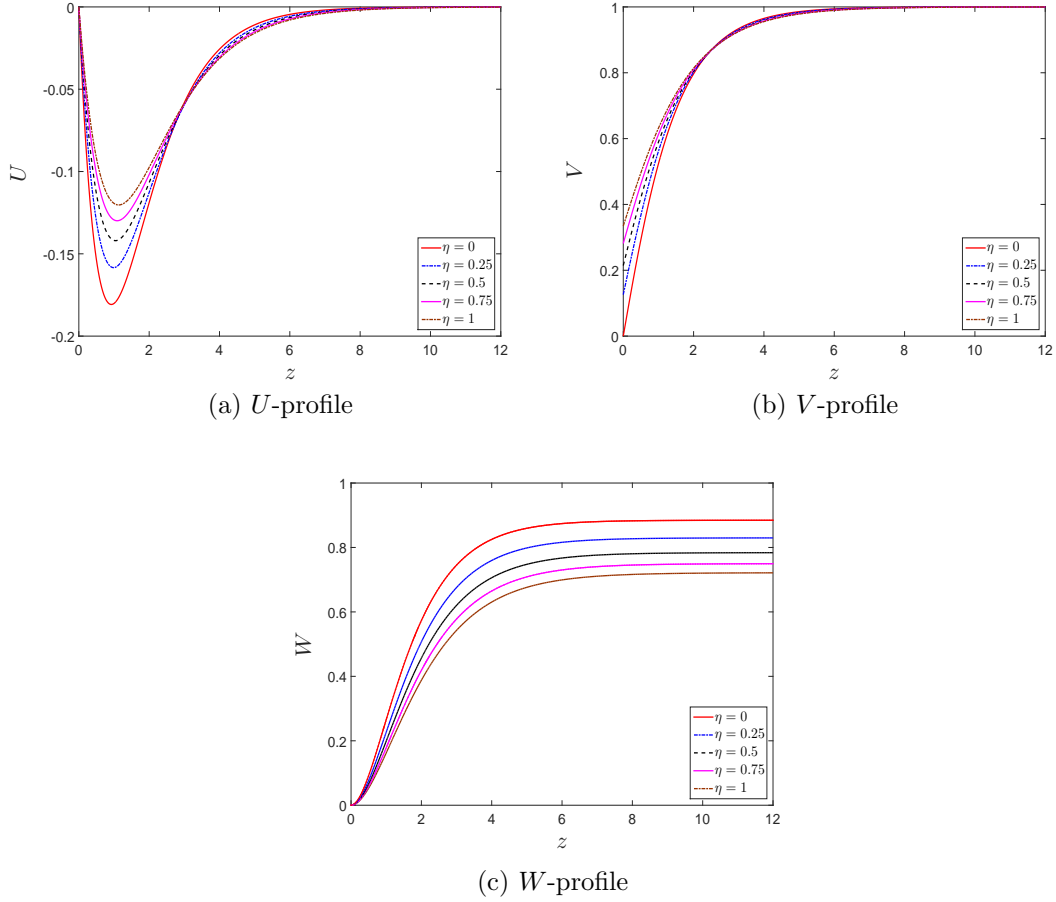


Figure 5.2: Mean-flow components of the von Kármán flow in the case of radially-anisotropic roughness (concentric grooves,  $\lambda = 0$ ).

azimuthal mean flow profile  $V$  is presented in Figures 5.2(b)-5.6(b). The last flow component  $W$ , in the axial direction, is presented in Figures 5.2(c)-5.6(c). The initial values of  $U'(0)$  and  $V'(0)$  are important for the computation of the flow profiles and the resisting torque  $T$  given in (2.21). They are shown in Table 5.1 for various values of roughness parameter  $\eta$ . Our initial values for the von Kármán flow are identical to those presented by Miklavcic & Wang (2004).

The oscillatory behaviour of each mean flow component of the BEK system, that is related to the Type I instability mechanism (Saric & Reed, 2003), is damped for increased surface roughness, as evidenced in Figures 5.2-5.6. This observation is similar to the effects of increased surface suction (Lingwood & Garrett, 2011) and an increase in the uniform magnetic field applied to the von Kármán flow (Jasmine &

The von Kármán flow,  $Ro = -1$

Parameter	$U'(0)$	$V'(0)$
$\eta = 0$	-0.510232616	0.615922011
$\eta = 0.25$	-0.417886378	0.504189321
$\eta = 0.5$	-0.355262334	0.428851249
$\eta = 0.75$	-0.310814547	0.375196569
$\eta = 1$	-0.277059262	0.3344449236

$Ro = -0.5$

Parameter	$U'(0)$	$V'(0)$
$\eta = 0$	-0.857041159	0.907317540
$\eta = 0.25$	-0.69137509	0.72627144
$\eta = 0.5$	-0.582170759	0.60805155
$\eta = 0.75$	-0.504040307	0.52410114
$\eta = 1$	-0.445066659	0.46112063

$Ro = 0.5$

Parameter	$U'(0)$	$V'(0)$
$\eta = 0$	-1.017626469	0.961193351
$\eta = 0.25$	-0.823188578	0.788230126
$\eta = 0.5$	-0.688203415	0.664651107
$\eta = 0.75$	-0.590018117	0.573151874
$\eta = 1$	-0.515770753	0.503128977

The Bödewadt flow,  $Ro = 1$

Parameter	$U'(0)$	$V'(0)$
$\eta = 0$	-0.941970896	0.772885383
$\eta = 0.25$	-0.780006850	0.677381629
$\eta = 0.5$	-0.662521420	0.594817650
$\eta = 0.75$	-0.573875981	0.526317744
$\eta = 1$	-0.505093817	0.470038322

Table 5.1: The initial values of  $U'$  and  $V'$  at the disk surface for various  $Ro$  (concentric grooves,  $\lambda = 0$ ).

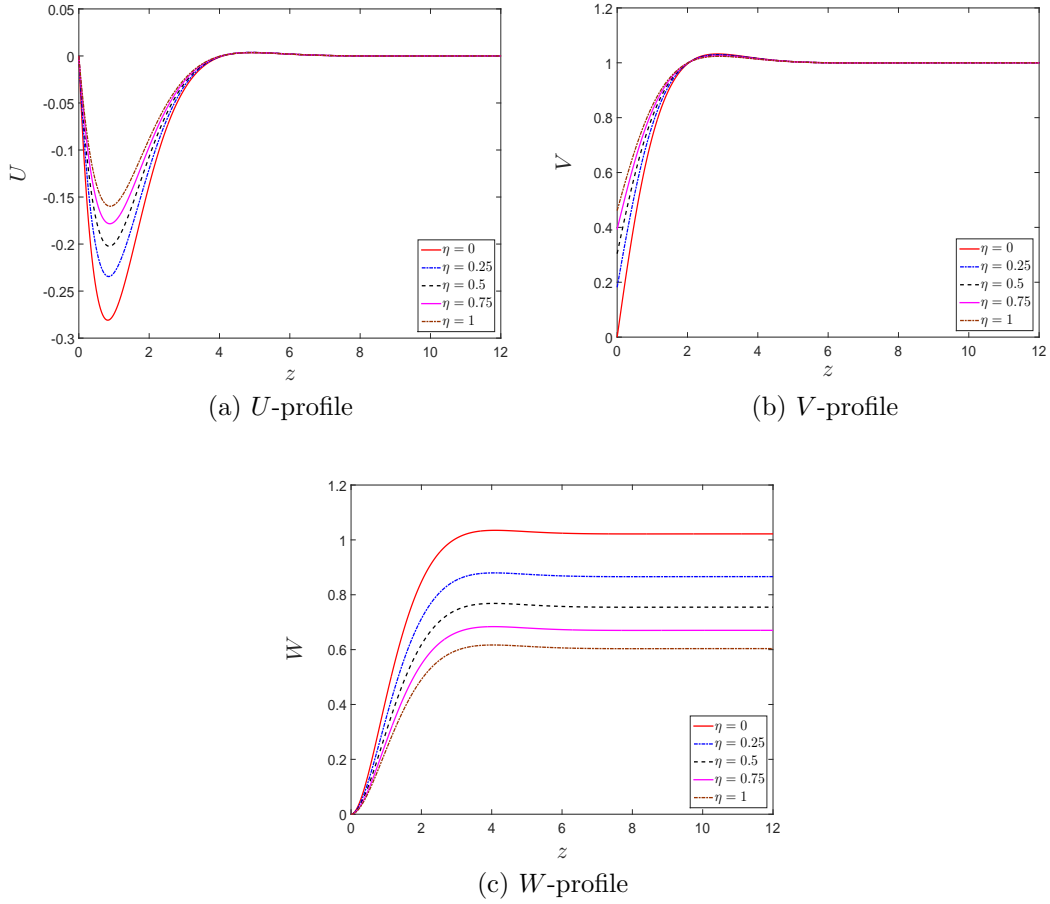


Figure 5.3: Mean-flow components for  $Ro = -0.5$  in the case of radially-anisotropic roughness (concentric grooves,  $\lambda = 0$ )

Gajjar, 2005). Both studies observe a reducing in the magnitude of the oscillations in each mean flow component with an increase in their parameters.

Figures 5.2(a)-5.6(a) clearly show the reduction in the magnitude of the radial wall jet with an increase in concentric grooves for all flows in the BEK system. This is physically reasonable as the friction holding back the radial wall jet would be increased by concentric grooves as it moves along the radial direction, Garrett *et al.* (2016). The reduction rate of the radial wall jet on the other hand increases substantially with increased  $\eta$  as  $Ro$  changes from -1, the von Kármán flow, to 1, the Bödewadt flow. However, the location of the maximum value of  $U$  remains nearly unchanged for negative Rossby flows, but moves slightly towards the disk surface for positive Rossby flows as roughness is increased. We observe that the boundary

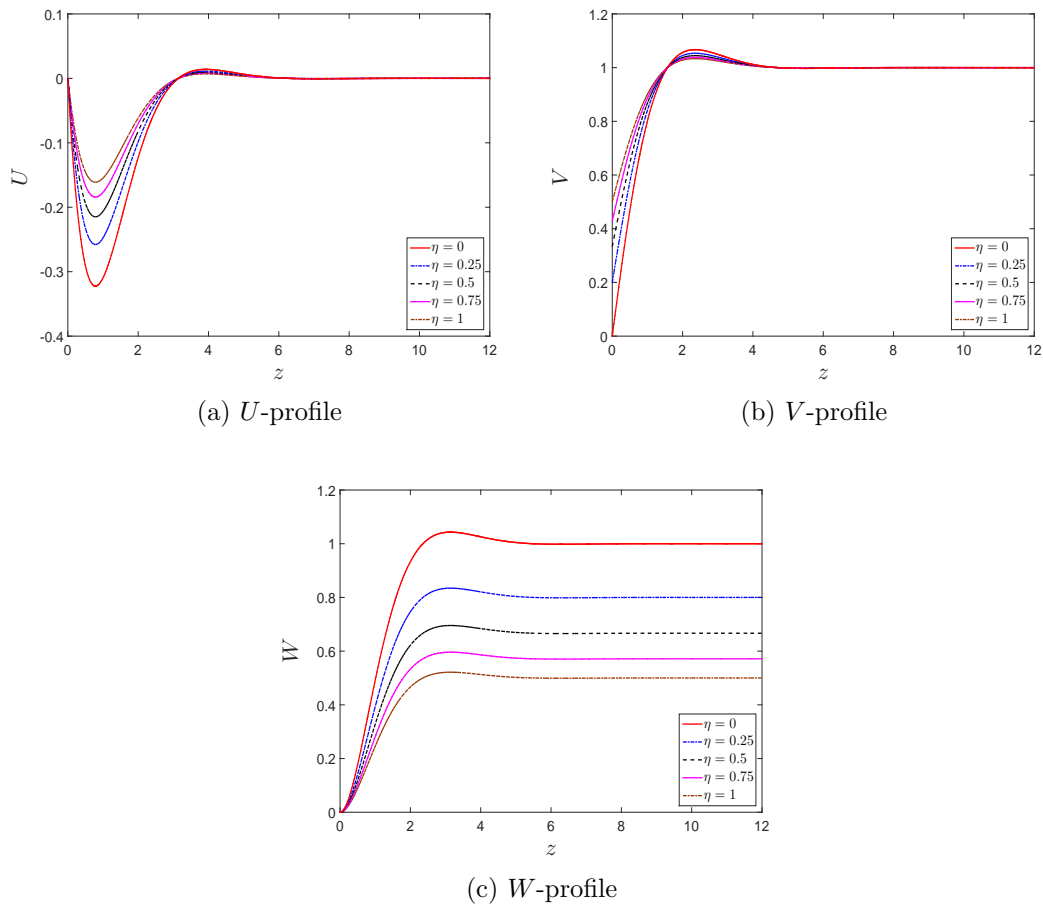


Figure 5.4: Mean-flow components of the Ekman flow ( $Ro = 0$ ) in the case of radially-anisotropic roughness (concentric grooves,  $\lambda = 0$ ).

layer thickness for positive  $Ro$  reduces for increased roughness. These changes of the  $U$  profile are similar to those observed in the smooth case for increased surface suction and increased uniform magnetic field techniques.

It is seen from Figures 5.2(b)-5.6(b) that the wall value of the azimuthal velocity profile  $V$  increases for all flows with increased roughness as a direct implication of the partial slip boundary conditions (2.19) as  $\eta \neq 0$ , and this effect is in contrast to the radially grooved case. Indeed, a decrease is noted in Table 5.1 for the initial value of the derivative of this component. This leads to a substantial decrease at the resisting torque  $T$  for all  $Ro \neq 0$ , similar to the results of Miklavcic & Wang (2004) in case of the von Kármán flow.

Figures 5.2(c)-5.6(c) demonstrate that increased concentric grooves reduce sub-

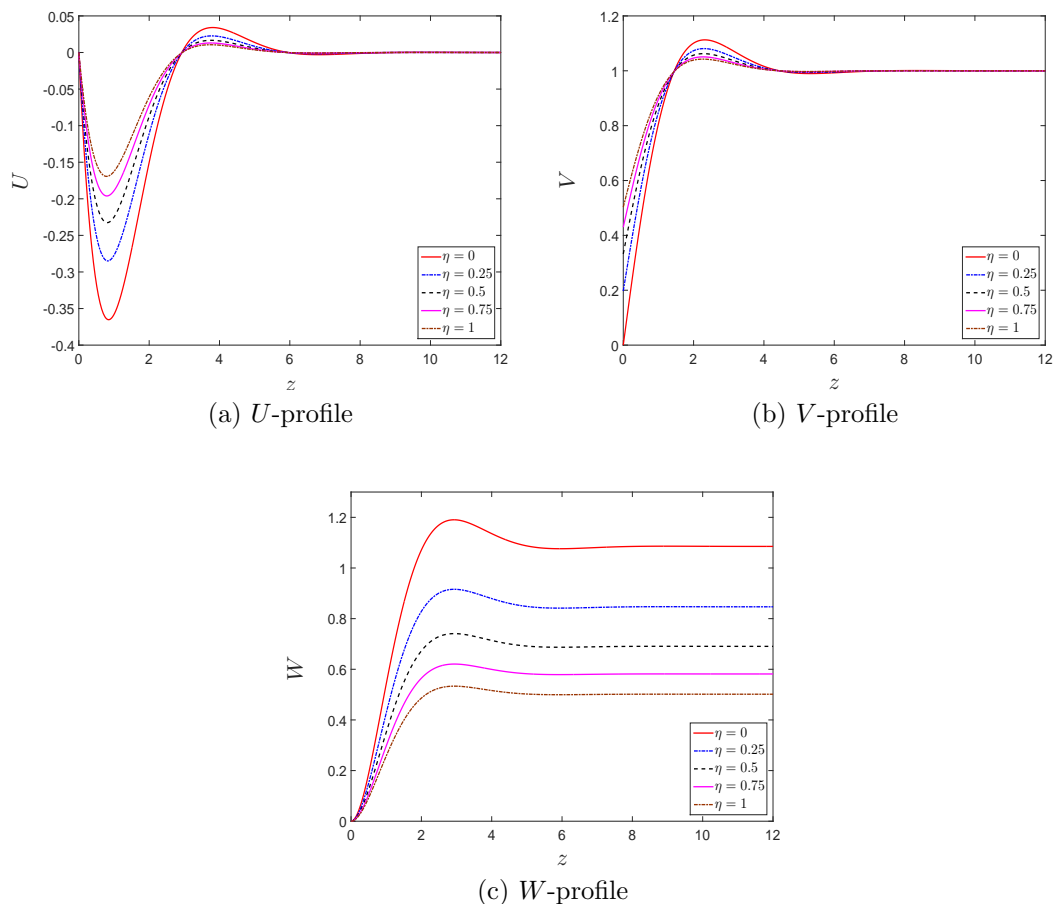


Figure 5.5: Mean-flow components for  $Ro = 0.5$  in the case of radially-anisotropic roughness (concentric grooves,  $\lambda = 0$ ).

stantially the magnitude of axial flow for all flows of the BEK system, that is in parallel to the findings of Lingwood & Garrett (2011) for increased surface suction for  $Ro \geq 0$  and those of Jasmine & Gajjar (2005) for increased uniform magnetic field. In other words, the amount of flow entrained into the boundary layer reduces for all  $Ro$  as the roughness is increased.

Our main findings in this section for the mean flow components of each particular flow in the BEK system indicate that the effect of anisotropic roughness with concentric grooves on the radial jet are consistent with those obtained by Cooper *et al.* (2015) for the von Kármán flow. That is, the increased concentric grooves act to decrease the magnitude of the radial jet. Furthermore, the effects of increased roughness on the oscillatory behaviours of the flow components are similar to the

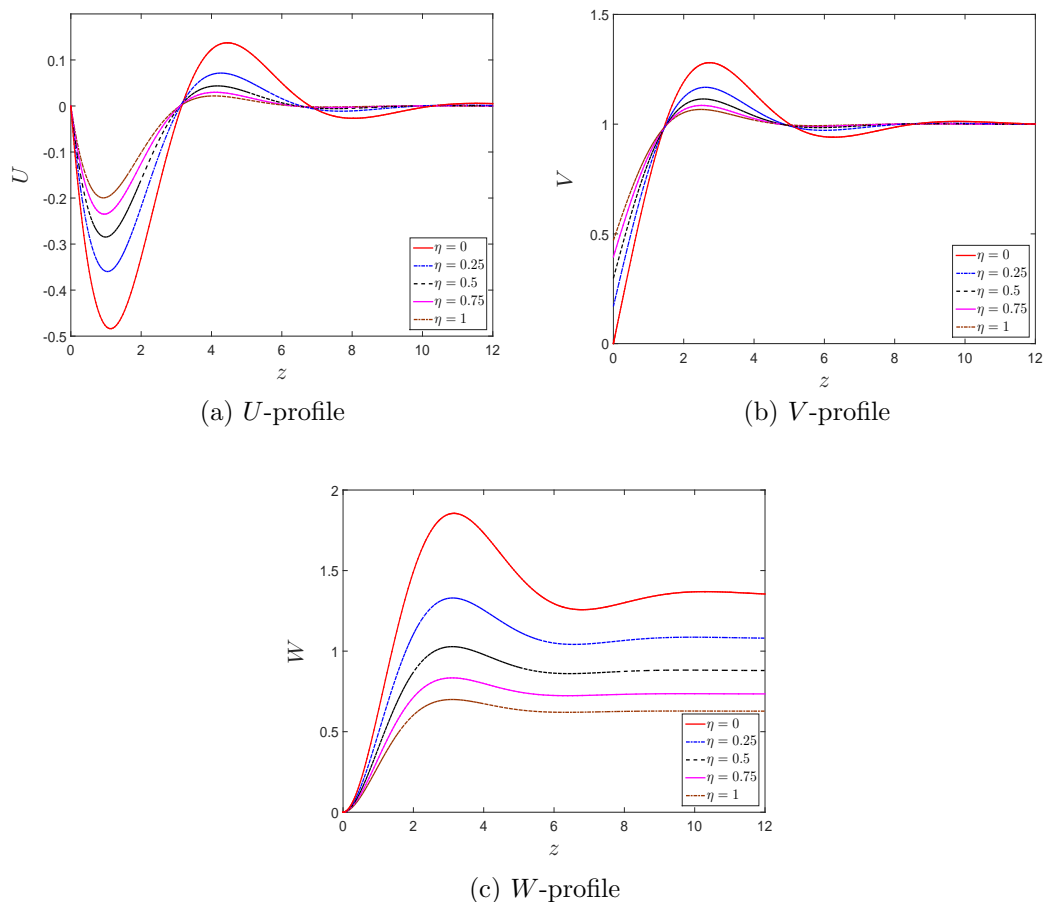


Figure 5.6: Mean-flow components of the Bödewadt flow ( $Ro = 1$ ) in the case of radially-anisotropic roughness (concentric grooves,  $\lambda = 0$ ).

responses seen to surface mass flux and the distribution of a uniform magnetic field. Similarly, a decrease in the amount of the fluid entrained inside the boundary layers are observed for all flows in the BEK system. The torque  $T$  also decreases with increased concentric grooves.

### 5.3. The convective instability analysis

This section is concerned with the occurrence of convective instabilities in the case of the concentric grooves distributed over the rotating disk. The convective instability is determined by the computed solutions of the perturbation equations (2.40)-(2.41) using the spectral Chebyshev method described in §3.2. We analyse

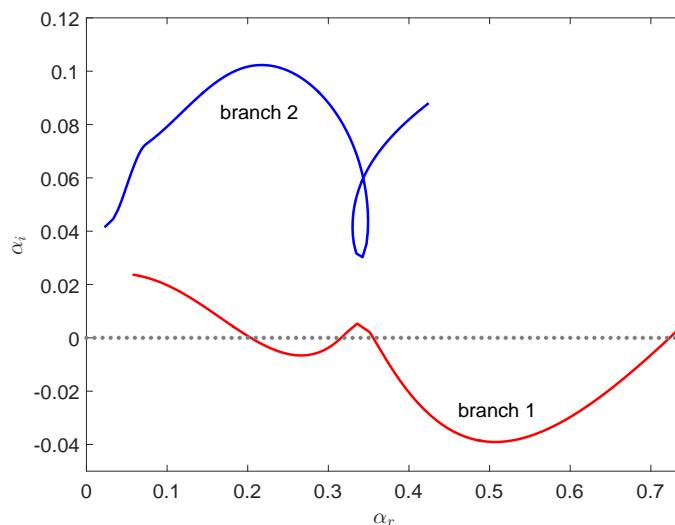


Figure 5.7: The two spatial branches after the exchange showing regions of both streamline-curvature and crossflow instability at  $Re = 195$  for the Ekman flow in the case of  $\eta = 0.5$ .

the characteristics of convective instability in terms of neutral curves in §5.3.1 and the growth rates of both the Type I and Type II modes in §5.14. We suppose in the first instance that the flow is not absolutely unstable. As a result, in the Briggs-Bers procedure we can set the imaginary part of the frequency to zero, so that  $\omega_i = 0$ .

### 5.3.1. Neutral curves

In this section, the neutral curves for the boundary layer flows belonging to the BEK system are presented in the  $(Re, \alpha_r)$ ,  $(Re, n)$  and  $(R, \epsilon)$ -planes in the case of radially anisotropic surface roughness. Each curve encloses a convectively unstable region. Two spatial branches determining the convective instability characteristics of each flow are found in this case. Figure 5.7 shows two spatial branches of the Ekman flow as an example in the case of moderate roughness levels,  $\eta = 0.5$  in the complex  $\alpha$  plane at  $Re = 195$ , where an exchange of modes has occurred. These branches arise from crossflow and streamline-curvature instability modes and are different to the branches 1 & 2 discussed in §4.3.1. The region of convective instability is indicated by a branch crossing into the region lying below the  $\alpha_i = 0$  line and is now determined by the modified branch 1 which has two minima. The peak in between

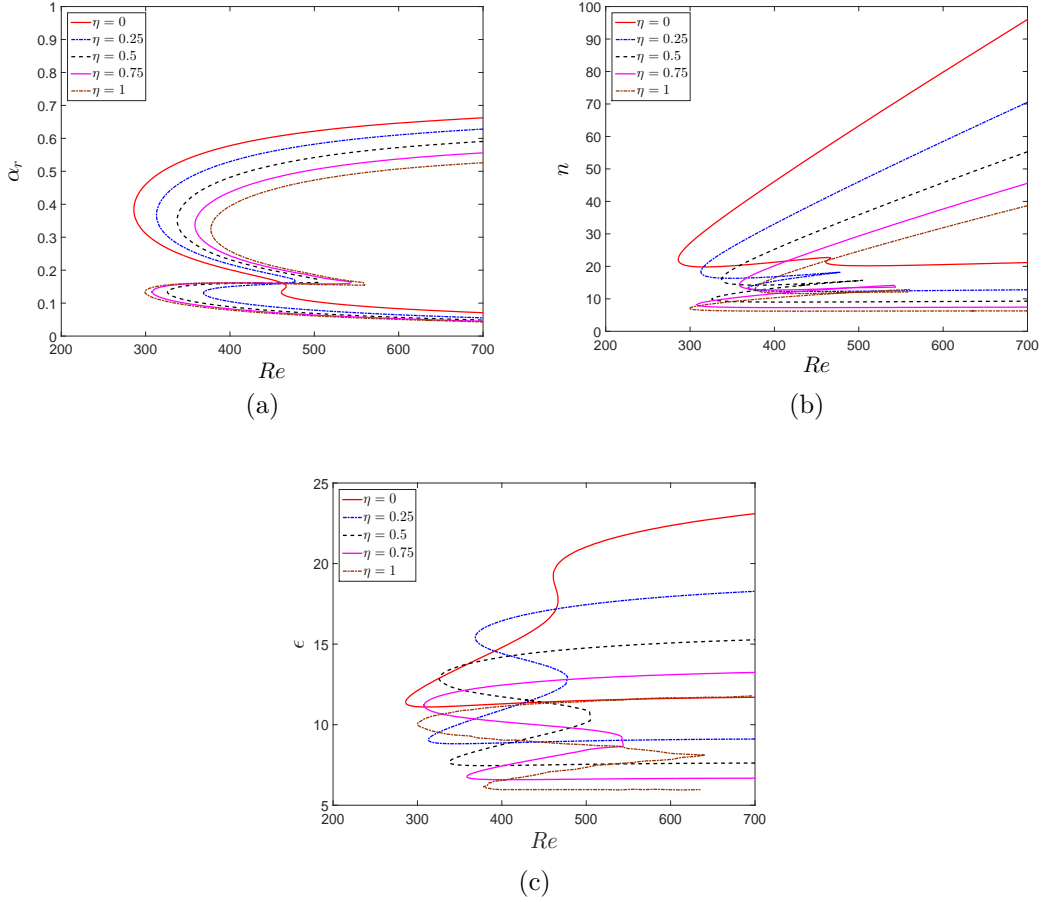


Figure 5.8: Neutral curves of the convective instability of the von Kármán flow in the case of radially-anisotropic roughness (concentric grooves,  $\lambda = 0$ ).

these minima moves downwards and branch points crossing the line  $\alpha_i = 0$  move apart as  $Re$  is increased. Therefore, the region of instability expands and a two lobed structure of the neutral curve maps out. For a sufficiently high value of  $Re$  the peak moves below the line  $\alpha_i = 0$  and further increases in  $Re$  to produce the upper and lower branches of the neutral curve. This spatial branch behaviour is typical for each flow in the BEK system in the case of anisotropic surface roughness with concentric grooves. Moreover, in each neutral curve, the Type I mode appears as an upper lobe that is characterised by higher wave numbers whereas the Type II mode appears as a lower lobe that is characterised by smaller wave numbers.

The solutions of the perturbation equations (2.40)-(2.41) are obtained using the spectral Chebyshev method discussed in §3.2.1. Figure 5.8 presents neutral curves of

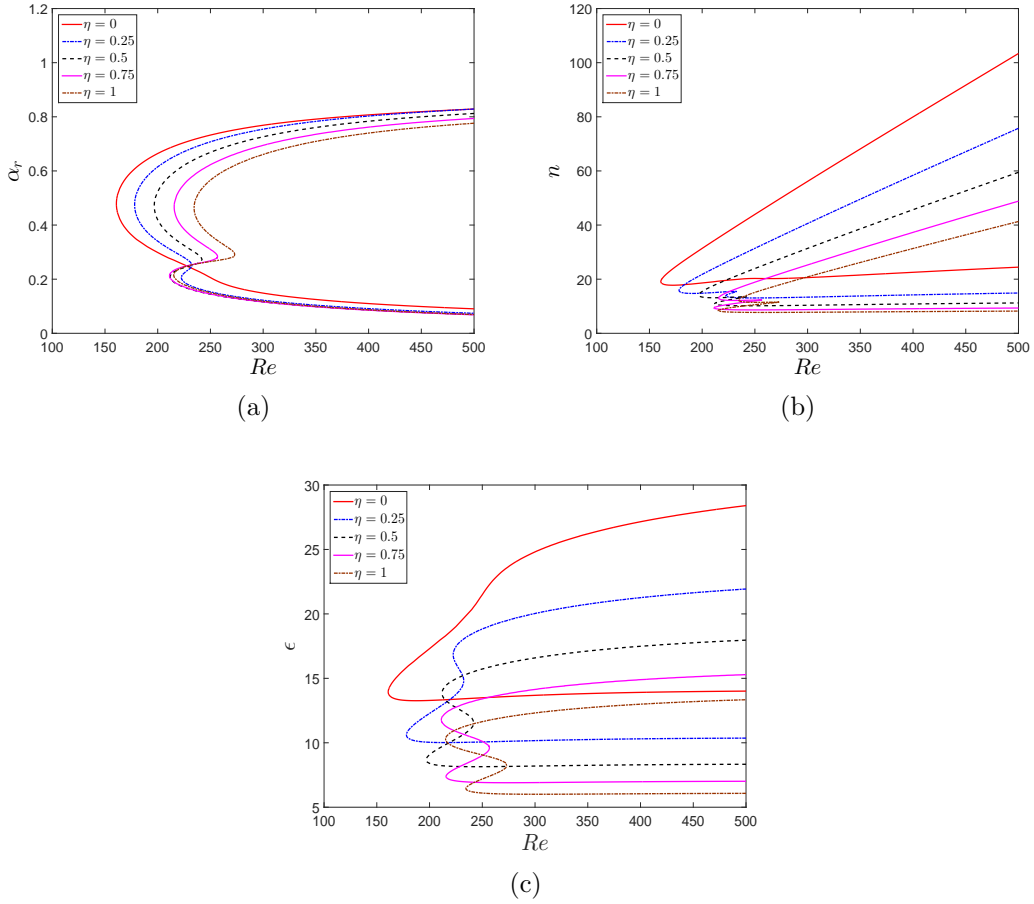


Figure 5.9: Neutral curves of the convective instability for  $Ro = -0.5$  in the case of radially-anisotropic roughness (concentric grooves,  $\lambda = 0$ ).

the von Kármán flow in the case of radially anisotropic roughness. These curves are consistent with those of Cooper *et al.* (2015) and are included here for completeness of the BEK system only, and validation of our code. It is seen from Figure 5.8(a) that increasing the level of roughness has a strong stabilising effect on the Type I mode in terms of the critical Reynolds number and width of the instability region while the Type II mode is destabilised. After a threshold value of the parameter  $\eta = 0.5$ , the Type II mode onsets earlier than the Type I mode and becomes the dominant instability mechanism in the system. Figures 5.8(b)-(c), on the other hand, show a substantial decreasing of the number of vortices  $n$  and the vortex angle  $\epsilon$  along both the upper and lower branches of the neutral curves with increased roughness; this is in parallel with the strong stabilising effect on the Type I mode.

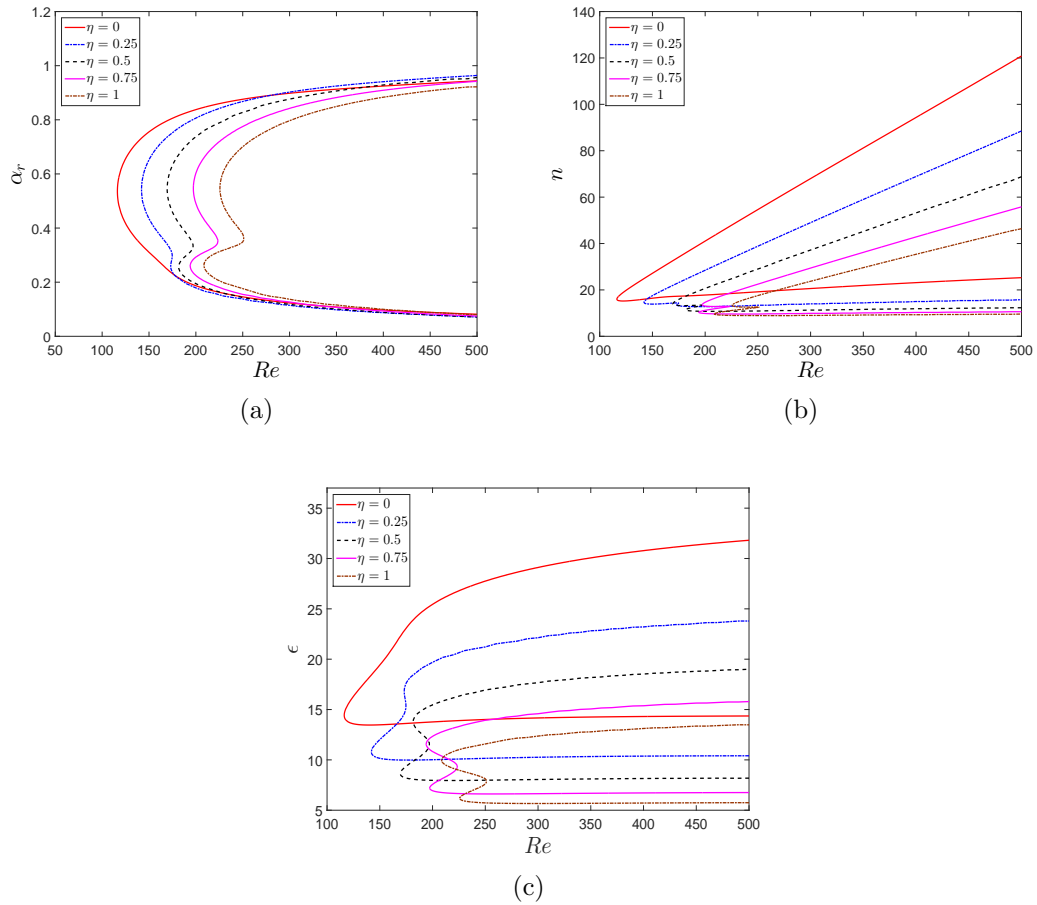


Figure 5.10: Neutral curves of the convective instability of the Ekman flow in the case of radially-anisotropic roughness (concentric grooves,  $\lambda = 0$ ).

Neutral curves of the related flow,  $Ro = -0.5$ , are presented in Figure 5.9. Figure 5.9(a) reveals the strong stabilisation effect of increased concentric grooves on the Type I mode of instability in terms of the critical Reynolds number, the width of the instability region and the destabilising effect on the Type II mode. Compared to the von Kármán flow, both the Type I and Type II instabilities onset at lower Reynolds numbers for each roughness level. Furthermore, it is clear from Figures 5.9(b)-(c) that the number of vortices and values of the vortex angle decrease along both the upper and lower branches of the neutral curves for increased roughness, as they did in the von Kármán case.

The neutral curves of the Ekman flow,  $Ro = 0$ , are presented in Figure 5.10. It is seen from Figure 5.10(a) that concentric grooves have a similar effect on the Type I

mode of the Ekman flow as for the von Kármán and  $Ro = -0.5$  flows. However, the response of the Type II mode to increased levels of roughness is notably different. Indeed, the concentric grooves lead to a stabilising effect on the Type II mode in terms of the critical Reynolds number although they have a destabilising effect on it in terms of the width of unstable region. Nevertheless, the Type II mode becomes the dominant instability mechanism for sufficiently large values of  $\eta$ . It is worth noting that the critical values of the Reynolds number for both modes are smaller than those of the previous cases, the von Kármán and  $Ro = -0.5$  flows, at each particular level of radially anisotropic roughness.

The neutral curves of the Ekman flow in terms of the number of spiral vortices are represented in Figure 5.10(b). We can see a significant decrease in the number of vortices along the upper branch of the neutral curve and a slight decrease along the lower branch. Similarly, Figure 5.10(c) shows that the value of the vortex angle decreases in a similar way to  $n$  along both branches for larger values of the roughness parameter  $\eta$ .

The neutral curves of the related flow for  $Ro = 0.5$  are presented in Figure 5.11. Figure 5.11(a) reveals that the strong stabilising effect of increased concentric grooves on both the modes in terms of critical Reynolds number is maintained. The width of the instability region of the Type II mode still expands whereas that for the Type I mode shrinks. The decrease of the number of vortices  $n$  and the vortex angle  $\epsilon$  have a similar pattern for the von Kármán and Ekman flows, as evidenced in Figures 5.11(c)-(e). In other words, these values decrease significantly along the upper branch and decrease slightly along the lower branches for increased roughness.

The neutral curves of the Bödewadt flow are presented in Figure 5.12. In contrast to the case of radial grooves, the effects of concentric grooves on the Bödewadt flow are quite similar to those of the other flows in the system. However, the onset of the Type II mode is further delayed until the roughness parameter  $\eta$  is varied up to 0.5, as observed in Figure 5.12(a). It is also worth noting that the width of the unstable region shrinks with increased roughness only up until a certain value of  $Re$

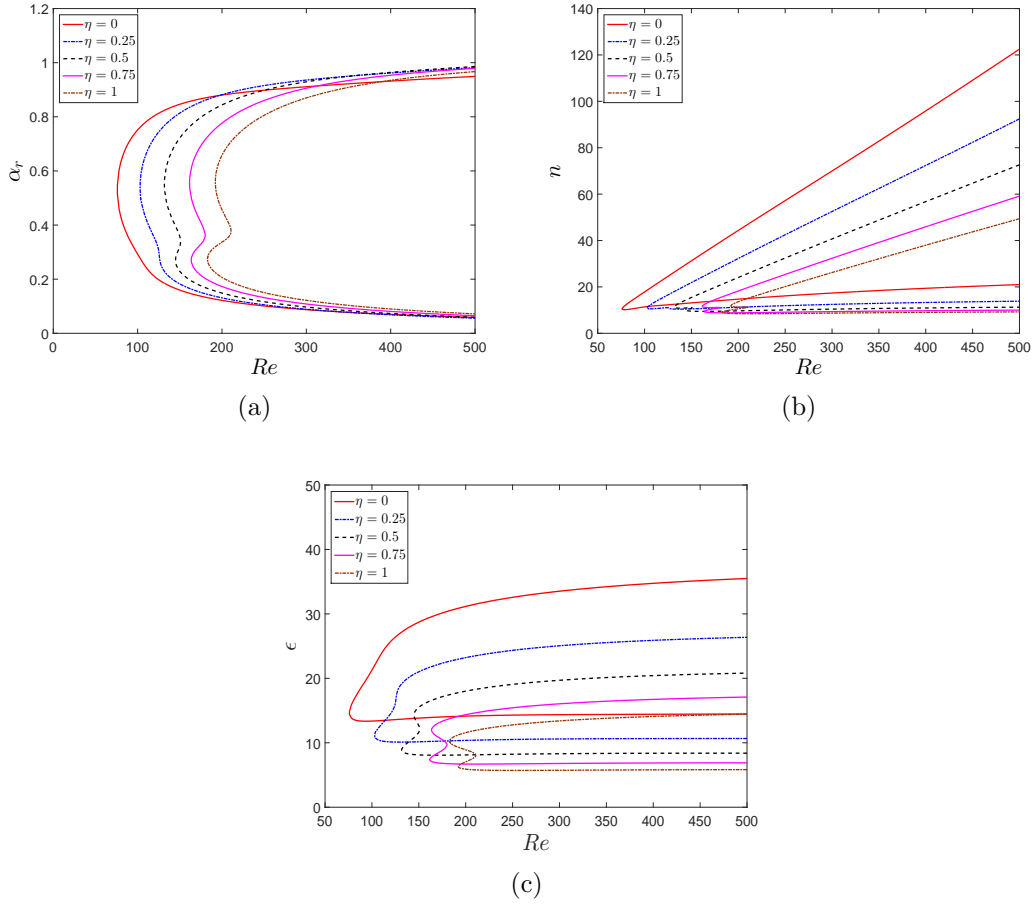


Figure 5.11: Neutral curves of the convective instability for  $Ro = 0.5$  in the case of radially-anisotropic roughness (concentric grooves,  $\lambda = 0$ ).

is reached. After this threshold, it begins to expand along the upper branch. There is a substantial decrease in the number of vortices along the upper branch and a slight decrease along the lower branch as the roughness is increased, as is evidenced in Figure 5.12(b). It is also clear from Figure 5.12(c) that an increase in roughness level reduces the value of the vortex angle along both branches of the neutral curves.

It is also worthwhile to present the comparison of the stability characteristic of all flows in the BEK system for a moderate level of roughness parameter,  $\eta = 0.5$ . Figure 5.13(a) demonstrates that the strength of the stabilising effect on both the Type I and Type II modes in terms of the critical Reynolds number reduces continuously from the von Kármán flow,  $Ro = -1$ , to the Bödewadt flow,  $Ro = 1$ . Moreover, the instability area of the modes expands with increased surface rough-

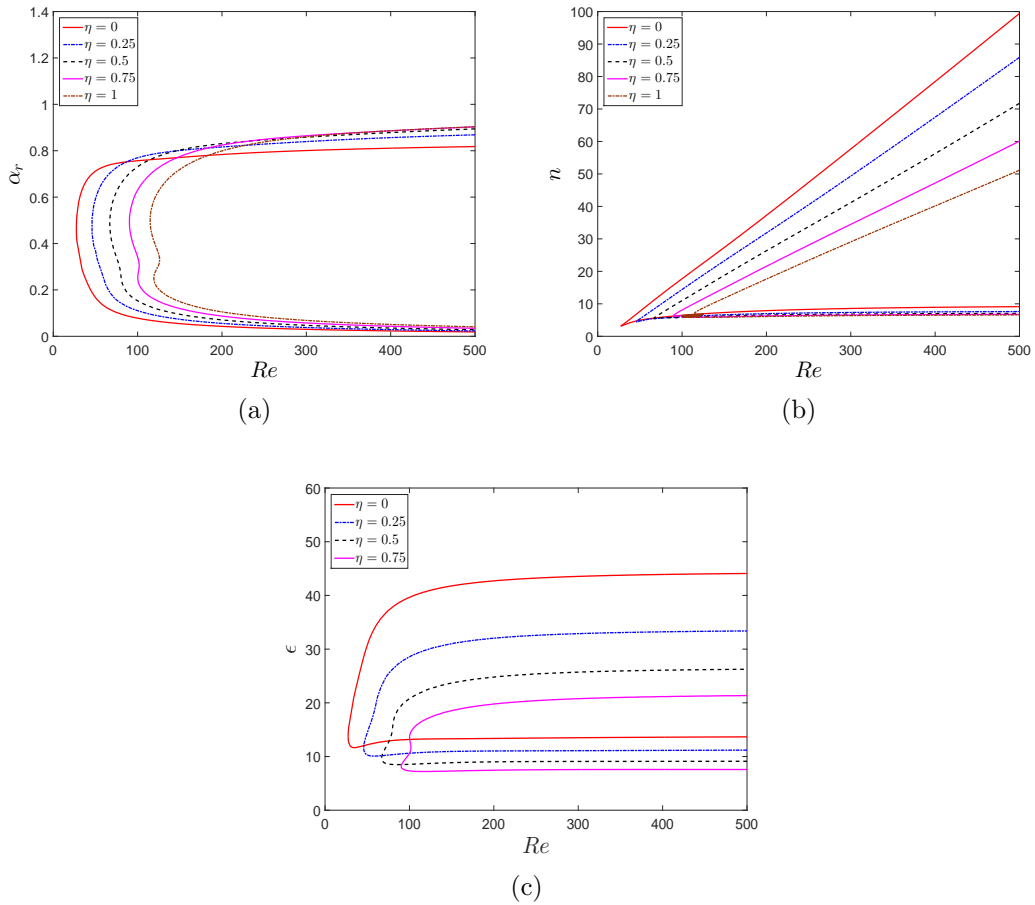


Figure 5.12: Neutral curves of the convective instability of the Bödewadt flow in the case of radially-anisotropic roughness (concentric grooves,  $\lambda = 0$ ).

ness. The behaviour of these flows on a radially anisotropic rough disk are similar to those obtained in the smooth disk case (Lingwood, 1997). Similarly, we also obtain the two lobed structure of the neutral curves for all Rossby number flows in this case although the appearance of the Type II mode is reduced towards the Bödewadt flow.

Figure 5.13(b) shows that the number of vortices  $n$  is slightly affected by increased roughness level for the negative Rossby number flows around the onset of the Type I mode, whereas it decreases for positive Rossby number flows. The number of vortices around the onset of the Type II mode, along the lower branch of the neutral curves in Figure 5.13(c), is nearly unchanged for all the flows. The vortex angle at the critical Reynolds numbers of both the modes increases continuously as

The von Kármán layer,  $Ro = -1$ 

Parameter	$Re$	$n$	$\epsilon$
$\eta = 0$	<b>286.05</b> (460.92)	<b>22.20</b> (21.28)	<b>11.40</b> (19.28)
$\eta = 0.25$	<b>312.91</b> (368.56)	<b>18.35</b> (13.27)	<b>9.06</b> (15.42)
$\eta = 0.5$	337.42 ( <b>325.80</b> )	<b>16.02</b> (9.94)	(7.66)( <b>12.87</b> )
$\eta = 0.75$	358.48 ( <b>307.79</b> )	<b>14.40</b> (8.16)	(6.77)( <b>11.22</b> )
$\eta = 1$	377.36 ( <b>299.24</b> )	<b>13.16</b> (7.05)	(6.11)( <b>10.00</b> )

The related layer for  $Ro = -0.5$ 

Parameter	$Re$	$n$	$\epsilon$
$\eta = 0$	<b>160.81</b> (-)	<b>19.09</b> (-)	<b>13.97</b> (-)
$\eta = 0.25$	<b>178.10</b> (222.43)	<b>15.86</b> (13.84)	<b>10.61</b> (16.83)
$\eta = 0.5$	<b>196.75</b> (211.82)	<b>14.13</b> (10.91)	<b>8.68</b> (13.85)
$\eta = 0.75$	215.62 ( <b>211.17</b> )	13.05 ( <b>9.36</b> )	7.38 ( <b>11.79</b> )
$\eta = 1$	234.52 ( <b>215.21</b> )	12.29 ( <b>8.40</b> )	6.44 ( <b>10.29</b> )

The Ekman layer,  $Ro = 0$ 

Parameter	$Re$	$n$	$\epsilon$
$\eta = 0$	116.26 (-)	16.04 (-)	14.33 (-)
$\eta = 0.25$	<b>142.04</b> (173.17)	<b>14.68</b> (13.52)	<b>10.31</b> (16.61)
$\eta = 0.5$	<b>169.35</b> (181.65)	<b>14.02</b> (11.44)	<b>8.60</b> (14.89)
$\eta = 0.75$	197.33 ( <b>194.01</b> )	13.63 ( <b>10.34</b> )	7.45 ( <b>11.46</b> )
$\eta = 1$	225.67 ( <b>208.65</b> )	13.38 ( <b>9.64</b> )	5.73 ( <b>9.74</b> )

The related layer for  $Ro = 0.5$ 

Parameter	$Re$	$n$	$\epsilon$
$\eta = 0$	<b>75.89</b> (-)	<b>10.52</b> (-)	<b>14.63</b> (-)
$\eta = 0.25$	<b>102.95</b> (-)	<b>10.98</b> (-)	<b>11.12</b> (-)
$\eta = 0.5$	<b>131.72</b> (144.99)	<b>11.35</b> (9.96)	<b>8.88</b> (14.29)
$\eta = 0.75$	<b>161.58</b> (163.57)	<b>11.64</b> (9.40)	<b>7.37</b> (11.98)
$\eta = 1$	192.15 ( <b>182.86</b> )	11.86 ( <b>9.05</b> )	6.30 ( <b>10.24</b> )

The Bödewadt layer,  $Ro = 1$ 

Parameter	$Re$	$n$	$\epsilon$
$\eta = 0$	<b>27.38</b> (-)	<b>3.12</b> (-)	<b>14.32</b> (-)
$\eta = 0.25$	<b>45.97</b> (-)	<b>4.43</b> (-)	<b>12.03</b> (-)
$\eta = 0.5$	<b>67.00</b> (-)	<b>5.55</b> (-)	<b>8.60</b> (-)
$\eta = 0.75$	<b>90.25</b> (100.70)	<b>6.41</b> (6.23)	<b>8.59</b> (12.61)
$\eta = 1$	<b>114.85</b> (119.21)	<b>7.07</b> (6.20)	<b>6.88</b> (11.46)

Table 5.2: Critical values of observable parameters at the onset of convective instability of both modes for the boundary layers in the BEK system in the case of radially-anisotropic roughness (concentric grooves). Type I and (Type II). The most dangerous mode is indicated as bold text in terms of critical Reynolds number.

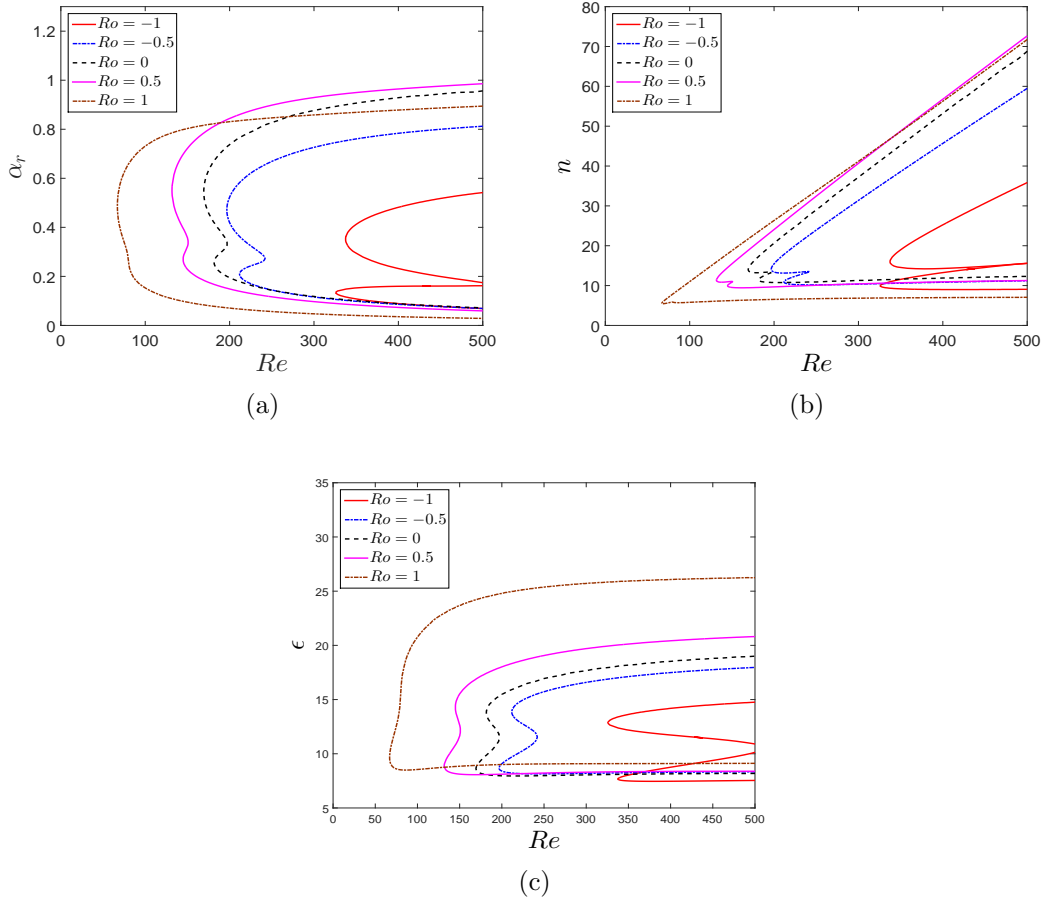


Figure 5.13: Neutral curves of the convective instability of the particular flows in the BEK system in the case of a moderate value of radially-anisotropic roughness,  $\eta = 0.5$ .

the Rossby number increases from the von Kármán flow,  $Ro = -1$ , to the Bödewadt one,  $Ro = 1$  as shown in Figure 5.13(c). However, the increment of the vortex angle along the lower branches is less than that along the upper branches.

The numerical predictions of the critical parameters at the onset of convective instability are presented in Table 5.2 for each flow discussed previously. The critical values of the Type I mode of the smooth case are in very close agreement with the existing results in the literature for the BEK system and those due to Cooper *et al.* (2015) for the rough rotating disk, however there are some minor discrepancies in the Type II mode results. These discrepancies are consistent with the apparent sensitivity of Type II mode results in the von Kármán flow due to the solution methods

used as stated in the study of Balakumar & Malik (1990); this is also discussed by Garrett *et al.* (2016). The effects of anisotropic roughness with concentric grooves on the Type I mode of the neutral curves of the BEK system of flows are similar to the effects of increased suction in all flows of the system and increased uniform distribution of magnetic field in the von Kármán flow. The effects on the Type II mode are different than those of these methods. The Type II mode has been spatially damped by increased concentric grooves whereas increased suction invokes this mode. An increased uniform magnetic field, on the other hand, delays the onset of Type II mode but it is not suppressed spatially.

### 5.3.2. The growth rates

We now consider the effect of concentric grooves on the growth rates of the instability modes of the BEK system of boundary layer flows. However, as discussed in §4.3.2 it is not possible to produce plots of the convective growth rates of the Bödewadt flow due to the early onset of the “branch exchange” (Lingwood & Garrett, 2011).

The growth rates of the Type I and Type II instability modes within the BEK system of flows at  $Re = Re_{critical} + 25$  are presented in Figure 5.14 as a function of the vortex number  $n$  for each level of roughness. Here  $Re_{critical}$  is the critical Reynolds number presented in Table 5.2 for the onset of the convective instability of the Type I mode. It is easy to identify the stabilizing effect of concentric grooves on the Type I mode of each flow from Figures 5.14(a)-(d). That is, the value of the most rapidly growing Type I mode indicated by a red dot decreases with an increase in the roughness size. These figures also present the destabilization of the Type II mode of each flow with increased roughness parameter  $\eta$ . In other words, the value of the most rapidly growing Type II mode indicated by a red circle increases proportionally to the surface roughness. Moreover, the maximum growth rate shifts to lower values of  $n$  for both the modes, indicating a decrease in the number of vortices along upper and lower branches as an effect of increased surface roughness level. The change of the number of vortices is in contrast to the observations detailed for the azimuthally

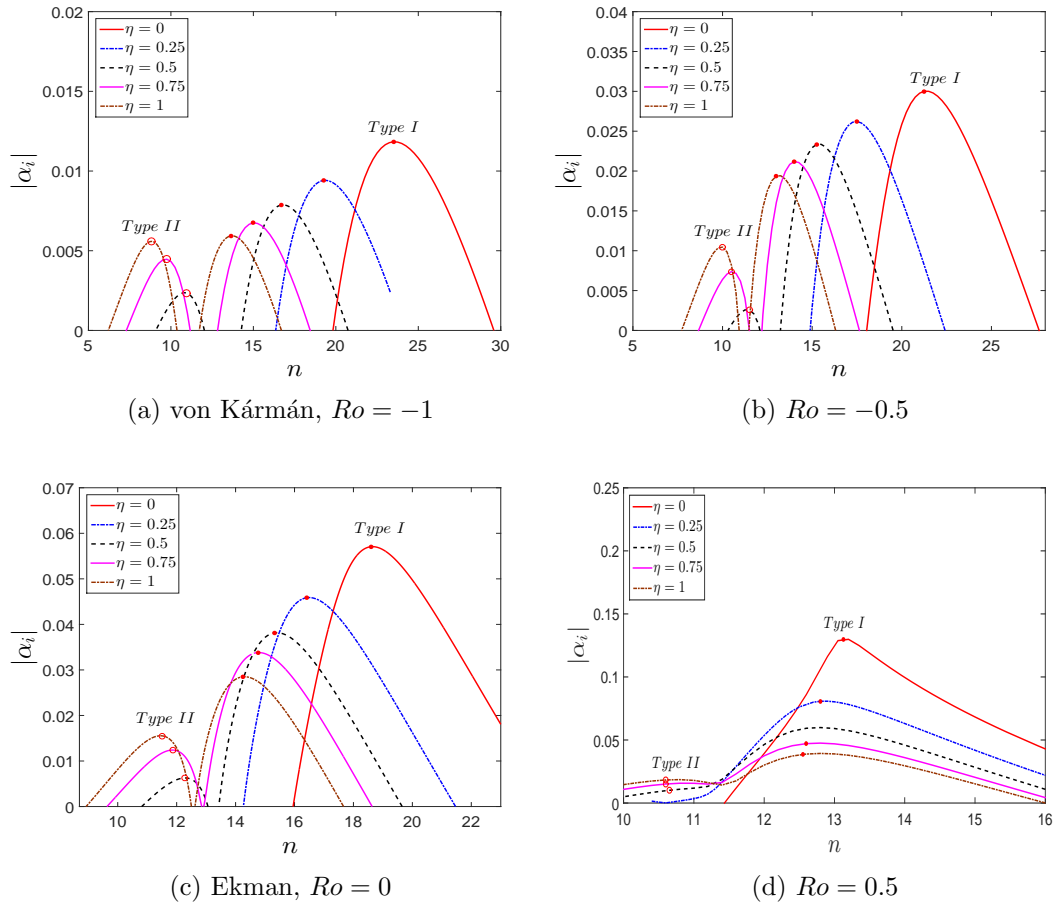


Figure 5.14: Growth rates of Type I and Type II instability modes within the BEK boundary layer flows as a function of vortex number  $n$  at  $Re = Re_{critical} + 25$  in the case of radial grooves, azimuthally-anisotropic roughness. The red dots and circles indicate the most rapidly growing mode for Type I and Type II modes, respectively.

anisotropic roughness cases in §4.3.2.

These results are consistent with the response of the critical parameters obtained for each flow as stated in Table 5.2. A similar discussion of the growth rates for the von Kármán flow has been provided by Cooper *et al.* (2015) and we include our results for this flow as a validation.

## 5.4. Energy Analysis

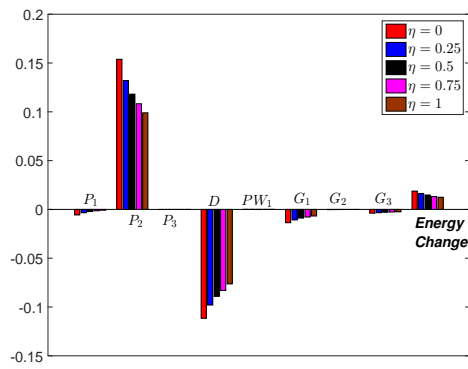
The aim of this section is to establish the underlying physical mechanisms behind the effects of concentrically grooved disks on the BEK system of boundary layer flows

by solving the energy balance equation (2.50). As discussed in §4.4, this equation can be solved for any eigenmode of the perturbation equations (2.40)-(2.41).

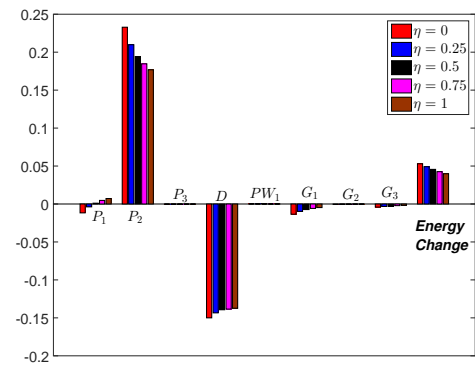
The positive terms that arise from the solutions of (2.49) contribute to the energy production and the negative ones reduce the energy of the system. A destabilisation of any eigenmode occurs if energy production exceeds the energy dissipation in the system. Therefore we can identify the effect of concentric grooves on the instability modes by calculating the energy change of the system, that is the sum of energy production and dissipation in the system.

The results obtained in this section for the BEK system of boundary layer flows are calculated at the location of the maximum growth rates of the Type I and Type II modes, as presented in previous section. The only exception is the Bödewadt flow due to the “branch exchange” issue identified by Lingwood & Garrett (2011). The energy balance of the Bödewadt flow is calculated at fixed  $Re = 400$  with the number of vortices,  $n = 30$ , and  $n = 12$ , for the Type I, and Type II modes, respectively. The values of number of vortices are chosen for the purpose of being outside of the absolutely unstable region at  $Re = 400$ .

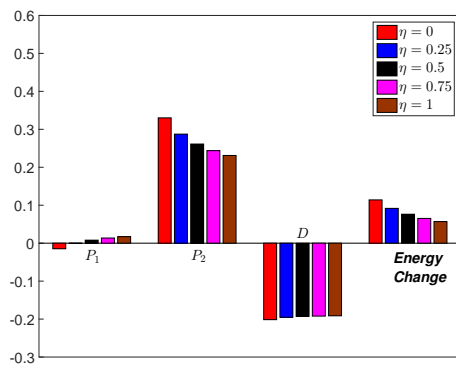
Figure 5.15 shows the energy balance calculations of the Type I mode in the case of concentric grooves. The stabilisation effect, that is the reduction in the energy of the system as roughness is increased, is seen clearly from the Figure 5.15 for all Rossby numbers. This effect arises mainly from the reduction in the energy production term  $P_2$  and in the energy dissipation term  $D$  for each flow, with the exception of the Bödewadt flow. In the case of the Bödewadt flow, the main energy production terms are  $G_1$  and  $G_3$ , that arise from the streamline curvature effects and the three dimensionality of the mean flow. Indeed, the energy removal effects of these terms for the negative Rossby number flows turns into an energy dissipation for the positive Rossby number flows. However, a decreasing of the  $G_1$  and  $G_3$  terms and a substantial increasing of the viscous dissipation for increased roughness leads to a stabilisation of the Type I mode in the Bödewadt flow. It is also worthwhile to note that the reduction in all terms decrease as the Rossby number change from negative unity to positive unity.



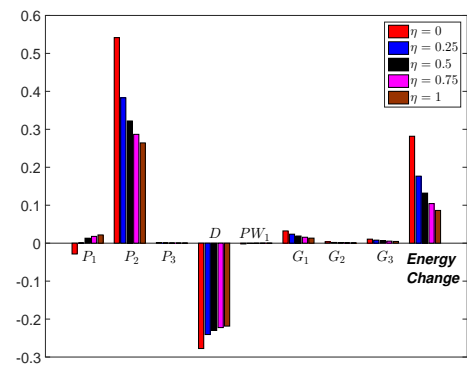
(a) von Kármán,  $Ro = -1$



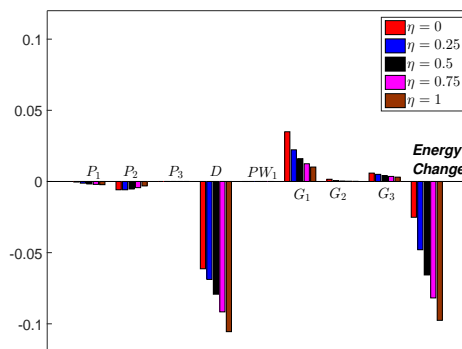
(b)  $Ro = -0.5$



(c) Ekman,  $Ro = 0$

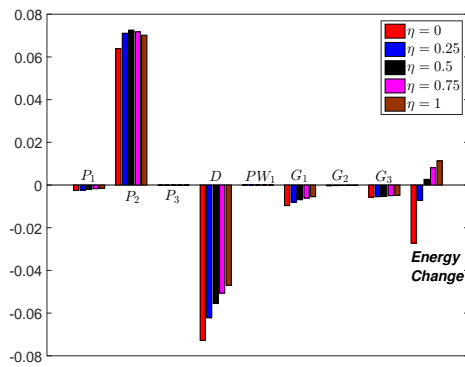


(d)  $Ro = 0.5$

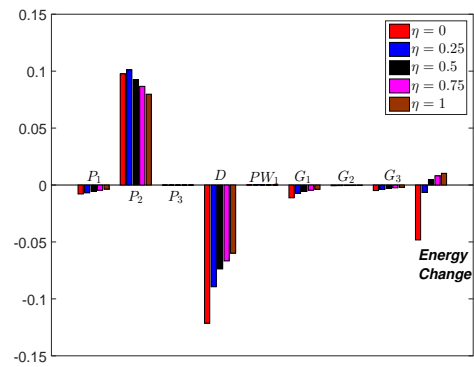


(e) Bödewadt,  $Ro = 1$

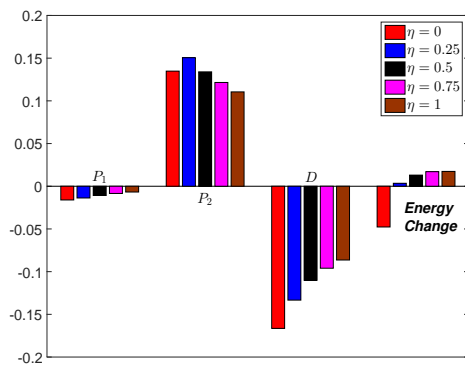
Figure 5.15: Energy balance of the Type I mode of the BEK system of boundary layer flows for radially anisotropic roughness at the location of maximum amplification at  $Re = Re_{critical} + 25$  except the Bödewadt flow. For Bödewadt flow,  $Re = 400$  and  $n = 30$ . The terms are normalised by the mechanical energy flux of the most dangerous mode within each figure.



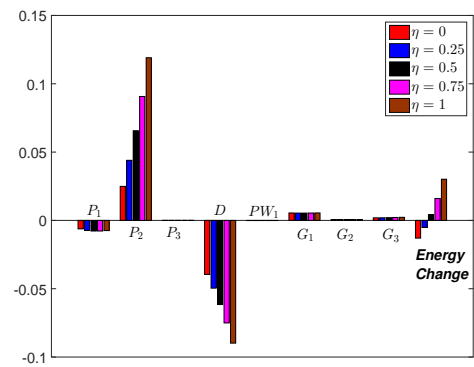
(a) von Kármán,  $Ro = -1$



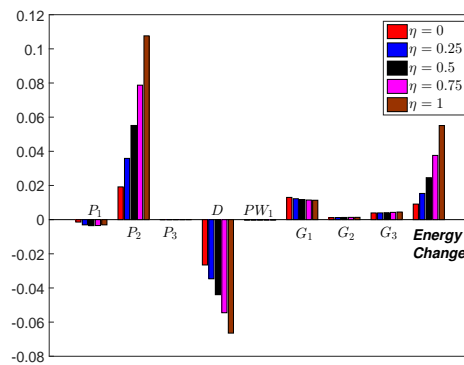
(b)  $Ro = -0.5$



(c) Ekman,  $Ro = 0$



(d)  $Ro = 0.5$



(e) Bödewadt,  $Ro = 1$

Figure 5.16: Energy balance of the Type II mode of the BEK system of boundary layer flows for radially anisotropic roughness at the location of maximum amplification at  $Re = Re_{critical} + 25$ , except the Bödewadt flow. For this flow,  $Re = 400$  and  $n = 12$ . The terms are normalised by the mechanical energy flux of the most dangerous mode within each figure.

The energy balance calculations of the Type II mode are presented in Figure 5.16 for the case of concentric grooves. Clearly, destabilisation of the Type II modes of each flow is due to an increase in the energy change for higher values of the roughness parameter. The main cause of destabilisation is seen to be the strong reduction of energy dissipation from each negative Rossby number flow, including the Ekman flow as is evidenced in Figure 5.16(a)-(c). In contrast, destabilisation of the positive Rossby number flows is due to a substantial increase of the energy production term  $P_2$  with increased roughness as is evidenced in Figure 5.16(d)-(e). Moreover, the geometric terms  $G_i$  for the Type II mode are relatively larger than those of the Type I mode.

Forms of the azimuthal velocity perturbation,  $\hat{v}$ , and the axial velocity perturbation,  $\hat{w}$ , which provide some explanations about the energy trends of the BEK system flows (Cooper *et al.*, 2015) are presented in Figure 5.17 for the Type I mode. It is seen from this figure that the general form of both disturbance profiles are not changed with the profiles being translated away from the wall as the roughness increased. The strong decrease of the  $P_2$  term in the case of the flows with negative Rossby numbers is due to a reduction in the amplitude of the axial velocity perturbation,  $\hat{w}$ . For the  $Ro = 0$  and  $Ro = 0.5$  flows, the decrease of that term results from the strong reduction in the amplitude of the axial disturbance profile  $\hat{w}$  as the roughness increases. The substantial increase of viscous dissipation in the Bödewadt flow is seen to be caused by an increase of the amplitudes of both velocity profiles as is evidenced in 5.17(i)-(j).

Figure 5.18 presents the form of the velocity profiles for the Type II mode. It is clearly seen that it is the decreasing viscous dissipation that leads to destabilisation of Type II modes of the BEK system flows, except the Bödewadt flow. The decreasing of the dissipation term is caused by a reduce in the amplitude of the  $\hat{v}$  profile with increased roughness. However, the increasing energy production in the Bödewadt flow is caused by a substantial increase in the amplitude of the  $\hat{w}$  profile as the roughness level is increased, as is evidenced in 5.18(i)-(j). On the other hand, the  $\hat{v}$  disturbance profile for the Type II mode extends further into the boundary

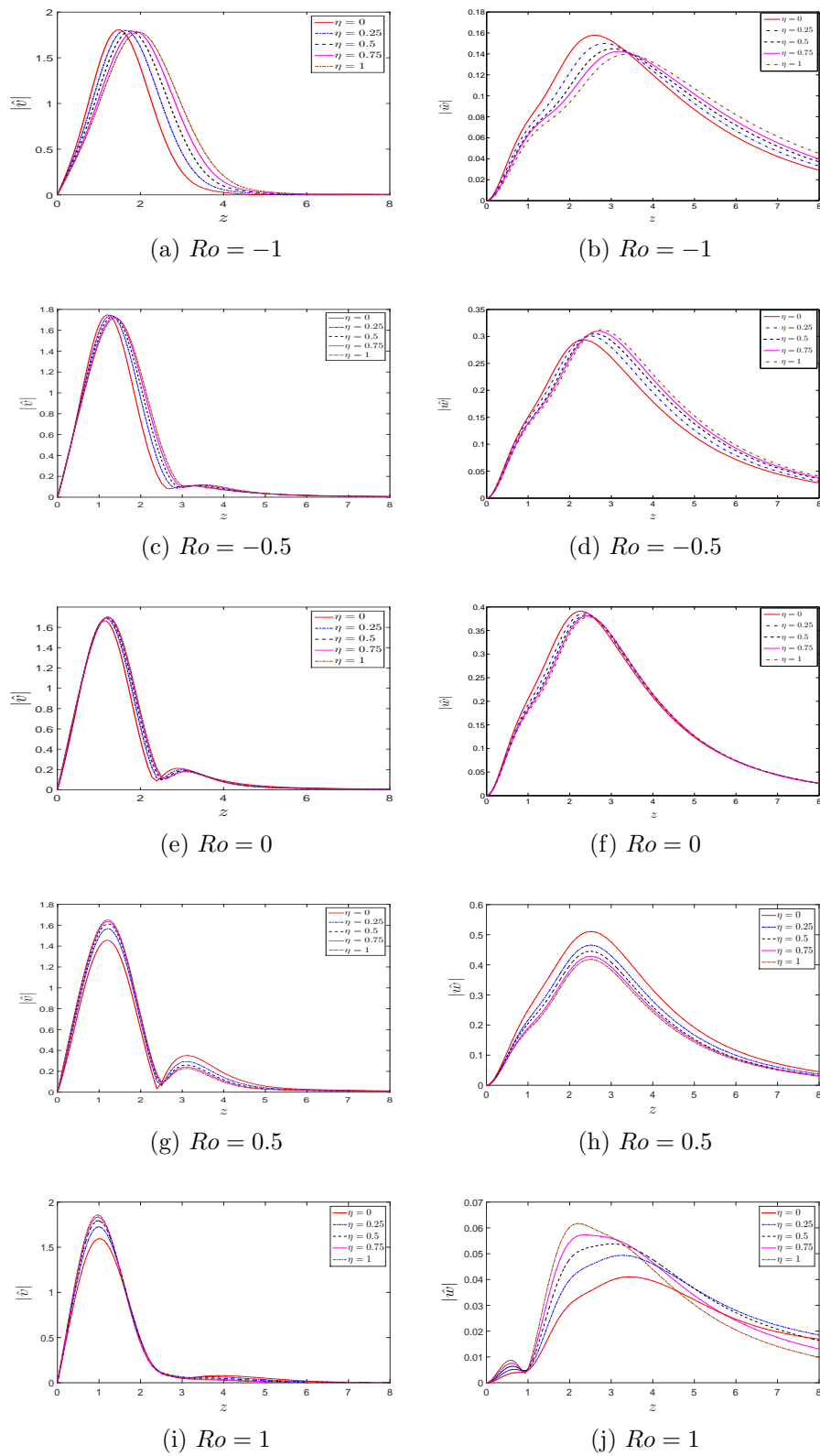


Figure 5.17: Type I mode profiles for the azimuthal and the axial disturbance velocity profiles of the BEK flows in the case of a concentrically grooved disk at the location of maximum amplification at  $Re = Re_{critical} + 25$  except the Bödewadt flow. For Bödewadt flow,  $Re = 400$  and  $n = 30$ .

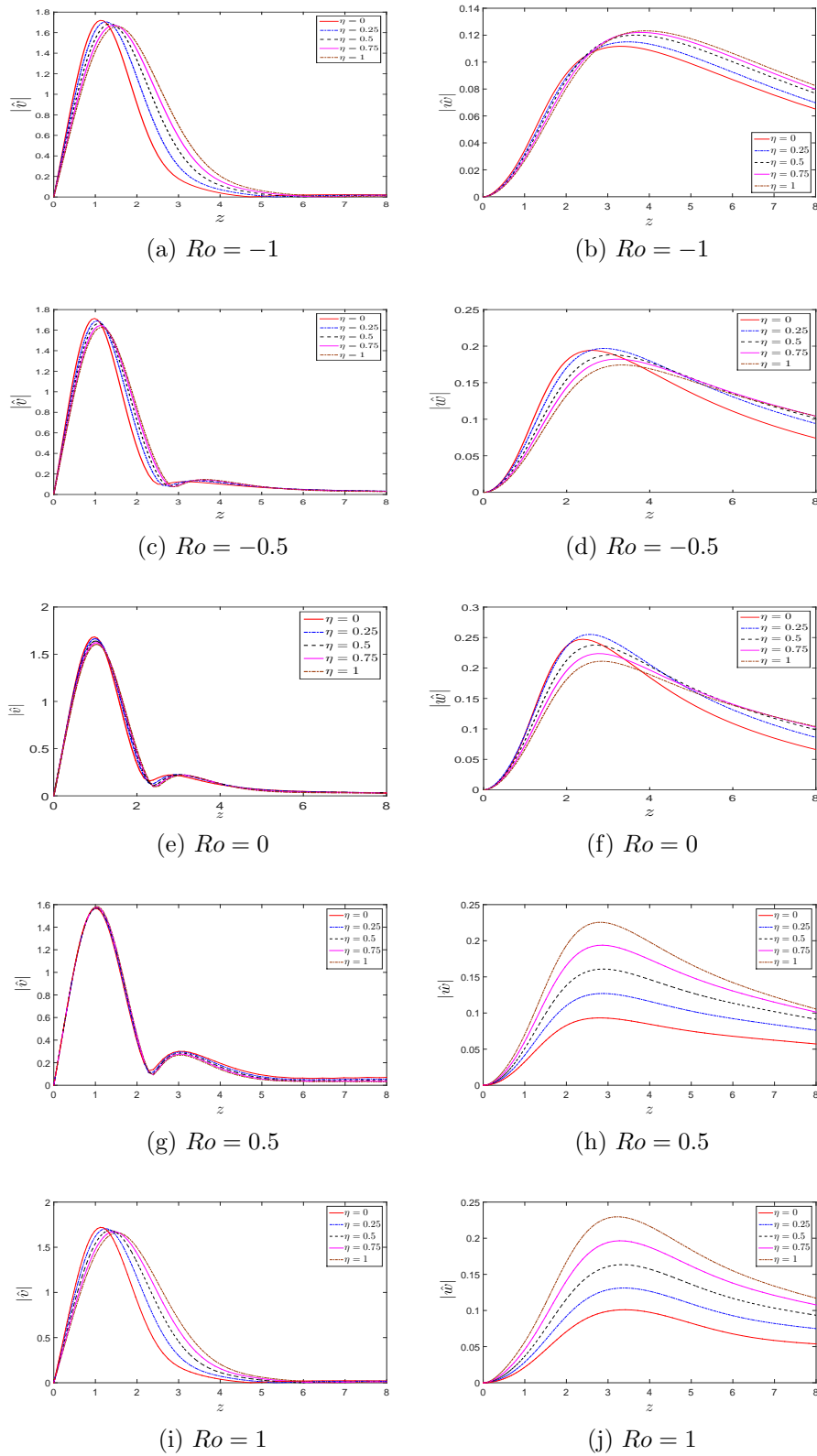


Figure 5.18: Type II mode profiles for the azimuthal and the axial disturbance velocity profiles of the BEK flows in the case of a concentrically grooved disk at the location of maximum amplification at  $Re = Re_{critical} + 25$  except the Bödewadt flow. For Bödewadt flow,  $Re = 400$  and  $n = 12$ .

	Ekman flow, $Ro = 0$	Bödewadt flow, $Ro = 1$
$\eta = 0$	219 ~ 220	27 ~ 28
$\eta = 0.25$	346 ~ 347	47 ~ 48
$\eta = 0.5$	563 ~ 564	78 ~ 79
$\eta = 0.75$	> 1000	118 ~ 119
$\eta = 1$	> 1000	174 ~ 175

Table 5.3: Critical Reynolds number for the stationary Type I mode interacting with the absolute instability region inside the neutral curves of the BEK system flows in the case of concentric grooves.

layer and stretches out as roughness is increased and this could be a cause of the destabilisation of the Type II mode.

## 5.5. Absolute instability

We are not able to produce growth rate curves of instability modes for the Bödewadt flow in §5.3.2 due to the “branch exchange” issue. The issue occurs when the Type III mode, as identified by Mack (1985), coalesces with Type I cross-flow instability mode and leads to absolute instability (Lingwood, 1997). Therefore, in this section we investigate the effect of anisotropic roughness with concentric grooves on suppressing one of the coalescing modes. If it is satisfied, it can be a sign that the onset of absolute instability could be delayed to higher Reynolds numbers.

The critical Reynolds numbers of the Ekman and Bödewadt flows at which the “branch exchange” has occurred between the Type I and Type III modes in the case of concentric grooves are shown in Table 5.3. We can see that the “branch exchange” is delayed to a higher Reynolds number for both flows compared to the smooth cases. However, the delay is not as strong as the one obtained in the case of radial grooves. On the other hand, obtaining the delay for the Bödewadt flow is worth being noted as there is no such delay for this flow in the case of radial

grooves. Indeed, these results are in parallel to the stabilisation effect of concentric grooves on the Type I mode and lead the prediction that radially anisotropic surface roughness can be used to delay the onset of absolute instability to higher Reynolds numbers compared to the smooth disk case.

## 5.6. Conclusion

In this chapter we have studied the effects of radially anisotropic roughness on the convective instability of stationary disturbances in the BEK family of boundary layer flows. The presented solutions of the mean flow equations are obtained using the partial-slip approach of Miklavcic & Wang (2004) without modification. The results are in excellent agreement with those in the literature for the smooth surface cases at all values of  $Ro$ . Moreover, the mean flow components of the von Kármán flow are identical to those presented by Cooper *et al.* (2015). Our numerics have revealed that the effects of anisotropic roughness with concentric grooves on the mean flow components are to decrease the amplification of the oscillatory behaviour through the axial direction, along with the magnitude of the radial wall jet. These behaviours are opposite to those found for in the case of anisotropic roughness with radial grooves, as discussed in §4.2.

The local linear stability analyses conducted in §5.3 reveal that radially-anisotropic roughness has a strong stabilising effect on the Type I instability mode in terms of the critical Reynolds number for the onset of the convective instability and the width of instability area for all flows in the BEK system. For the Type II mode a stabilising effect has been observed in terms of the width of the unstable area. Moreover, the relative importance of the Type II mode increases as the roughness level is increased and they are, therefore, expected to dominate for sufficiently high levels.

We also observed that the numbers of vortices,  $n$ , and the vortex angle,  $\epsilon$ , are decreased at all values of  $Ro$  as roughness is increased. The supporting results to the effects of concentric grooves are then obtained by considering the growth

rates of each instability mode and conducting an energy balance analysis for all flows in the BEK system. Furthermore, we have determined the critical Reynolds numbers at the points of which a “branch exchange” has occurred for the Ekman and Bödewadt flows. The increase of those critical Reynolds numbers with increased  $\eta$  could suggest that concentric grooves can be used to delay the onset of absolute instability in rotating disk flows.

The effects of concentric grooves on the Type I mode are similar to effects of other flow-control methodologies for the BEK system: the surface suction technique as studied theoretically by Lingwood & Garrett (2011) and imposing increased uniform magnetic field normal to the disk as studied by Jasmine & Gajjar (2005), whereas those on the Type II mode are in contrast to the effects of these two techniques. Furthermore, we find that the response of the physical mechanisms that lead to transition in the boundary layer is sensitive to the Rossby number of the system as is also shown with the surface suction technique.

# Chapter 6

## Effect of isotropic roughness on the BEK family of boundary layers

### 6.1. Overview

This chapter is concerned with the effects of isotropic roughness on the convective instability mechanisms within the general class of rotating BEK system of boundary-layers. Local linear stability analyses that include both viscous and streamline-curvature effects are conducted. The stability results of each flow are then confirmed with an energy analysis.

For consistency of presentation across the thesis, this chapter follows the structure of Chapters 4 and 5. The effects of isotropic roughness on the solutions of the steady mean flow equations are discussed in §6.2. The results of the convective instability analysis are presented in §6.3 and neutral curves produced from the solutions of the perturbation equations (2.40)-(2.41) are presented in §6.3.1. The convective growth rate curves of each instability mode are presented in §6.4 for increased levels of the roughness. Finally, the absolute instability is discussed briefly in §6.5.

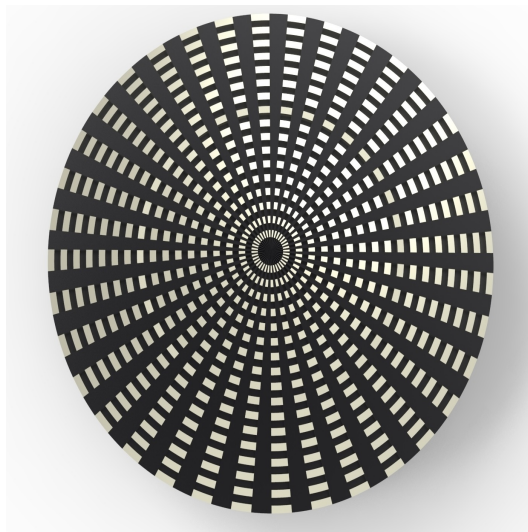


Figure 6.1: Distribution of roughness isotropically over a disk.

## 6.2. The steady mean flow solutions

The primary aim of this section is to study the effects of isotropic roughness on the mean flow profiles of the BEK family of boundary layers. Furthermore, we will compare the results with those of other passive drag control mechanisms on the BEK system of flows; surface suction studied by Lingwood & Garrett (2011) and uniform distribution of a magnetic field studied by Jasmine & Gajjar (2005).

The isotropic surface roughness corresponds to equally distributed roughness in the azimuthal and radial directions on the disk surface. Therefore, we set the roughness parameters in the partial-slip boundary conditions (2.19) obtained under the MW model to  $\eta = \lambda > 0$ . We solve the steady mean flow equations (2.18) of the BEK family of boundary layers with the MATLAB function described in §3.1, however, there are precise analytical solutions of each mean flow components for the Ekman flow stated in (2.20). In the case of the Bödewadt flow, our solutions are identical to those of Sahoo *et al.* (2014) obtained using two distinct methods; a second order finite difference scheme and the Keller box method. Furthermore, the initial values of  $U'(0)$  and  $V'(0)$  are shown in Table 6.1 in the case of isotropic roughness. Note that our initial values for the von Kármán flow are identical to those presented by Miklavcic & Wang (2004).

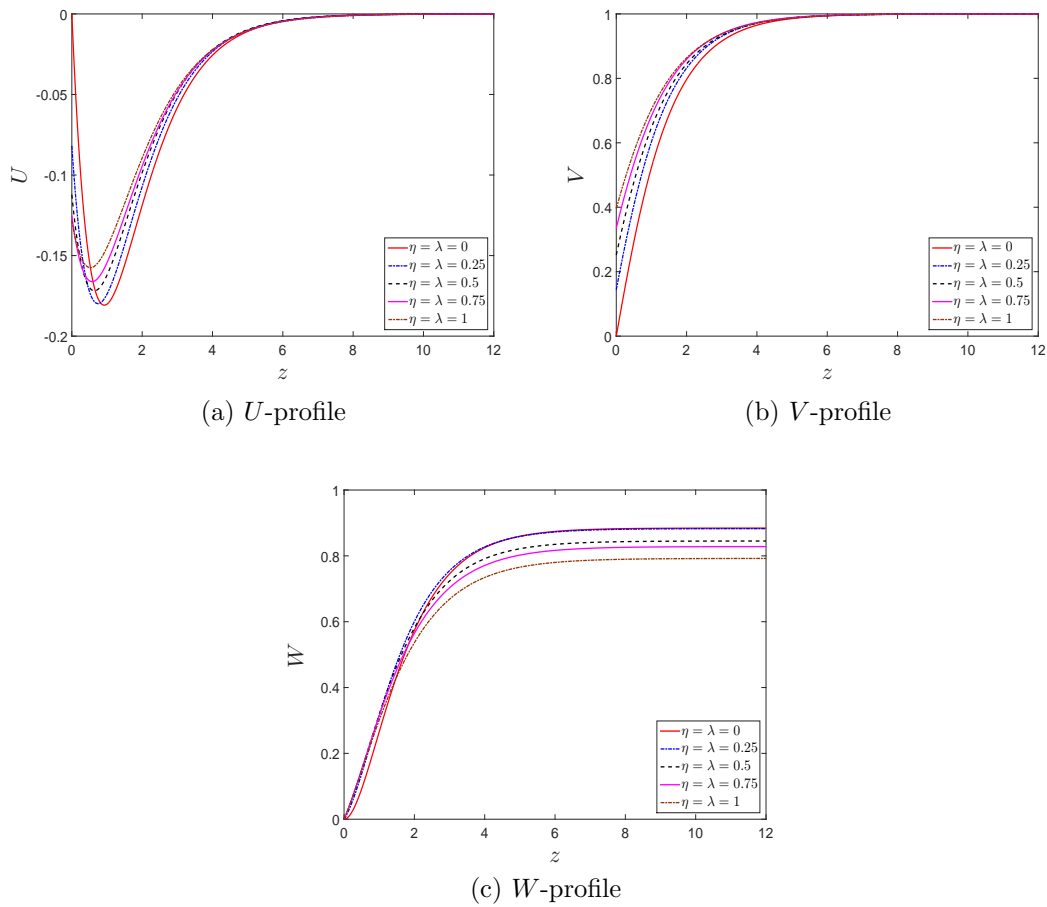


Figure 6.2: Mean-flow components of the von Kármán flow in the case of isotropic roughness ( $\eta = \lambda \neq 0$ ).

The radial mean flow component  $U$  is presented in Figures 6.2(a)-6.6(a) and the azimuthal mean flow profile  $V$  is presented in Figures 6.2(b)-6.6(b). The mean flow component  $W$ , in axial direction, is presented in Figures 6.2(c)-6.6(c).

Figures 6.2-6.6 reveal that the oscillations of each of the mean flow components of the BEK system are damped out with increased isotropic roughness. This effect is similar to that observed in the case of concentric grooves in Chapter 5. It is also similar to the effects of increased surface suction (Lingwood & Garrett, 2011) and an increased the uniform magnetic field applied to the von Kármán flow (Jasmine & Gajjar, 2005). In those studies, convective amplification rates reduce with an increase in their parameters, i.e. they are stabilising.

Figures 6.2(a)-6.6(a) show that the maximum value of the radial velocity com-

The von Kármán layer,  $Ro = -1$

Parameter	$U'(0)$	$V'(0)$
$\eta = \lambda = 0$	-0.510232616	0.615922011
$\eta = \lambda = 0.25$	-0.327600480	0.575119454
$\eta = \lambda = 0.5$	-0.167015414	0.503591898
$\eta = \lambda = 0.75$	-0.277176378	0.446770739
$\eta = \lambda = 1$	-0.128216711	0.395522953

$Ro = -0.5$

Parameter	$U'(0)$	$V'(0)$
$\eta = \lambda = 0$	-0.857041159	0.907317540
$\eta = \lambda = 0.25$	-0.529748347	0.832737971
$\eta = \lambda = 0.5$	-0.353343231	0.722084578
$\eta = \lambda = 0.75$	-0.251546033	0.626364820
$\eta = \lambda = 1$	-0.188042408	0.549310236

$Ro = 0.5$

Parameter	$U'(0)$	$V'(0)$
$\eta = \lambda = 0$	-1.017626469	0.961193351
$\eta = \lambda = 0.25$	-0.657618690	0.908393868
$\eta = \lambda = 0.5$	-0.431523827	0.804078004
$\eta = \lambda = 0.75$	-0.295272439	0.699379912
$\eta = \lambda = 1$	-0.211485030	0.610129728

The Bödewadt layer,  $Ro = 1$

Parameter	$U'(0)$	$V'(0)$
$\eta = \lambda = 0$	-0.941970896	0.772885383
$\eta = \lambda = 0.25$	-0.695524054	0.771562672
$\eta = \lambda = 0.5$	-0.483768497	0.729696382
$\eta = \lambda = 0.75$	-0.335808673	0.659134799
$\eta = \lambda = 1$	-0.240292848	0.586455699

Table 6.1: The initial values of  $U'$  and  $V'$  at the disk surface for various  $Ro$ , calculated by shooting method in case of isotropic roughness ( $\eta = \lambda \neq 0$ ).

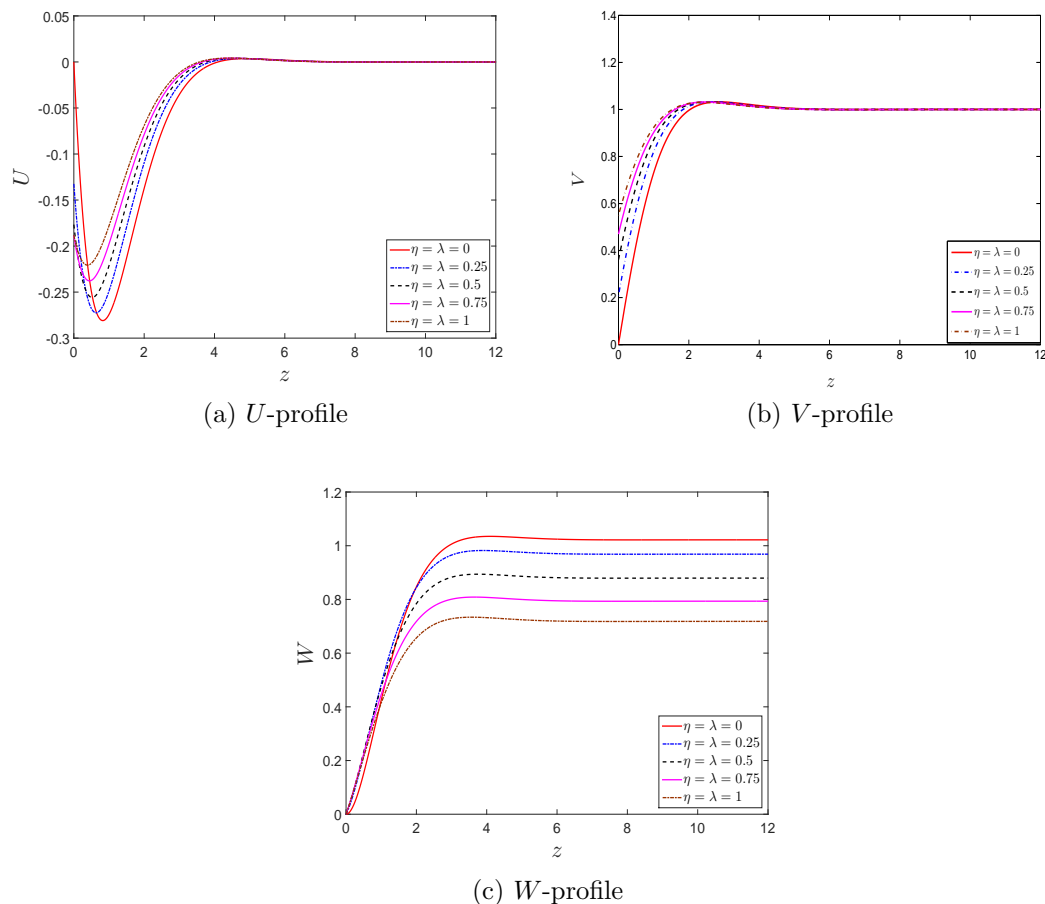


Figure 6.3: Mean-flow components for  $Ro = -0.5$  in the case of isotropic roughness ( $\eta = \lambda \neq 0$ )

ponent,  $U$ , for each flow reduces and moves towards the disk surface as a result of increased isotropic roughness. In other words, increased radial grooves act to decrease the radial wall jet. We also observe that the boundary layer thickness reduces. These changes in the maximum value of the  $U$  profile are similar to those observed with increased surface suction and increased uniform magnetic field. Figures 6.2(c)-6.6(c) show that the amount of fluid entrained into the boundary layer reduces as the magnitude of axial flow reduces substantially for increased isotropic roughness. This is similar to the findings of Lingwood & Garrett (2011) for increased surface suction for  $Ro \geq 0$  and those of Jasmine & Gajjar (2005) for increased uniform magnetic field for the von Kármán flow.

The effects of isotropic roughness on the azimuthal velocity profile  $V$  are pre-

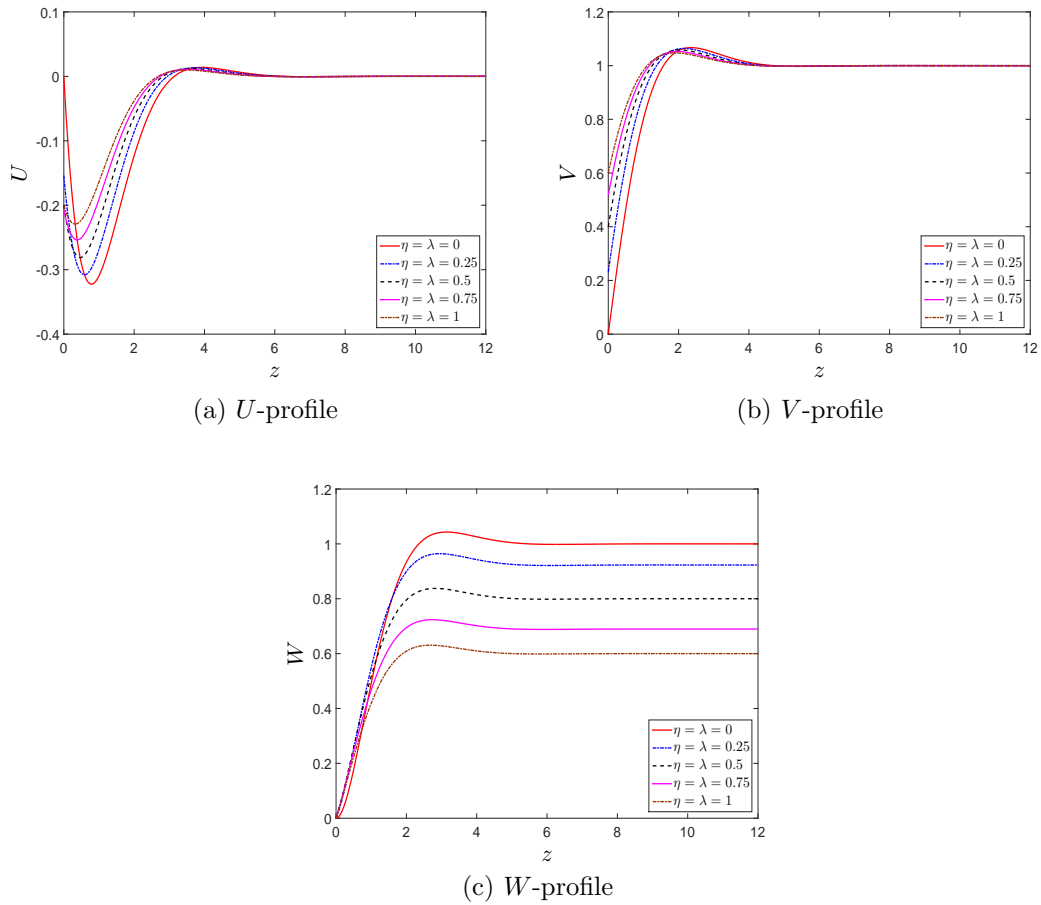


Figure 6.4: Mean-flow components of the Ekman flow ( $Ro = 0$ ) in the case of isotropic roughness ( $\eta = \lambda \neq 0$ ).

sented in Figures 6.2(b)-6.6(b), and they reveal that the wall value of the component increases for each flow as roughness is increased; this is similar to the concentric groove case discussed in Chapter 5. However, this is a direct implication of the partial slip boundary conditions (2.19) as  $\eta \neq 0$ . As a result, the resisting torque  $T$  in (2.21) also reduces for each non-zero Rossby flow, but the rate of reduction is less than the concentric grooves case. The torque is equal to zero for the Ekman flow as might be expected with zero net rotation between the upper and lower flows.

Our main findings in this section for each particular flow in the BEK system indicate that the effect of isotropic roughness on the properties of mean flow components are similar to the effects observed in the concentric grooves case, but less pronounced. Therefore, the effects can be seen as a combination of the effects ob-

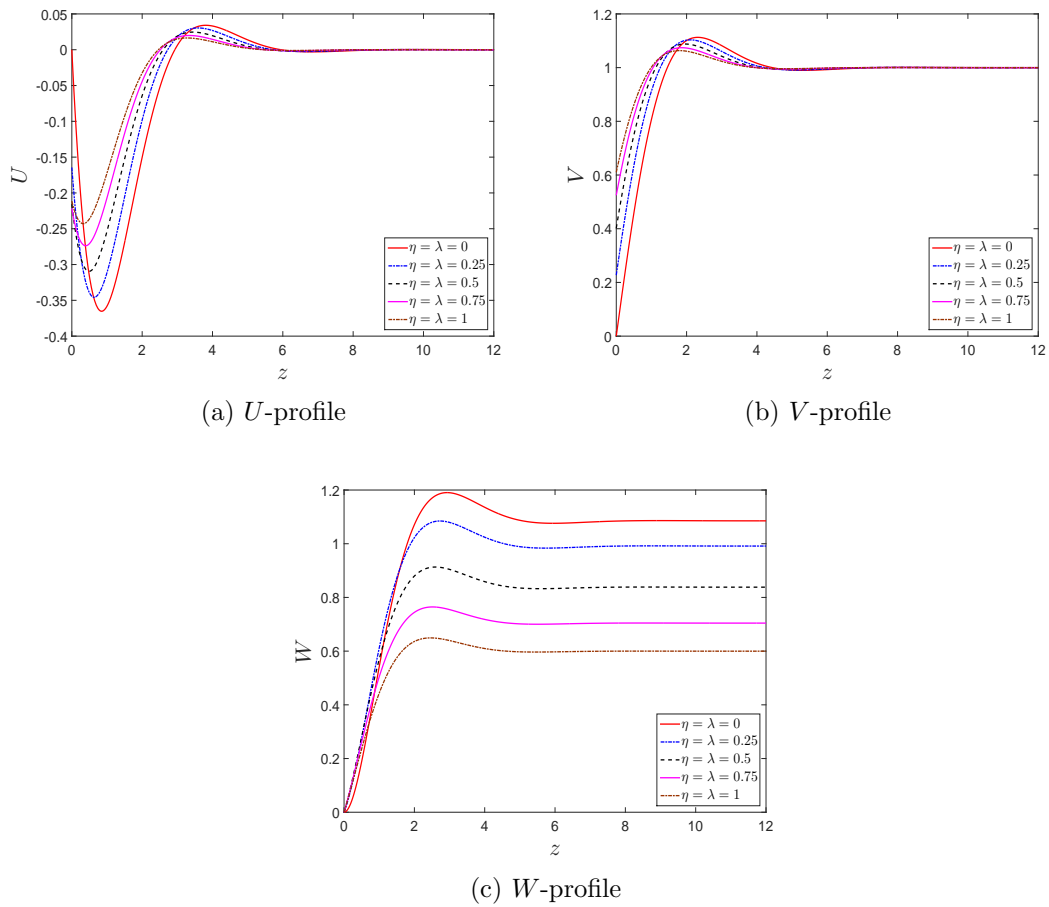


Figure 6.5: Mean-flow components for  $Ro = 0.5$  in the case of isotropic roughness ( $\eta = \lambda \neq 0$ ).

served for radial and concentric grooves in §4.2 & §5.2, respectively. Furthermore, the effects of increased roughness on the oscillatory behaviour of the flow components are similar to the responses seen from surface mass flux and the distribution of a uniform magnetic field.

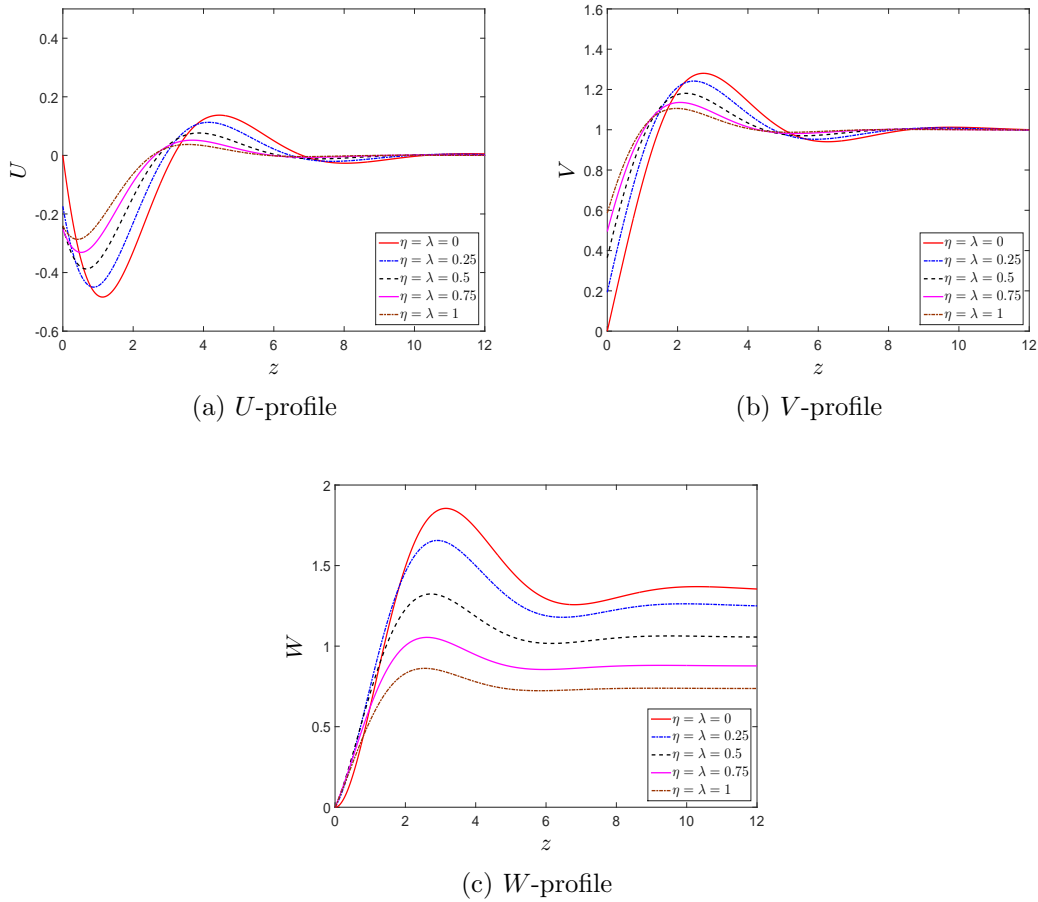


Figure 6.6: Mean-flow components of the Bödewadt flow ( $Ro = 1$ ) in the case of isotropic roughness ( $\eta = \lambda \neq 0$ ).

### 6.3. The convective instability analysis

In this section we are concerned with the occurrence of convective instabilities in the case of isotropic roughness. The convective instability is determined by the computed solutions of the perturbation equations (2.40)-(2.41). The solutions are obtained by the spectral Chebyshev method described in §3.2. We analyse the characteristics of convective instability in terms of neutral curves in §6.3.1 and the growth rates in §6.13. We suppose in the first instance that the flow is not absolutely unstable. As a result, in the Briggs-Bers procedure we can set the imaginary part of the frequency to zero, so that  $\omega_i = 0$ . To produce neutral curves of convective instability we also insist that the vortices rotate with the lower disk surface, thereby

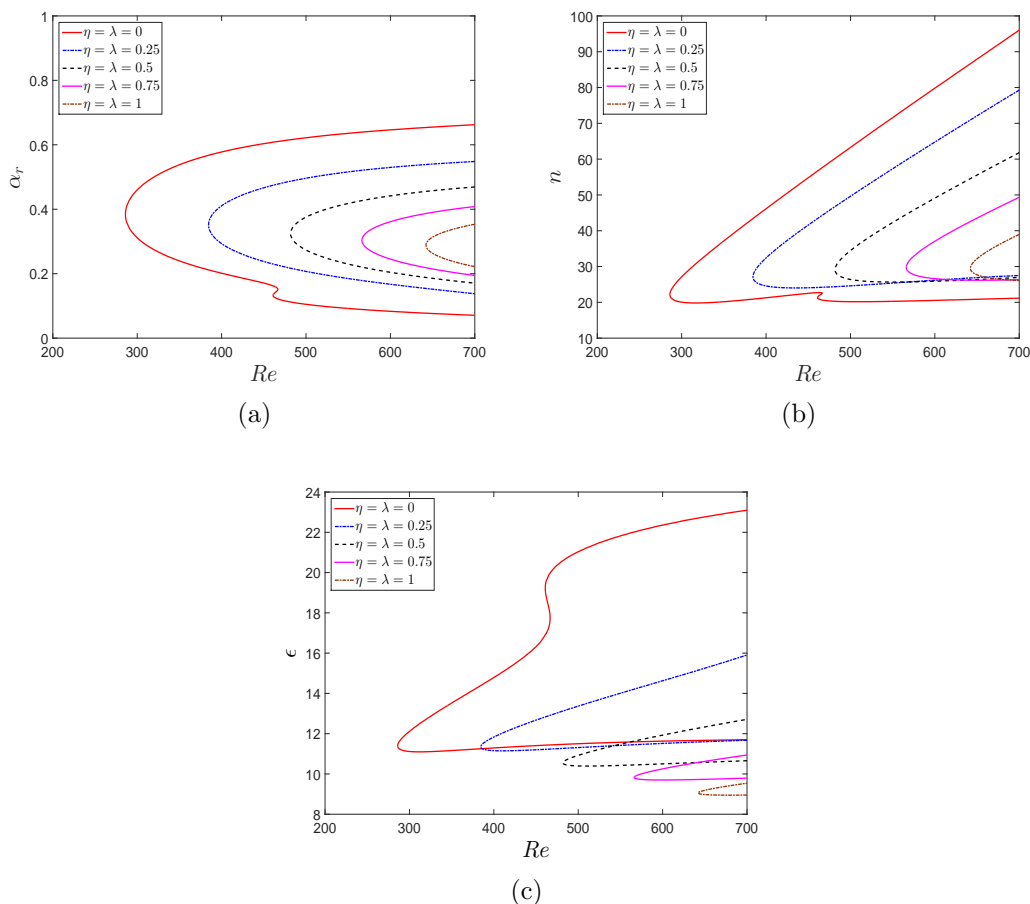


Figure 6.7: Neutral curves of the convective instability of the von Kármán flow in the case of azimuthally-anisotropic roughness ( $\eta = \lambda \neq 0$ ).

the real part of the frequency  $\omega_r = 0$ , and then the radial wavenumber  $\alpha$  and the azimuthal wavenumber  $\beta$  are computed.

### 6.3.1. Neutral curves

In this section we present neutral curves of the stability of the boundary layer flows belonging to the BEK system in the  $(Re, \alpha_r)$ ,  $(Re, n)$  and  $(Re, \epsilon)$ -planes in the case of isotropic surface roughness. Each curve encloses a region in which the boundary layers are convectively unstable. Two spatial branches are found that determine the convective instability characteristics for each size of roughness. These branches arise from crossflow and streamline-curvature instability modes and are identical to branches 1 & 2 discussed in §4.3.1; they are not discussed here for this

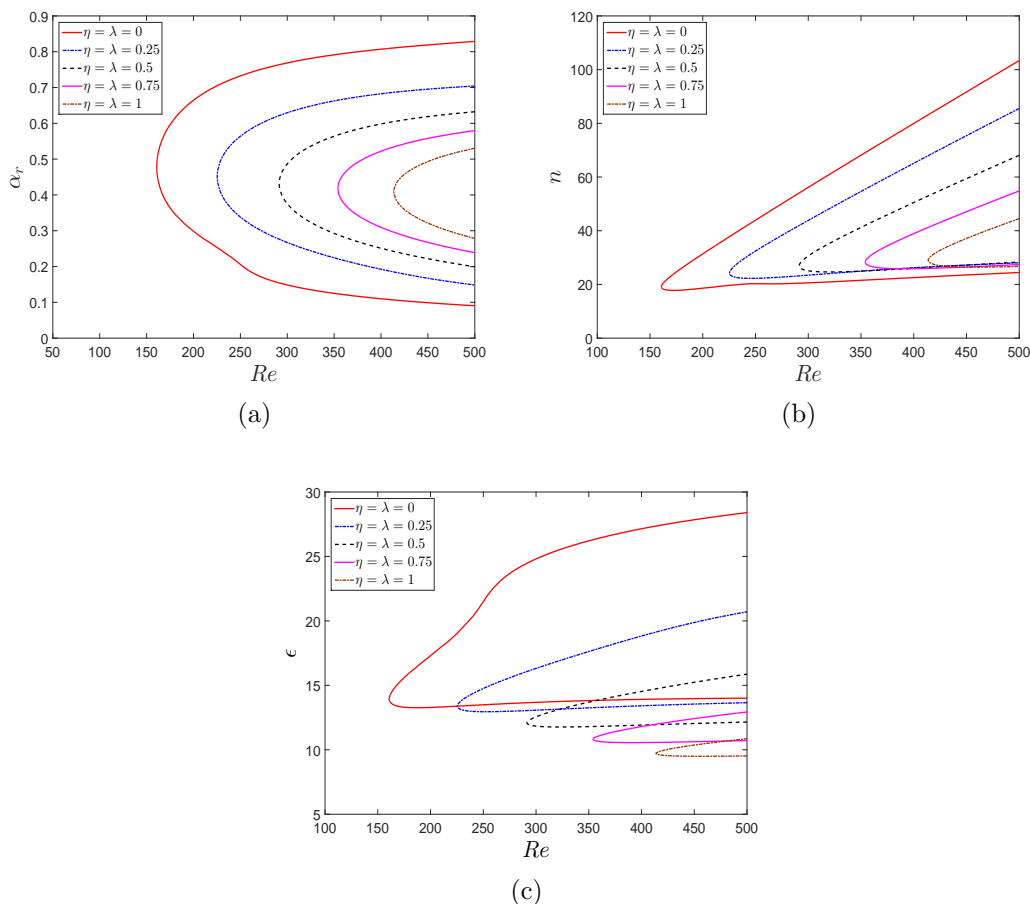


Figure 6.8: Neutral curves of the convective instability for  $Ro = -0.5$  in the case of isotropic roughness ( $\eta = \lambda \neq 0$ ).

reason.

The solutions of the perturbation equations (2.40)-(2.41) are obtained using the spectral Chebyshev method discussed in §3.2.1. Figure 6.7 presents the effects of isotropic roughness on the neutral curves of the von Kármán flow. These curves are consistent with those of Cooper *et al.* (2015) and are included here for completeness. The effects of isotropic roughness on neutral curves of other flows in the BEK system are quite similar to the von Kármán flow, as is evidenced in Figures 6.8 - 6.11.

Figures 6.7(a) - 6.11(a) clearly reveal that increasing levels of isotropic roughness has a strong stabilisation effect on both of the Type I and Type II instability modes of each flow in the BEK system. The Type II mode, that appears as the lower lobe in smooth cases of each flow, vanishes even for modest levels of isotropic roughness.

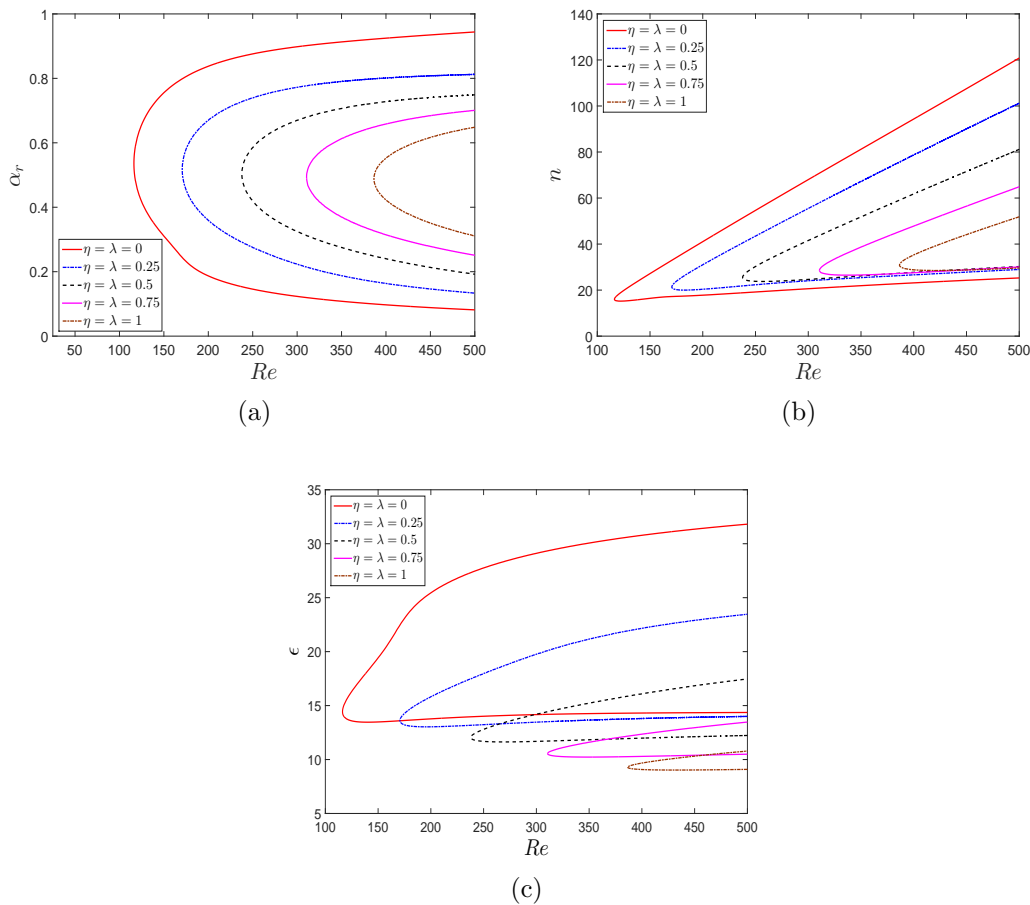


Figure 6.9: Neutral curves of the convective instability of the Ekman flow in the case of isotropic roughness ( $\eta = \lambda \neq 0$ ).

Therefore the Type I mode remains the dominant instability mechanism of each flow in the case of isotropic roughness. The critical Reynolds number at which the Type I mode onsets increases with roughness level for each flow. Furthermore, the width of instability region shrinks with an increase in the roughness level. Both are significant stabilising effects.

Figures 6.7(b) - 6.11(b) show the effects of isotropic roughness on the number of vortices  $n$  for each flow in the system. Clearly the number of vortices decreases substantially along the upper branch of the neutral curves as roughness is increased. However, there is a slight increase in the number of vortices along the lower branches of the neutral curves for larger values of the roughness parameter. Those changes in  $n$  appear to be the combined effects of azimuthal and radial roughness cases,

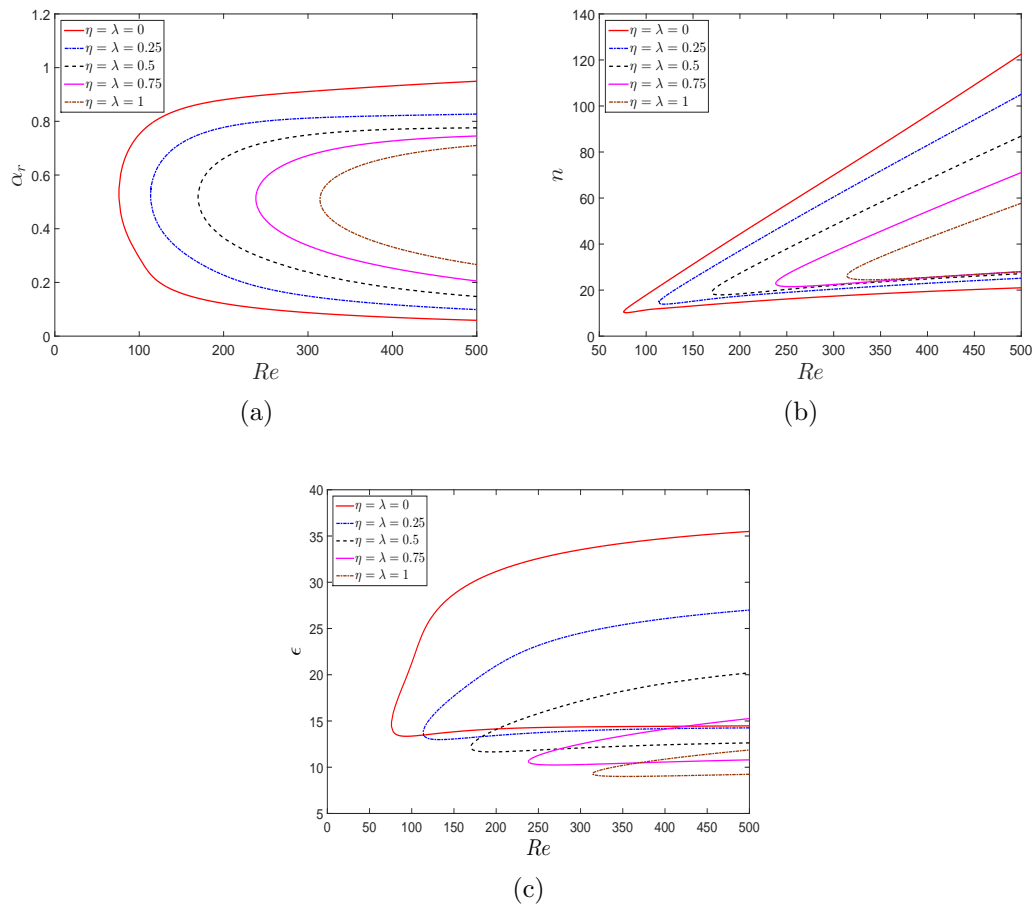


Figure 6.10: Neutral curves of the convective instability for  $Ro = 0.5$  in the case of isotropic roughness ( $\eta = \lambda \neq 0$ ).

because radial grooves lead to an increase in  $n$  while concentric grooves leads to a decrease, as discussed in §4.3.1 & §5.3.1. The effects of isotropic roughness on the vortex angle are presented in Figures 6.7(c) - 6.11(c). In contrast to the number of vortices, the effect of increasing isotropic roughness is to decrease the vortex angle of each flow in the system along both the upper and lower branches. However, the strength of the decreasing effect reduces along the lower branch.

It is also worthwhile to note that the strength of the stabilising effects of isotropic roughness is sensitive to the Rossby number and to gain a better understand of this sensitivity we compare the stability characteristic of all flows in the BEK system for a moderate level of isotropic roughness,  $\eta = \lambda = 0.5$ . Figure 6.12(a) clearly shows that the flows become increasingly unstable in terms of critical Reynolds number as

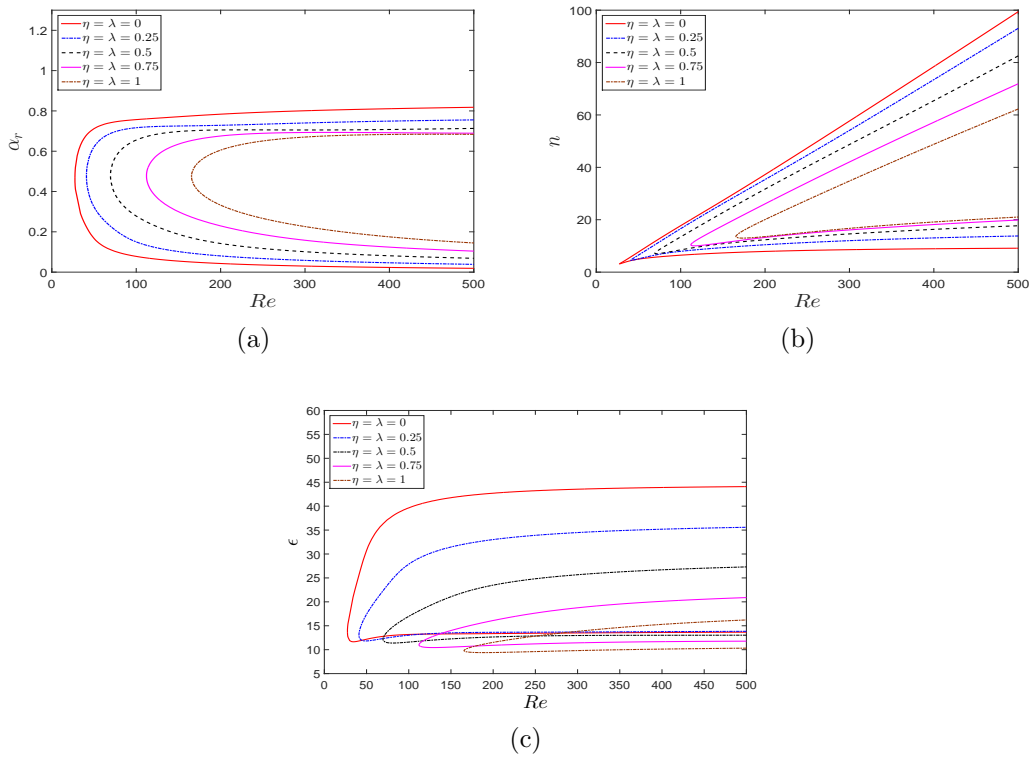


Figure 6.11: Neutral curves of the convective instability of the Bödewadt flow in the case of isotropic roughness ( $\eta = \lambda \neq 0$ ).

the Rossby number increases from the von Kármán flow,  $Ro = -1$ , to the Bödewadt flow,  $Ro = 1$ . This behaviour is similar to that obtained in the smooth disk case (Lingwood, 1997). The width of the instability region expands with increased surface roughness from  $Ro = -1$  to  $Ro = 0.5$ , whereas it shrinks slightly for  $Ro = 1$ .

Figure 6.12(b) demonstrates that the number of vortices  $n$  at the critical Reynolds number is nearly unaffected by increased roughness for the negative Rossby number flows whilst a sharp reduction is obtained for positive Rossby number flows. However, the number of vortices increases from  $Ro = -1$  to  $Ro = 0$  and remains nearly unchanged for positive Rossby number flows in the smooth case. Similarly, the vortex angle at the critical Reynolds number increases sharply between  $Ro = -1$  to  $Ro = -0.5$  flows and remains nearly unchanged for the other flows as evidenced in Figure 6.12(c). This behaviour is quite similar to the smooth case.

The numerical predictions of the critical parameters at the onset of convective instability are presented in Table 6.2 for each flow discussed previously. The critical

The von Kármán flow,  $Ro = -1$ 

Parameter	$Re$	$n$	$\epsilon$
$\eta = \lambda = 0$	<b>286.05</b> (460.92)	<b>22.20</b> (21.28)	<b>11.40</b> (19.28)
$\eta = \lambda = 0.25$	<b>384.53</b> (-)	<b>27.04</b> (-)	<b>11.35</b> (-)
$\eta = \lambda = 0.5$	<b>481.64</b> (-)	<b>29.13</b> (-)	<b>10.54</b> (-)
$\eta = \lambda = 0.75$	<b>566.24</b> (-)	<b>29.90</b> (-)	<b>9.82</b> (-)
$\eta = \lambda = 1$	<b>642.16</b> (-)	<b>29.57</b> (-)	<b>9.05</b> (-)

The related flow for  $Ro = -0.5$ 

Parameter	$Re$	$n$	$\epsilon$
$\eta = \lambda = 0$	<b>160.81</b> (-)	<b>19.09</b> (-)	<b>13.97</b> (-)
$\eta = \lambda = 0.25$	<b>225.34</b> (-)	<b>24.12</b> (-)	<b>13.35</b> (-)
$\eta = \lambda = 0.5$	<b>291.39</b> (-)	<b>26.91</b> (-)	<b>12.11</b> (-)
$\eta = \lambda = 0.75$	<b>354.06</b> (-)	<b>28.14</b> (-)	<b>10.79</b> (-)
$\eta = \lambda = 1$	<b>413.69</b> (-)	<b>29.08</b> (-)	<b>9.72</b> (-)

The Ekman flow,  $Ro = 0$ 

Parameter	$Re$	$n$	$\epsilon$
$\eta = \lambda = 0$	<b>116.26</b> (-)	<b>16.04</b> (-)	<b>14.33</b> (-)
$\eta = \lambda = 0.25$	<b>170.66</b> (-)	<b>21.45</b> (-)	<b>13.75</b> (-)
$\eta = \lambda = 0.5$	<b>237.79</b> (-)	<b>25.55</b> (-)	<b>12.03</b> (-)
$\eta = \lambda = 0.75$	<b>310.63</b> (-)	<b>28.65</b> (-)	<b>10.89</b> (-)
$\eta = \lambda = 1$	<b>386.49</b> (-)	<b>30.85</b> (-)	<b>9.17</b> (-)

The related flow for  $Ro = 0.5$ 

Parameter	$Re$	$n$	$\epsilon$
$\eta = \lambda = 0$	<b>75.89</b> (-)	<b>10.52</b> (-)	<b>14.63</b> (-)
$\eta = \lambda = 0.25$	<b>113.49</b> (-)	<b>14.62</b> (-)	<b>13.46</b> (-)
$\eta = \lambda = 0.5$	<b>169.74</b> (-)	<b>18.99</b> (-)	<b>12.17</b> (-)
$\eta = \lambda = 0.75$	<b>238.21</b> (-)	<b>22.96</b> (-)	<b>10.61</b> (-)
$\lambda = 1$	<b>314.21</b> (-)	<b>26.20</b> (-)	<b>9.28</b> (-)

The Bödewadt flow,  $Ro = 1$ 

Parameter	$Re$	$n$	$\epsilon$
$\eta = \lambda = 0$	<b>27.38</b> (-)	<b>3.12</b> (-)	<b>14.32</b> (-)
$\eta = \lambda = 0.25$	<b>41.02</b> (-)	<b>4.55</b> (-)	<b>12.60</b> (-)
$\eta = \lambda = 0.5$	<b>69.50</b> (-)	<b>7.22</b> (-)	<b>12.03</b> (-)
$\eta = \lambda = 0.75$	<b>112.15</b> (-)	<b>10.45</b> (-)	<b>10.88</b> (-)
$\eta = \lambda = 1$	<b>165.52</b> (-)	<b>13.64</b> (-)	<b>9.74</b> (-)

Table 6.2: Critical values of observable parameters at the onset of convective instability of both modes for the boundary layers in the BEK system in the case of isotropic roughness. Type I and (Type II). The most dangerous mode is indicated as bold text in terms of critical Reynolds number.

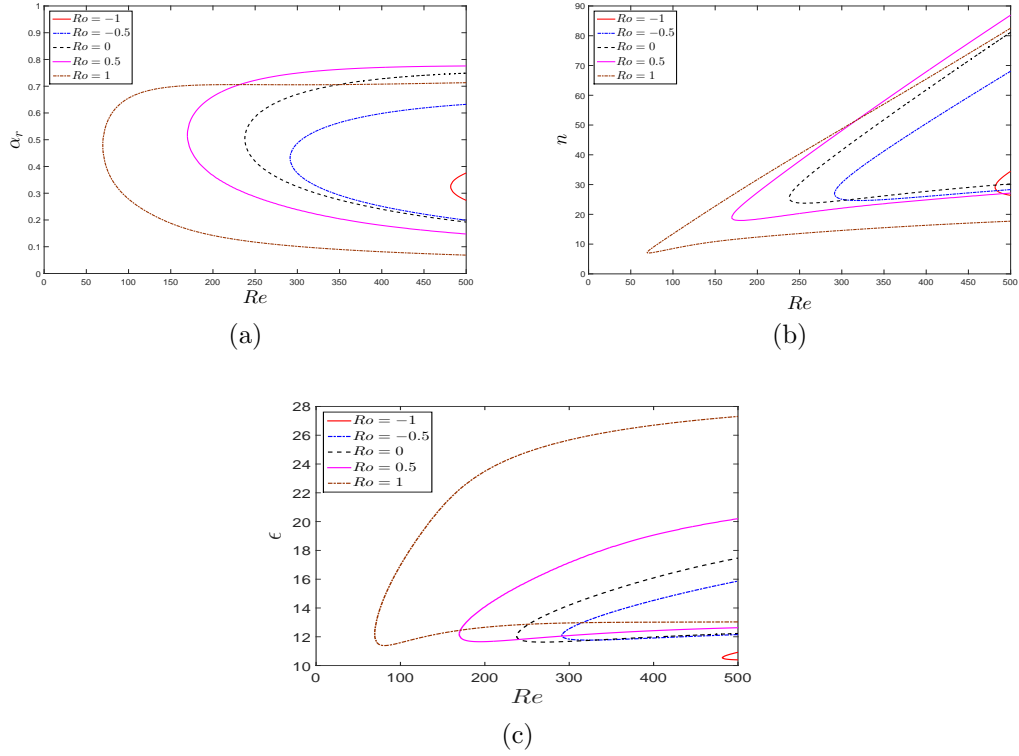


Figure 6.12: Neutral curves of the convective instability of the particular flows in the BEK system in the case of a moderate value of isotropic roughness,  $\eta = 0.5$ .

values of the Type I mode are in very good agreement with the existing results in the literature for the BEK system and those due to Cooper *et al.* (2015).

### 6.3.2. The growth rates

We now consider the effect of isotropic roughness on the growth rates of the instability modes of the BEK boundary layer flows. In contrast to radial and concentric grooves, it is also possible to produce these curves for the Bödewadt flow after a threshold value of the isotropic roughness parameter has been surpassed. In other words, the early onset of the “branch exchange” is delayed substantially by increased isotropic roughness. The details for that issue will be discussed in §6.5.

The growth rates of the Type I instability within the BEK system flows at  $Re = Re_{critical} + 25$  are presented in Figure 6.13 as a function of the vortex number  $n$  at each size of roughness. Here  $Re_{critical}$  is the critical Reynolds number presented

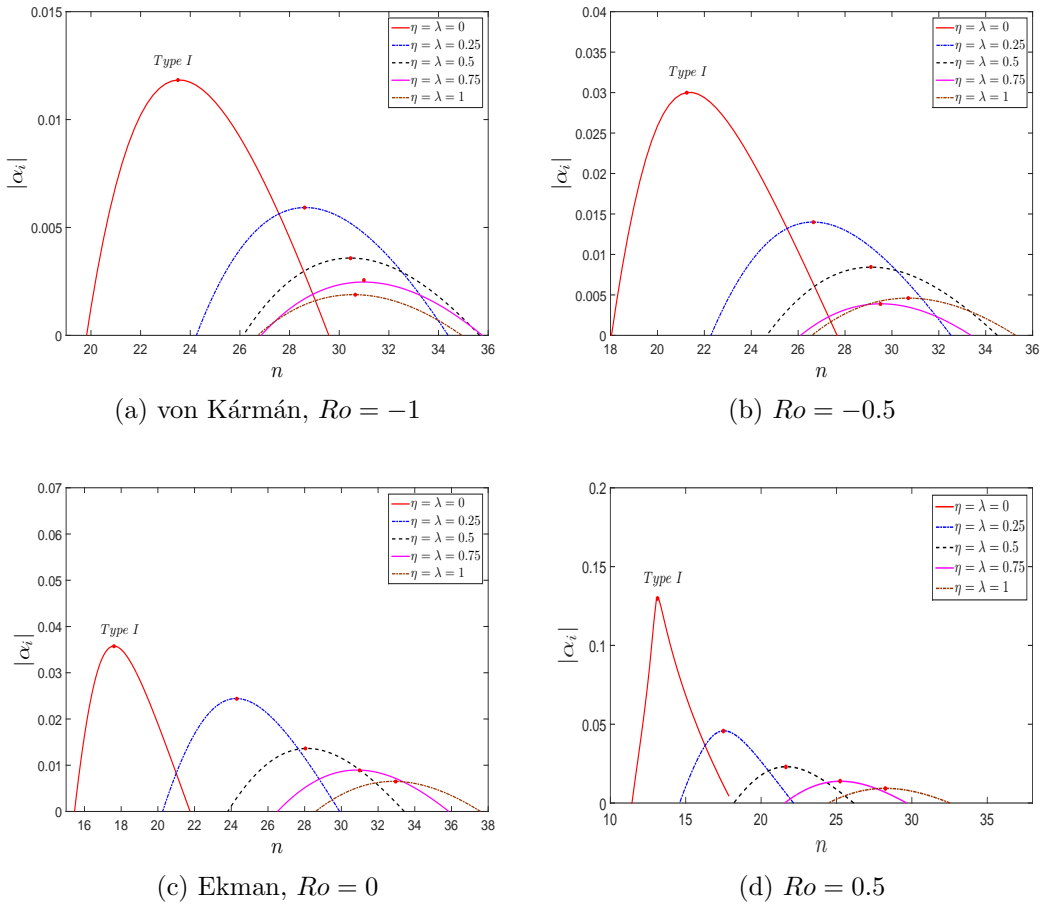


Figure 6.13: Growth rates of Type I instability mode within the BEK boundary layer flows as a function of vortex number  $n$  at  $Re = Re_{critical} + 25$  in the case of isotropic. The red dots indicates the most rapidly growing mode for Type I.

in Table 6.2 for the onset of the mode in the case of isotropic roughness. Figure 6.13 clearly reveals the stabilising effect of isotropic roughness on the Type I mode of each flow as the value of the maximum growth rate indicated by a red dot decreases for increased roughness. Furthermore, location of the maximum growth rate shifts to higher values of  $n$ , indicating an increase in the number of vortices as an effect of increased surface roughness level. A similar discussion of the growth rates for the von Kármán flow has been provided by Cooper *et al.* (2015) and we include here our results for this flow as a validation.

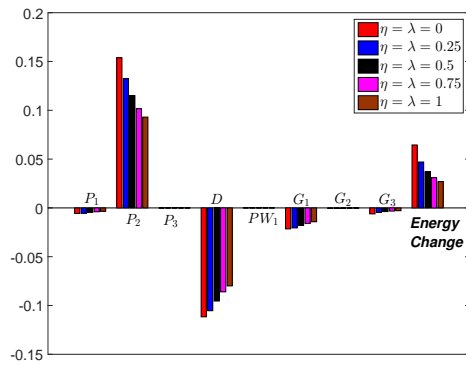
## 6.4. Energy Analysis

In this section we analyse the effects of isotropic roughness on the BEK system of boundary layer flows by solving the energy balance equation (2.50). As discussed in §4.4, this equation can be solved for any eigenmode of the perturbation equations (2.40)-(2.41).

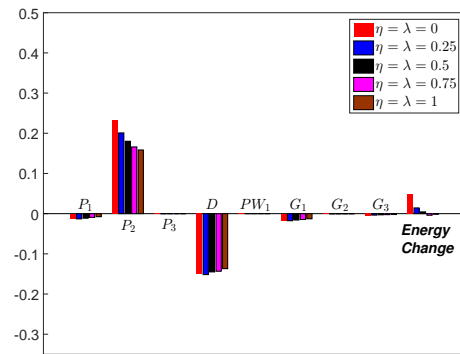
As discussed in §6.3.1, the Type II mode disappears for even modest levels of isotropic roughness in each flow of the BEK system. Therefore, we only discuss the energy balance for the Type I mode of instability here. We do this by performing the energy balance at the location of maximum amplification that was discussed in previous section at  $Re = Re_{critical} + 25$ . Here  $Re_{critical}$  is the critical Reynolds number presented in Table 6.2 for the onset of the Type I mode of instability in the case of isotropic roughness. Our growth rate results have shown that the interaction with an absolutely unstable area is delayed for some levels of isotropic roughness for the Bödewadt flow. Therefore, we can carry out the energy balance calculations for all levels of the roughness that are possible to produce growth rate plots at  $Re = Re_{critical} + 25$  for the Type I mode.

Figure 6.14 shows the energy balance calculation of the Type I mode for isotropic roughness. Clearly the stabilisation effect obtained for each flow in the system is due to a strong decrease in energy changes of the flows as roughness is increased. This effect arises mainly from the changes in the energy production term  $P_2$  and in the energy dissipation term  $D$ . Both energy production and dissipation in each flow decrease for higher values of the roughness parameter. Furthermore, the energy removing effects of the  $G_1$ ,  $G_2$  and  $G_3$  terms arising from the streamline curvature and the three dimensionality of the mean flow result in an energy production effect for positive values of the Rossby number. In other words, these terms contribute to energy production in the system.

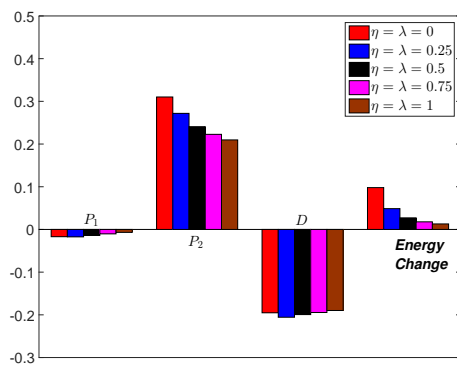
It is also possible to provide some explanation about the energy trends of the BEK system of flows by analysing the form of azimuthal velocity perturbation,  $\hat{v}$ , and the axial velocity perturbation,  $\hat{w}$ . These profiles contribute to the dominant



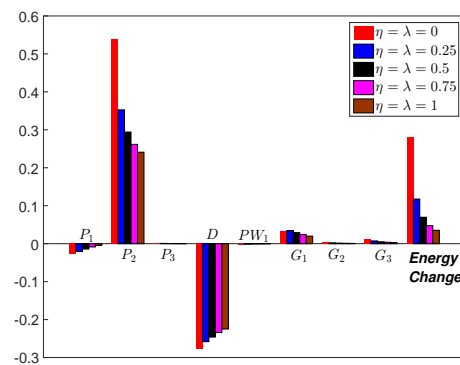
(a) von Kármán,  $Ro = -1$



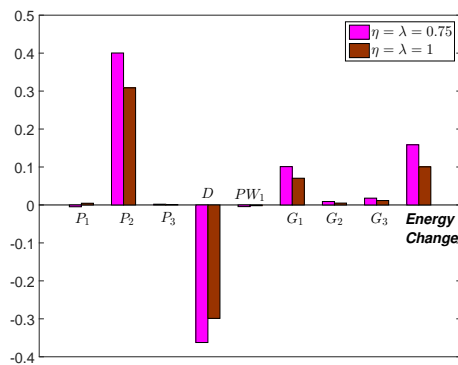
(b)  $Ro = -0.5$



(c) Ekman,  $Ro = 0$



(d)  $Ro = 0.5$



(e) Bödewadt,  $Ro = 1$

Figure 6.14: Energy balance at the location of maximum amplification of the BEK boundary layer flows at  $Re = Re_{critical} + 25$  for isotropic roughness. The terms are normalised by the mechanical energy flux of the most dangerous mode within each figure.

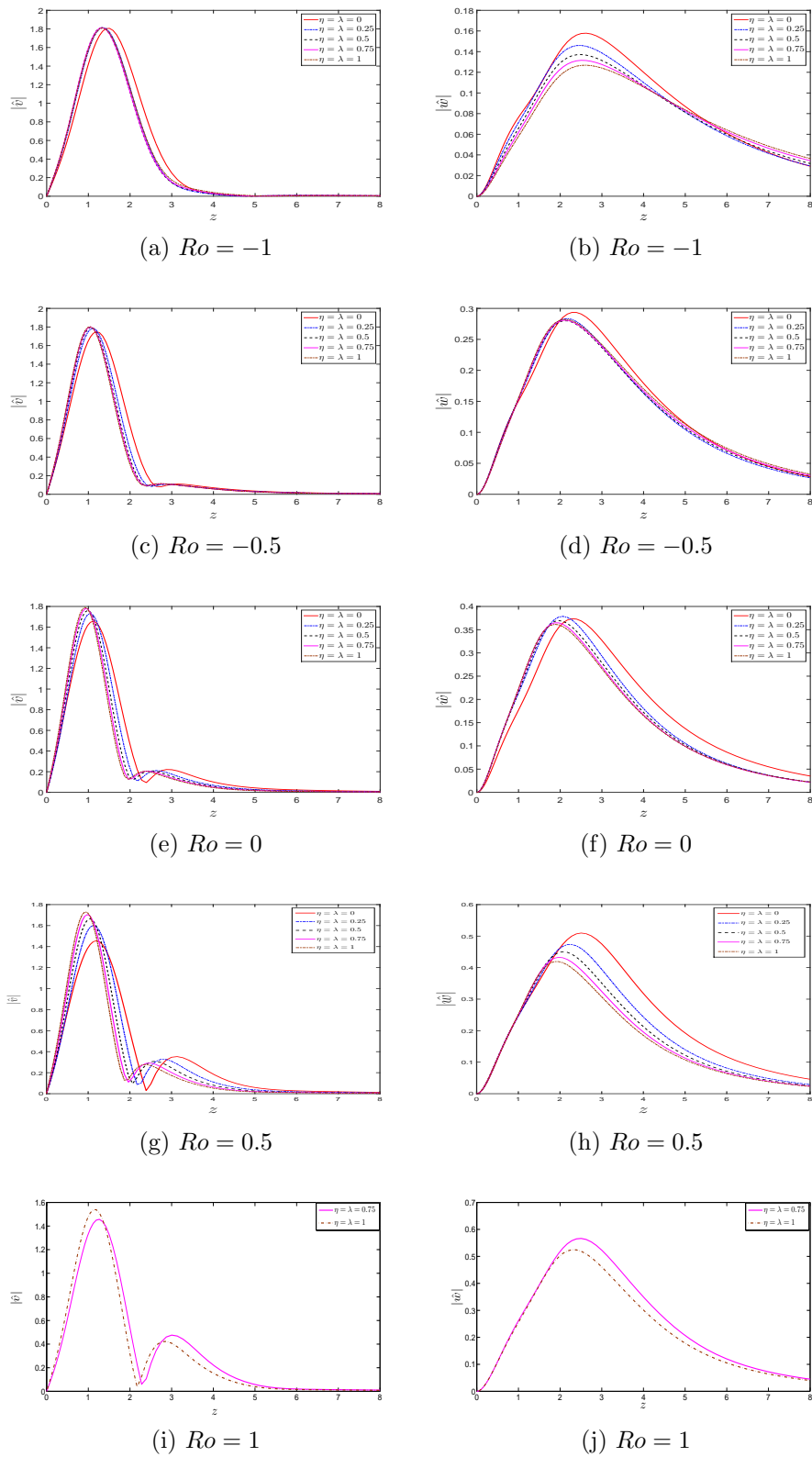


Figure 6.15: Type I mode profiles for the azimuthal and the axial disturbance velocity profiles of the BEK flows at  $Re = Re_{critical} + 25$  in the case of an isotropically rough disk.

	Ekman flow, $Ro = 0$	Bödewadt flow, $Ro = 1$
$\eta = \lambda = 0$	219 ~ 220	27 ~ 28
$\eta = \lambda = 0.25$	> 1000	45 ~ 46
$\eta = \lambda = 0.5$	> 1000	104 ~ 105
$\eta = \lambda = 0.75$	> 1000	475 ~ 476
$\eta = \lambda = 1$	> 1000	> 1000

Table 6.3: Critical Reynolds number for the stationary Type I mode interacting with the absolute instability region inside the neutral curves of the BEK system flows in the case of isotropic roughness.

energy production term  $P_2$  and energy dissipation term  $D$ . The magnitudes of these two disturbance profiles are presented in Figure 6.15 for the BEK system of flows in the case of an isotropically rough disk for the Type I instability mode. It is seen that the general form of both disturbance profiles are not changed with the profiles being translated towards the wall as the roughness is increased. The strong decrease of the  $P_2$  term for each flow is due to the reduction in the amplitude of the axial velocity perturbation,  $\hat{w}$ . The reduction in the dissipation rate of the system is due to the increase of the maximum value of the azimuthal velocity profile  $\hat{v}$ .

## 6.5. Absolute instability

Our growth rate results discussed in §6.3.2 have revealed that sufficiently large sizes of isotropic roughness suppress the coalescing of the Type I and Type III instability modes, that leads to the “branch exchange” issue for all flows of the BEK system. Therefore, the onset of absolute instability could be delayed to higher Reynolds numbers.

Table 6.3 shows that the critical Reynolds numbers for the stationary Type I mode at which convective instability region starts to interact with the absolute instability region in the case of isotropic roughness. It is clear that the onset of the

interaction is delayed to higher Reynolds numbers for all the BEK system of flows as roughness is increased. The delaying effect of isotropic roughness is not as strong as for azimuthally anisotropic roughness for the flows between  $Ro = -1$  and  $Ro = 0.5$ . However, it has a certain delaying effect on the Bödewadt flow while the former does not. Furthermore, it is stronger compared to radially anisotropic roughness for all Rossby flows in the system. Indeed, these results lead to the prediction that isotropic surface roughness can restrict the onset of absolute instability to higher Reynolds numbers compared to a smooth disk.

## 6.6. Conclusion

In this chapter we have investigated the effects of isotropic roughness on the convective instability of stationary disturbances in the BEK family of boundary layer flows. We have presented solutions of the mean flow equations obtained using the partial-slip approach of Miklavcic & Wang (2004) without modification. The computed mean flow components are in good agreement with those in the literature for the smooth surface cases at all values of  $Ro$ . The computed mean flow components of the von Kármán and the Bödewadt flows are qualitatively consistent with those presented by Sahoo *et al.* (2014), Cooper *et al.* (2015) and Garrett *et al.* (2016). Our findings have revealed that isotropic roughness acts to decrease the amplification of the oscillatory behaviour of the steady flows through the axial direction and the boundary layer thickness of each flow.

We have then conducted a linear stability analysis and reveal that isotropic roughness has a strong stabilising effect on both of the Type I and Type II modes instability in terms of postponing the onset of the convective instability and the width of the unstable area enclosed by the neutral curves at all Rossby numbers. It is observed that increased surface roughness at all values of  $Ro$  acts to decrease the number of vortices along the upper branch and increase them along the lower branch. The effect of isotropic roughness is to reduce the value of the vortex angle along both branches. We have also presented supporting results by considering

the growth rates of each instability mode and have conducted an energy balance analysis at the locations of the maximum amplifications for particular flows in the system. Moreover, our findings indicate that isotropic surface roughness can be a stabilisation mechanism that could be used to delay the onset of absolute instability for rotating disk flows.

The observed stabilising effect in this case of roughness on the instability modes are similar to the effects of other flow-control methodologies for the BEK system: the surface suction technique, studied theoretically by Lingwood & Garrett (2011) and imposing increased uniform magnetic field normal to the disk as studied by Jasmine & Gajjar (2005). Furthermore, we find that the response of the physical mechanisms that lead to transition in the boundary layer is sensitive to the Rossby number of the system as with the surface suction technique.

# Chapter 7

## Conclusion

“This thesis aims to investigate whether distributed surface roughness could be used as a passive drag reduction technique for the BEK system of flows. If it can, what is the right sort roughness”. To answer those questions, we have investigated the effects of particular types of distributed surface roughness, anisotropic and isotropic, on the convective stability characteristics of the stationary disturbances in the BEK system of flows. Each analysis has been presented separately and a summary of the main findings from each investigation are given briefly here. In particular, in §7.1 we present a comparison of the effects of each surface roughness and draw some general conclusions. As a result of the main findings of this thesis, suggestions for future research are identified in §7.2.

### 7.1. Comparison of main results

Cooper *et al.* (2015) and Garrett *et al.* (2016) have previously published results concerning the effects of surface roughness on the von Kármán flow and this thesis is designed to extend those investigations to predict the effects of surface roughness on the convective instability characteristics of the broader BEK system of flows. The steady boundary layer flows within the BEK system are parametrised by the Rossby number,  $Ro$ , and the distinct surface roughness types have been modelled using the partial-slip approach of Miklavcic & Wang (2004) without modification. Our results

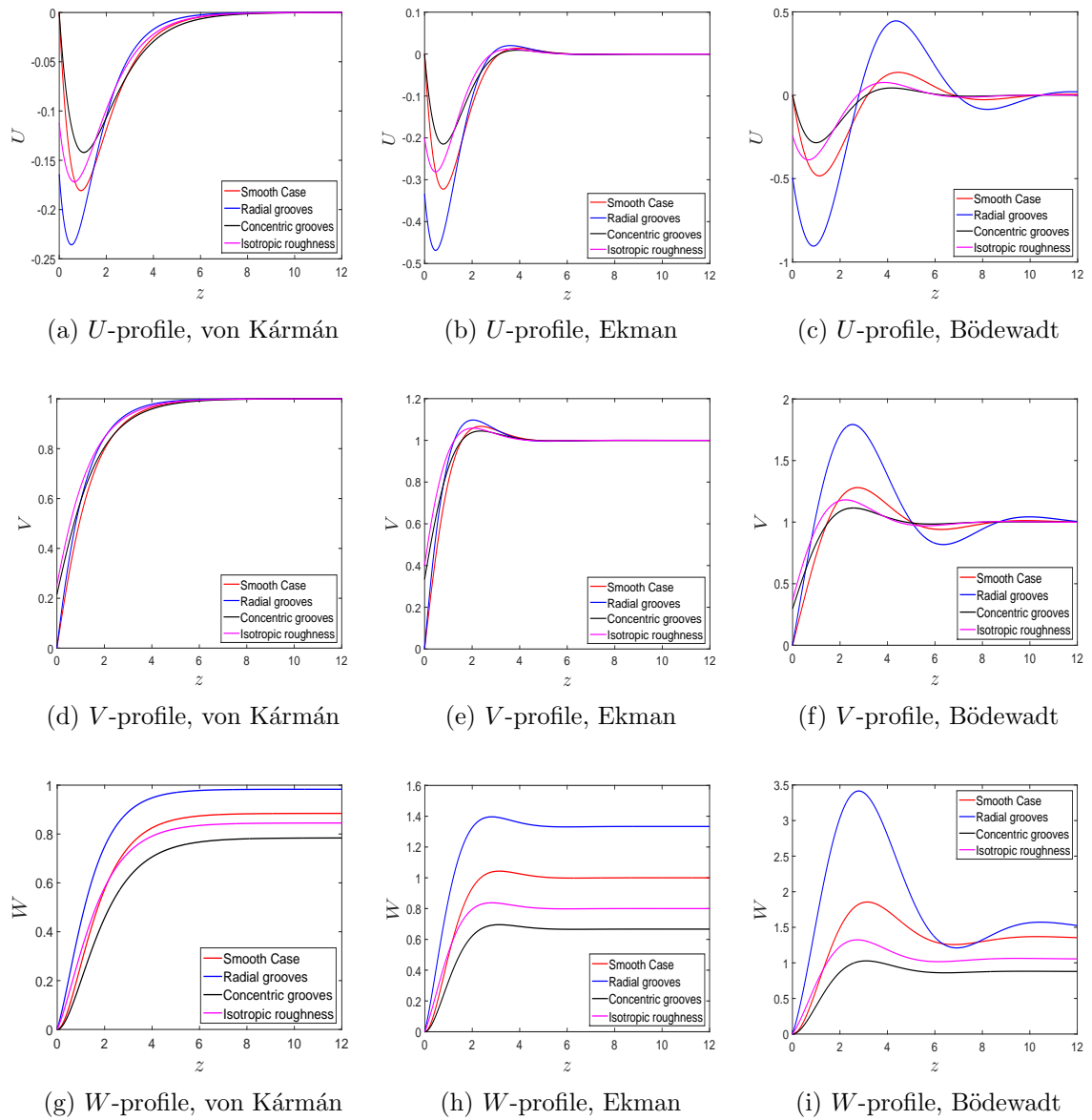


Figure 7.1: Comparative mean-flow components of the main flows of the BEK system. The size of roughness is set to 0.5 in each rough case.

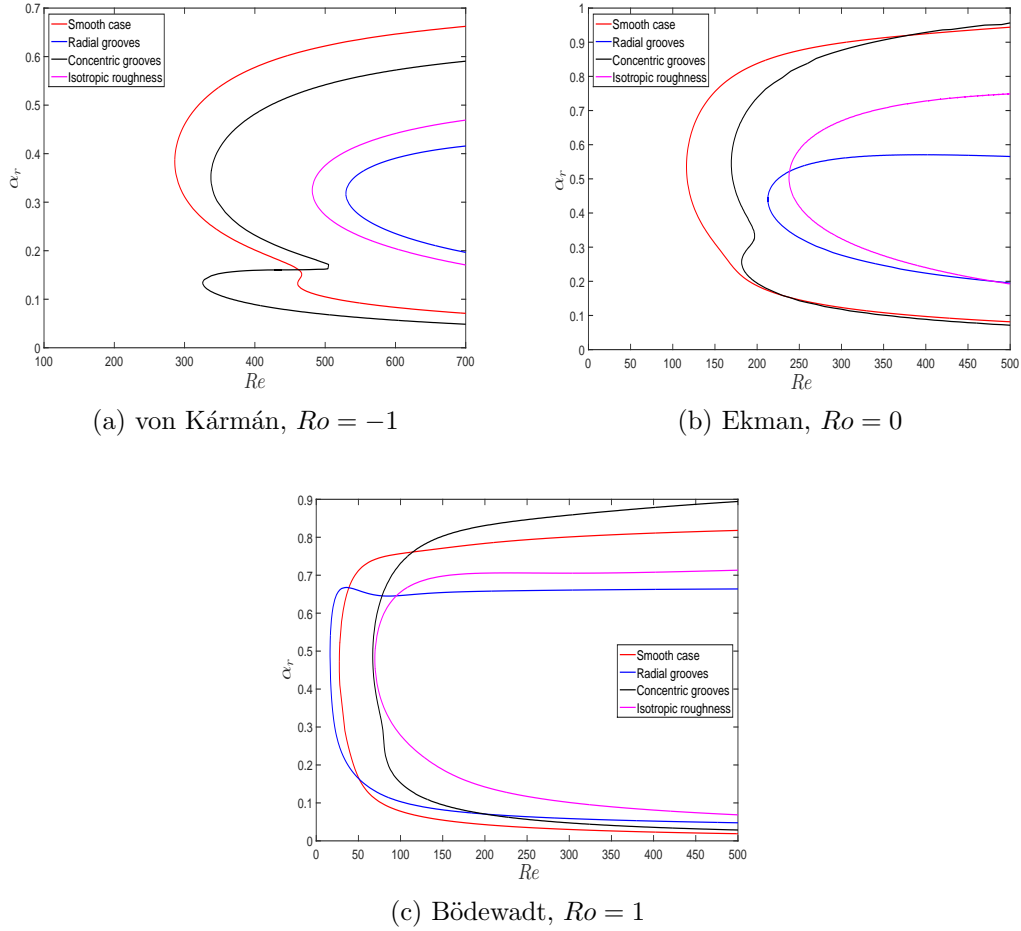


Figure 7.2: Comparative convective neutral curves of the main flows in the BEK system for each type of surface roughness. The size of roughness is set to 0.5 in each rough case.

are directly comparable to Cooper *et al.* (2015). The computed mean flow profiles of each flow in the BEK system have revealed that azimuthally-anisotropic roughness - radial grooves - acts to magnify the oscillatory behaviour of these flow components and also increases the magnitude of the wall jet. However, radially-anisotropic roughness - concentric grooves - and isotropic roughness have been found to have the opposite effect. This can be attributed to increased acceleration of the radial mean flow component  $U$  in the case of the radial grooves compared to the smooth case as evidenced in Figure 7.1. Moreover, the thickness of the boundary layer is reduced with increased surface roughness with the isotropic roughness showing particular sensitivity, as observed in Figure 7.1.

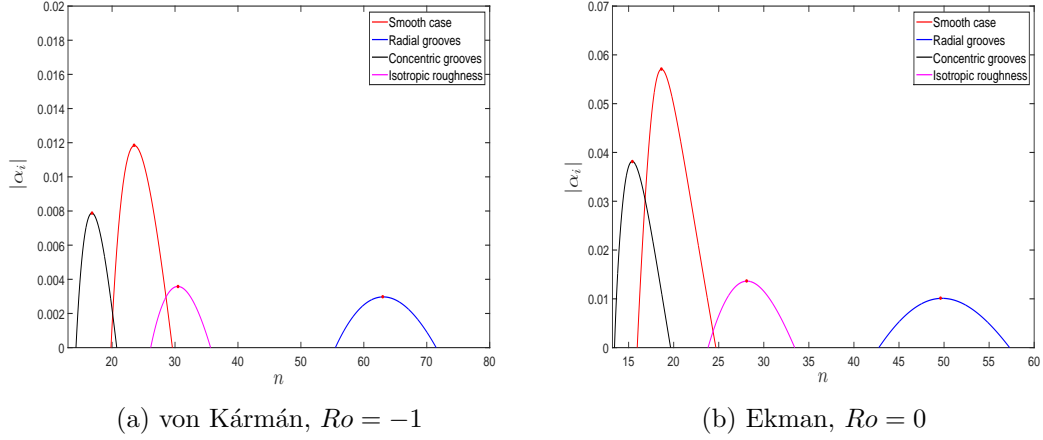


Figure 7.3: Comparative convective growth rate curves of the von Kármán and Ekman flows for the Type I mode at the location of maximum amplification of  $Re_{critical} = Re_{critical} + 25$ , where  $Re_{critical}$  corresponds the critical Reynolds number of each type of surface roughness. The size of roughness is set to 0.5 in each rough case.

A convective linear stability analysis for each of the BEK system of flows has been performed using the Chebyshev collocation method and the obtained neutral curves of the von Kármán, Ekman and Bödewadt flows are compared in Figure 7.2 at moderate levels of the roughness parameters. All roughness parameters are set to 0.5. Radial grooves are seen to have a stabilisation effect for the inviscid Type I mode of instability, as evidenced by the reduced region of instability and the increase of the critical Reynolds number at all  $Ro$ , as shown in Figure 7.2(a)-(c). However, the stabilisation effect of the radial grooves on both instability modes loses its strength as  $Ro$  changes towards positive unity. In fact, it switches to a marginally destabilising effect beyond  $Ro \approx 0.7$  as seen in Figure 7.2(a)-(c).

The concentric grooves also have a stabilising effect on the Type I mode at all  $Ro$ . However, the viscous Type II mode is destabilised by concentric grooves for each of the BEK system of flows, as seen in 7.2(a)-(c). Furthermore, concentric grooves act to promote this mode such that the mode becomes the most dangerous and is likely to be observed in experimental studies for sufficiently negative  $Ro$  and a sufficiently large roughness parameter. For both Type I and Type II modes isotropic roughness has a universally stabilising effect for all flows of the BEK system and the strength

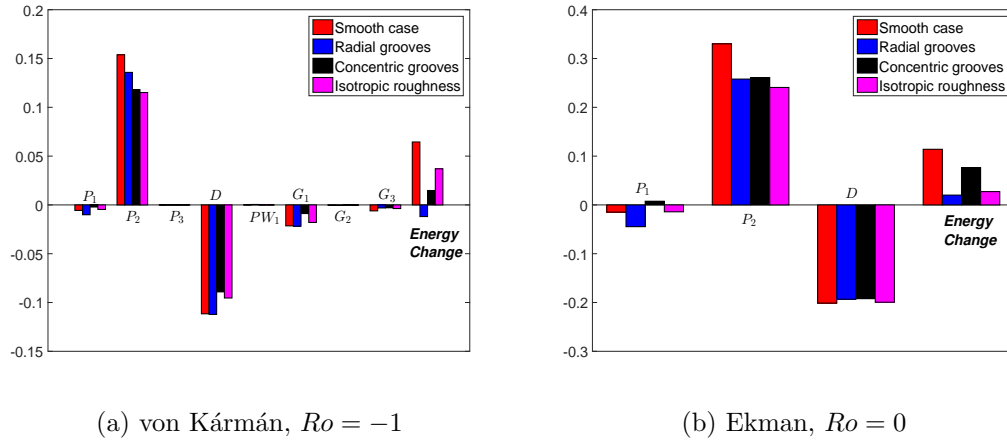
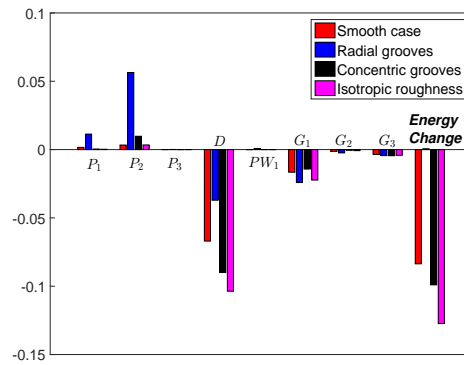
(a) von Kármán,  $Ro = -1$ (b) Ekman,  $Ro = 0$ (c) Bödewadt,  $Ro = 1$ 

Figure 7.4: Energy balance comparison of Type I mode of the BEK boundary layer flows for each roughness cases at the location of maximum amplification at  $Re = Re_{critical} + 25$ , except the Bödewadt flow. For these flow,  $Re = 400$  and  $n = 40$ . The terms are normalised by the mechanical energy flux of the most dangerous mode within each figure.

of this effect compared to anisotropic roughness cases increases with increased  $Ro$ .

The results obtained from the investigation of the convective neutral curves are supported by a study of the effects of roughness on the growth rates,  $|\alpha_i|$ , of both the Type I and Type II modes. However, the onset of absolute instability begins at very small Reynolds numbers in the Bödewadt flow and it leads to a “branch exchange” between type I and Type III modes that makes it impossible to find the location of maximum amplification of either instability mode (Mack, 1985; Lingwood & Garrett, 2011). Therefore, the effect of each roughness type is compared here only for the

von Kármán and Ekman flows. Moreover, the Type II mode is spatially damped by radial grooves and isotropic roughness and so has not been presented in the relevant chapters. The growth rate curves of the Type I mode of the von Kármán and Ekman flows are compared in Figure 7.3. This figure reveals that the maximum amplification of the most dangerous mode, indicated by a red circle on each curve, is damped by radial grooves and isotropic roughness for each flow. However, the number of vortices is approximately two times less for the isotropic case roughness. Reducing the number of vortices is a similar indication of the potential stabilising effect of surface roughness shown in the experimental study of Watanabe *et al.* (1993) for the boundary layer flows over a rotating cone.

Other complementary results have been obtained from performing an energy analysis. The main indicator to identify the effects of surface roughness on the stabilisation of the BEK system of flows is the energy change associated with them, that is, the sum of energy production and dissipation in the system. The main contributors to the energy change of the system have been identified as the term  $P_2$ , the Reynolds stress energy production term, and the term  $D$ , the viscous dissipation energy removal term. An increased energy change in a rough case compared to the smooth case indicates a destabilisation of the modes, whereas a reduced energy change indicates a stabilization. The energy balance of terms from the BEK system of flows are calculated for the Type I mode at the location of maximum amplification at  $Re = Re_{critical} + 25$  and are compared in Figure 7.4 for each surface roughness type. Here  $Re_{critical}$  is the critical Reynolds number presented in Tables 4.3, 5.2 & 6.2 for radial grooves, concentric grooves and isotropic roughness, respectively. In contrast, the energy balance calculations for the Bödewadt flow are performed at  $Re = 400$  with the number of vortices,  $n = 40$ , fixed due to the “branch exchange” issue. The value of number of vortices has been chosen for the purpose of being outside of the absolutely unstable region at  $Re = 400$ .

The behaviour of the energy balance terms are consistent with the behaviours of the neutral curves in Figure 7.2. The largest energy change, indicating the most powerful stabilisation effect, is obtained in case of the radial grooves at  $Ro = -1$ ,

	Ekman	Bödewadt
Smooth case, $\eta = \lambda = 0$	219 ~ 220	27 ~ 28
Radial grooves, $\lambda = 0.5$	> 1000	15 ~ 16
Concentric grooves, $\eta = 0.5$	463- 564	78 ~ 79
Isotropic roughness, $\eta = \lambda = 0.5$	> 1000	104 ~ 105

Table 7.1: Critical Reynolds number for the stationary Type I mode interacting with the absolute instability region inside the neutral curves of the BEK system flows in the case of isotropic roughness.

however, the energy change of this case exceeds the energy change of the smooth case as  $Ro$  is increased towards positive unity, which indicates the destabilisation of radial grooves for sufficiently high positive Rossby number flows. The energy changes of the system in the case of concentric grooves and isotropic roughness are always less than the energy change of a smooth case at all  $Ro$  and this observation supports the destabilisation effect of these types of surface roughnesses.

The final interesting finding of this thesis is the prediction of a delayed “branch exchange” occurring between the Type I and Type III modes to higher Reynolds numbers in the case of concentric grooves and isotropic roughness. Note that this prediction has been made for stationary vortices,  $\omega = 0$ , and therefore is not a complete absolute instability analysis. A complete investigation of the absolute instability mechanism requires a highly intensive study beyond the scope of this thesis. Nevertheless, this result can give credibility to the idea that the stabilization effect of certain types of distributed surface roughness could be used for delaying the onset of absolute instability and turbulence. The comparison of the critical values of the “branch exchange” is presented in Table 7.1.

The conclusions arising from this thesis are now clear. Isotropic surface roughness is shown to have the most significant effect on delaying the onset of convective instability at all values of the Rossby number. This conclusion is further supported by the damped growth of the most dangerous Type I and Type II modes. We

conclude that isotropic roughness is the most effective type of distributed surface roughness discussed in this thesis and is recommended as a passive-drag reduction mechanism for the entire BEK system of flows which are observed in rotor-stator type engineering applications.

## 7.2. Future work

Further research is needed to fully understand the effects of surface roughness on the BEK system of flows after completion of this thesis. First of all, there is no experimental study that could confirm the main findings of this thesis. An experimental investigation is required in order to validate our findings. The convective instability characteristics of the BEK system of flows are investigated here using a linear approach with the parallel flow approximation in the local scale. Therefore a natural extension of this study is to conduct a study involving a non-parallel mean flow by following the investigation of Davies & Carpenter (2003) for the von Kármán flow. The occurrence of linear global modes of the BEK system of flows, as studied by Healey (2010) in the case of von Kármán flow, over rough surfaces could be investigated to compare with the linear local modes found in this study. Investigating the effects of surface roughness on the nonlinear stability of the stationary cross flow mode of the BEK system of flows is another potential research area. Theoretical investigations of such instabilities have been presented by Gajjar (1996) for boundary layer flows over swept wings and extended to rotating disk flows by Floriani *et al.* (2000) in the smooth case. The effects of the surface roughness could also be investigated for other two-dimensional or three-dimensional boundary layer flows such as the boundary layer flows over a flat plate or a swept wing.

Another possible area of future work would be to investigate the absolute instability characteristics of the BEK flows over rough disk as the appearance of absolute instability has limited our growth rate and energy balance equations results. A similar study has been conducted by Lingwood & Garrett (2011) to investigate the effects of mass injection on the absolute instability characteristics of the BEK system

flows.

# Appendices

# Appendix A

## MATLAB codes for the convective instability analysis

In this appendix we present the Matlab codes developed for this study. The mean flow solver is presented in §A.1. The solvers of the neutral curves, the convective growth rate curves and the energy analysis are presented in §A.2.

### A.1. Mean flow solver

```
inf=15;
maxinf=27;
Ro=input('Rossby number: Ro= ');
EtaVal=input('Insert roughness parameter  $\eta$  =');
LamVal=input('Insert roughness parameter  $\lambda$  =');
markers =  $\{\text{'.'}, \text{'-'}, \text{'-.'}\}$ ;

%Initial solutions
solinit= bvpinit(linspace(0,inf,5), [0.0,0.0, -1.0, 0.0, 0.0]);
options = bvpset('AbsTol', 1e-6, 'RelTol', 1e-6, 'nmax', 100000);
z = solinit.x; phi = solinit.y;
Eta= EtaVal(j); Lambda=LamVal(j);
```

```

sol= bvp4c(@Pphiode,@Pphibc,solinit,options,Ro,Eta,Lambda);
z = sol.x; phi = sol.y;

for i=inf+1:maxinf
solinit= bvpinit(sol,[0 i]);
options = bvpset('AbsTol', 1e-40, 'RelTol', 1e-20);
sol = bvp4c(@Pphiode,@Pphibc,solinit,options,Ro,Eta,Lambda);
z = sol.x; phi = sol.y;
end
eta=z;

%Plotting mean flow components
figure(1)
axis([ 0 12 -0.5 0.5 ])
plot(z,phi(1,:), [markers{mod(j,numel(markers))+1}]);
xlabel('z'); ylabel('U(z)');
hold on

figure(2)
axis([0 10.0 0 2.2])
plot(z,phi(3,:), [markers{mod(j,numel(markers))+1}]);
ylabel('V(z)'); xlabel('z');

figure(3)
axis([0 10.0 0 4.0])
plot(z,phi(5,:), [markers{mod(j,numel(markers))+1}]);
ylabel('W(z)'); xlabel('z');

```

### A.1.1. Function for setup of the governing mean flow equations

```

function dphidz = Pphiode(z,phi,Ro,Eta,Lambda)

Co=2.0-Ro-Ro^2; % Coriolis number

```

```

dphidz = [phi(2)
          Ro*(phi(1)^2+phi(2)*phi(5)-phi(3)^2+1)-Co*(phi(3)-1.0)
          phi(4)
          Ro*(2.0*phi(1)*phi(3) + phi(4)*phi(5))+Co*phi(1)
          -2.0*phi(1)];
end

```

### A.1.2. Function for setup of the partial-slip boundary conditions

```

function bc = Pphibc (phi0,phiinf,Ro,Eta,Lambda)

bc = [phi0(1)-Lambda*phi0(2)
      phi0(3)-Eta*phi0(4)
      phi0(5)
      phiinf(1)
      phiinf(3)+1];
end

```

## A.2. Convective instability solvers

### A.2.1. Main solver

```

Ro=input('Rossby number: Ro= ');
Re=input('Reynolds number: Re= ');
InitBeta=input('Initial beta: beta= '); FinalBeta=0;

%load mean flow solutions
load 'Filename'.mat

% Number of steps and step size for Reynolds number
iR=; dR=;

```

```

% Number of steps and step size for azimuthal wavenumber beta
iB=(InitBeta-FinalBeta)/abs(dB); ;dB=;
beta=InitBeta;

%Number of Chebyshev polynomials
N=100;

i=sqrt(-1);
omega=0; %Frequency
tol=1e-2;tol2=1e-2;
etaa=0;

for i =1:iR
Rnew=R+(i-1)*dR;
Fname='Name of file saving the results';

fname=[Fname,num2str(Rnew),'.txt'];
fid=fopen(fname,'W');

%Initial calculation of eigenvalues
[C,er,z,X,u,v,w,p,U,V,W,dU,dV,dW,du,dv,dw]=chebsol(omega,...
beta,Rnew,N,Ro,phi,eta);

%Threshold to remove non-physical eigenvalues and eigenfunctions
q=find(abs(real(C))<1 & real(C)> 0 & abs(C-1/er)>1e-5);
C=C(q);X=X(:,q); u=u(:,q); v=v(:,q);w=w(:,q);
du=du(:,q); dv=dv(:,q);dw=dw(:,q);p=p(:,q);

%Sorting eigenvalues and eigenfunctions with respect to ...
    imaginary part of radial wavenumber.
sorted, idx] = sort(abs(imag(C)), 'descend');
C = C(idx);X=X(:,idx);u=u(:,idx);v=v(:,idx);
w=w(:,idx);du=du(:,idx); dv=dv(:,idx);dw=dw(:,idx);p=p(:,idx);
nz=find(real(C)>tol );
C=C(nz);X=X(:,nz);u=u(:,nz);v=v(:,nz);w=w(:,nz);

```

```

du=du(:,nz);   dv=dv(:,nz); dw=dw(:,nz); p=p(:,nz);
L=length(C);

%Energy terms calculation
[P1,P2,P3,D,PW1,G1,G2,G3]=intfun(u,v,w,p,U,V,W,dU,dV,dW,du,dv,dw,...
L,z,R,C,beta,Ro);
TE= P1+P2+P3+D+PW1+G1+G2+G3; %Energy change of the system
fprintf(fid,'%f %f 
%f\n',beta,real(C(L)),imag(C(L)),P1,P2,P3,D,PW1,G1,G2,G3,TE);
Rc=real(C(L));
Ic=imag(C(L));

%Searching the neutral points
for j=1:iB
    betanew=beta+dB*j
    [C,er,z,X,u,v,w,p,U,V,W,dU,dV,dW,du,dv,dw]=chebsol(omega,...
betanew,Rnew,N,Ro,phi,eta);

q=find(abs(real(C))<1 & real(C)> 0 & abs(C-1/er)>1e-5 );

C=C(q);X=X(:,q); u=u(:,q); v=v(:,q);w=w(:,q);
du=du(:,q); dv=dv(:,q); dw=dw(:,q); p=p(:,q);

[sorted, idx] = sort(abs(imag(C)), 'descend');
C = C(idx);X=X(:,idx);u=u(:,idx);v=v(:,idx);w=w(:,idx);
du=du(:,idx); dv=dv(:,idx); dw=dw(:,idx); p=p(:,idx);

nz=find(real(C)>tol );
C=C(nz);X=X(:,nz);u=u(:,nz);v=v(:,nz);w=w(:,nz);
du=du(:,nz); dv=dv(:,nz); dw=dw(:,nz); p=p(:,nz);
L=length(C);

[P1,P2,P3,D,PW1,G1,G2,G3]=intfun(u,v,w,p,U,V,W,dU,dV,dW,du,dv,dw,...
L,z,R,C,betanew,Ro);
TE= P1+P2+P3+D+PW1+G1+G2+G3;

```

```

fprintf(fid, '%f %f %f %f %f %f %f %f %f %f ...
          %f\n', betanew, real(C(L)), imag(C(L)), P1, P2, P3, D, PW1, G1, G2, G3, TE);

if sign(imag(C(L)))  $\neq$  sign(Ic) %Neutral point at upper branch
count=count+1;
if count==1
betatemp=betanew+0.04;
break;

%Use this part to find neutral points on lower branch

end

Rc=real(C(L));
Ic=imag(C(L));
end
fclose(fid);
end

```

### A.2.2. Function for energy analysis

```

function [P1, P2, P3, D, PW1, G1, G2, G3]=intfun(u, v, w, p, ...
U, V, W, dU, dV, dW, du, dv, dw, L, z, R, C, beta, Ro)

U=U'; V=V'; W=W'; dU=dU'; dV=dV'; dW=dW';

i=sqrt(-1); alpha=C(L, :); norm=0; beta=beta/(R^2);

a=(0.5)*(paq(u(:, L), u(:, L))+paq(v(:, L), v(:, L))+paq(w(:, L), w(:, L))).*U+...
paq(u(:, L), p(:, L))-(1/R)*(paq(2*i*alpha*u(:, L), u(:, L))+paq(i*beta*R*u(:, L), ...
+i*alpha*v(:, L), v(:, L))+ paq(du(:, L)+ i*alpha*w(:, L), w(:, L))));

norm=trapz(z, a);

P1=trapz(z, paq(u(:, L), w(:, L)).*dU)/norm;

```

```

P2=trapz(z,paq(v(:,L),w(:,L)).*dV)/norm;
P3=-(trapz(z,paq(w(:,L),w(:,L)).*dW))*(Ro/(R*norm));

d=(2/R)*(paq(i*alpha*u(:,L),i*alpha*u(:,L))...
+paq(i*beta*R*v(:,L),i*beta*R*v(:,L))...
+paq(dw(:,L),dw(:,L)))+...
(1/R)*(paq(i*beta*R*u(:,L)+i*alpha*v(:,L),i*alpha*v(:,L))...
+paq(du(:,L)+i*alpha*w(:,L),i*alpha*w(:,L))...
+paq(i*alpha*v(:,L)+i*beta*R*u(:,L),i*beta*R*u(:,L))...
+paq(dv(:,L)+i*beta*R*w(:,L),i*beta*R*w(:,L))...
+paq(i*alpha*w(:,L)+du(:,L),du(:,L))...
+paq(i*beta*R*w(:,L)+dv(:,L),dv(:,L)));

D=trapz(z,d)/norm;

PW1=trapz(z,paq(u(:,L),p(:,L)).*dW)*(Ro/(R*norm));
G1=-trapz(z,0.5*(paq(du(:,L),du(:,L))+paq(dv(:,L),dv(:,L))...
+paq(dw(:,L),dw(:,L)))* (Ro*W/R))/norm;
G2=trapz(z,paq(u(:,L),u(:,L)).*U)*(Ro/R)/norm;
G3=trapz(z,paq(v(:,L),v(:,L)).*U)*(Ro/R)/norm;
end

%This function calculates Period Averaged Quantities
function y=paq(a,b)
y=a.*conj(b)+b.*conj(a);
end

```

### A.2.3. Functions for Chebyshev method

```

function [e,er,z,X,u,v,w,p,U,V,W,dU,dV,dW,du,dv,dw]=...
chebsol(omega,beta,R,N,Ro,phi,eta)

%Calculations of Chebyshev polynomials
[T,dT,d2T,y]=cheb(N);

```

```

%Transformation of Chebyshev polynomials into physical domain
[S, dS, d2S, z]=Rcheb2(T, dT, d2T, y, N, 20);

er=-20*sqrt(-1);
%Setup of matrices A0, A1 and A2
[A0,A1,A2,U,V,W,dU,dV,dW]=matrixA0A1A2(eta,N,S,dS,d2S,phi,z,omega,beta,R,Ro);

%Solving the quadratic eigenvalue problem.
[X,e]=polyeig(A0,A1,A2);

%Eigenfunctions and their derivatives
u=zeros((N+1),4*(N+1)*2); v=zeros((N+1),4*(N+1)*2); ...
    w=zeros((N+1),4*(N+1)*2);
p=zeros((N+1),4*(N+1)*2);

du=zeros((N+1),4*(N+1)*2); dv=zeros((N+1),4*(N+1)*2); ...
    dw=zeros((N+1),4*(N+1)*2);

for kk=1:length(e)
    for jj=1:(N+1)
        u(:,kk)=u(:,kk)+X(1+(jj-1)*4,kk)*S(:,jj);
        v(:,kk)=v(:,kk)+X(2+(jj-1)*4,kk)*S(:,jj);
        w(:,kk)=w(:,kk)+X(3+(jj-1)*4,kk)*S(:,jj);
        p(:,kk)=p(:,kk)+X(4+(jj-1)*4,kk)*S(:,jj);

        du(:,kk)=du(:,kk)+X(1+(jj-1)*4,kk)*dS(:,jj);
        dv(:,kk)=dv(:,kk)+X(2+(jj-1)*4,kk)*dS(:,jj);
        dw(:,kk)=dw(:,kk)+X(3+(jj-1)*4,kk)*dS(:,jj);
    end
end

function [T, dT, d2T, y] = cheb(N)
%this function calculates chebyshev polynomials and their ...
    derivatives

y=-cos(pi*(0:N)/N); %Gauss-Labotto points ordered -1 to 1

```

```

T=zeros(N+1,N+1); dT=T;d2T=T; T(1,:)=1; T(2,:)=y; dT(2,:)=1; ...
    dT(3,:)=4*T(2,:); d2T(3,:)=4*dT(2,:);

for i=2:N
    T(i+1,:)=2*y.*T(i,:)-T(i-1,:);
    if i>2
        dT(i+1,:)=2*T(i,:)+2*y.*dT(i,:)-dT(i-1,:); % simple ...
            derivative of the recursive expression
        d2T(i+1,:)=4*dT(i,:)+2*y.*d2T(i,:)-d2T(i-1,:); % simple ...
            derivative of the recursive expression
    end
end
T=T'; dT=dT'; d2T=d2T';

function [S, dS, d2S, z]= Rcheb2(T, dT, d2T, y, N,Zmax)
%Mapping of Chebyshev polynomials to the physical space
aa=1/4; B=2/(exp(-aa*Zmax)-1); A=-1-B; z=-log((y-A)/B)/aa;
dydz=-aa*B*exp(-aa*z)'; d2ydz2=aa^2*B*exp(-aa*z)'; i=sqrt(-1); ...
    er=-20*i;

S=T; dS=dT.*repmat(dydZ,1,N+1);
d2S=d2T.*repmat(dydZ,1,N+1).^2+dT.*repmat(d2ydz2,1,N+1);
end

function [A0,A1,A2,U,V,W,dU,dV,dW]=...
matrixA0A1A2(eta,N,S,dS,d2S,phi,z,omega,beta,R,Ro)
% This function includes Construction of Matrix A in AV=BVD
Co = 2 - Ro - Ro^2;
U = spline(eta,phi(1,:),z); V= spline(eta,phi(3,:),z);
W= spline(eta,phi(5,:),z);

dU = spline(eta,phi(2,:),z); dV= spline(eta,phi(4,:),z);
dW= -2*U;

for n=0:N

```

```

for k=1:N-1
    Mx=(i*beta*V(k+1)/R) - (i*omega) + (beta^2/R^3);
    J=S(k+1,n+1);
    dJ=dS(k+1,n+1);
    d2J=d2S(k+1,n+1);

    A2(4*k+1,4*n+1)=(1/R)*J; A2(4*k+1,4*n+2)=0;
    A2(4*k+1,4*n+3)=0; A2(4*k+1,4*n+4)=0;

    A2(4*k+2,4*n+1)=0; A2(4*k+2,4*n+2)=(1/R)*J;
    A2(4*k+2,4*n+3)=0; A2(4*k+2,4*n+4)=0;

    A2(4*k+3,4*n+1)=0; A2(4*k+3,4*n+2)=0;
    A2(4*k+3,4*n+3)=(1/R)*J; A2(4*k+3,4*n+4)=0;

    A2(4*k+4,4*n+1)=0; A2(4*k+4,4*n+2)=0;
    A2(4*k+4,4*n+3)=0; A2(4*k+4,4*n+4)=0;

    A1(4*k+1,4*n+1)=i*U(k+1)*J; A1(4*k+1,4*n+2)=0;
    A1(4*k+1,4*n+3)=0; A1(4*k+1,4*n+4)=i*J;

    A1(4*k+2,4*n+1)=0; A1(4*k+2,4*n+2)=i*U(k+1)*J;
    A1(4*k+2,4*n+3)=0; A1(4*k+2,4*n+4)=0;

    A1(4*k+3,4*n+1)=0; A1(4*k+3,4*n+2)=0;
    A1(4*k+3,4*n+3)=i*U(k+1)*J; A1(4*k+3,4*n+4)=0;

    A1(4*k+4,4*n+1)=i*J; A1(4*k+4,4*n+2)=0;
    A1(4*k+4,4*n+3)=0; A1(4*k+4,4*n+4)=0;

    A0(4*k+1,4*n+1)=(Mx+(U(k+1)*Ro/R))*J ...
        + (Ro*W(k+1)/R)*dJ-d2J/R;
    A0(4*k+1,4*n+2)=-((2*Ro*V(k+1)+Co)/R)*J;
    A0(4*k+1,4*n+3)=dU(k+1)*J; A0(4*k+1,4*n+4)=0;

    A0(4*k+2,4*n+1)=((2*Ro*V(k+1)+Co)/R)*J;

```

```

A0(4*k+2,4*n+2)=(Mx+(U(k+1)*Ro/R))*J+(Ro*W(k+1)/R)*dJ-d2J/R;
A0(4*k+2,4*n+3)=dV(k+1)*J; A0(4*k+2,4*n+4)=(i*beta/R)*J;

A0(4*k+3,4*n+1)=0; A0(4*k+3,4*n+2)=0;
A0(4*k+3,4*n+3)=(Mx+(dW(k+1)*Ro/R))*J+Ro*(W(k+1)/R)*dJ-d2J/R;
A0(4*k+3,4*n+4)=dJ;

A0(4*k+4,4*n+1)=(Ro/R)*J; A0(4*k+4,4*n+2)=i*beta*J/R;
A0(4*k+4,4*n+3)=dJ; A0(4*k+4,4*n+4)=0;

end

%BC at the wall
A2(1,4*n+1)=0; A2(1,4*n+2)=0; A2(1,4*n+3)=0; A2(1,4*n+4)=0;
A2(2,4*n+1)=0; A2(2,4*n+2)=0; A2(2,4*n+3)=0; A2(2,4*n+4)=0;
A2(3,4*n+1)=0; A2(3,4*n+2)=0; A2(3,4*n+3)=0; A2(3,4*n+4)=0;
A2(4,4*n+1)=0; A2(4,4*n+2)=0; A2(4,4*n+3)=0; A2(4,4*n+4)=0;

A1(1,4*n+1)=er*S(1,n+1); A1(1,4*n+2)=0; A1(1,4*n+3)=0; ...
    A1(1,4*n+4)=0;
A1(2,4*n+1)=0; A1(2,4*n+2)=er*S(1,n+1); A1(2,4*n+3)=0; ...
    A1(2,4*n+4)=0;
A1(3,4*n+1)=0; A1(3,4*n+2)=0; A1(3,4*n+3)=er*S(1,n+1); ...
    A1(3,4*n+4)=0;
A1(4,4*n+1)=0; A1(4,4*n+2)=0; ...
    A1(4,4*n+3)=er*dS(1,n+1);A1(4,4*n+4)=0;

A0(1,4*n+1)=S(1,n+1); A0(1,4*n+2)=0; A0(1,4*n+3)=0; ...
    A0(1,4*n+4)=0;
A0(2,4*n+1)=0; A0(2,4*n+2)=S(1,n+1); A0(2,4*n+3)=0; ...
    A0(2,4*n+4)=0;
A0(3,4*n+1)=0; A0(3,4*n+2)=0; A0(3,4*n+3)=S(1,n+1); ...
    A0(3,4*n+4)=0;
A0(4,4*n+1)=0; A0(4,4*n+2)=0; A0(4,4*n+3)=dS(1,n+1); ...
    A0(4,4*n+4)=0;

%BC at infinity

```

```

A2 (4*N+1, 4*n+1)=0; A2 (4*N+1, 4*n+2)=0; A2 (4*N+1, 4*n+3)=0;
A2 (4*N+1, 4*n+4)=0;
A2 (4*N+2, 4*n+1)=0; A2 (4*N+2, 4*n+2)=0; A2 (4*N+2, 4*n+3)=0;
A2 (4*N+2, 4*n+4)=0;
A2 (4*N+3, 4*n+1)=0; A2 (4*N+3, 4*n+2)=0; A2 (4*N+3, 4*n+3)=0;
A2 (4*N+3, 4*n+4)=0;
A2 (4*N+4, 4*n+1)=0; A2 (4*N+4, 4*n+2)=0; A2 (4*N+4, 4*n+3)=0;
A2 (4*N+4, 4*n+4)=0;

```

```

A1 (4*N+1, 4*n+1)=er*S(N+1, n+1); A1 (4*N+1, 4*n+2)=0;
A1 (4*N+1, 4*n+3)=0; A1 (4*N+1, 4*n+4)=0;
A1 (4*N+2, 4*n+1)=0; A1 (4*N+2, 4*n+2)=er*S(N+1, n+1);
A1 (4*N+2, 4*n+3)=0; A1 (4*N+2, 4*n+4)=0;
A1 (4*N+3, 4*n+1)=0; A1 (4*N+3, 4*n+2)=0;
A1 (4*N+3, 4*n+3)=er*S(N+1, n+1); A1 (4*N+3, 4*n+4)=0;
A1 (4*N+4, 4*n+1)=0; A1 (4*N+4, 4*n+2)=0;
A1 (4*N+4, 4*n+3)=0; A1 (4*N+4, 4*n+4)=er*S(N+1, n+1);

```

```

A0 (4*N+1, 4*n+1)=S(N+1, n+1); A0 (4*N+1, 4*n+2)=0;
A0 (4*N+1, 4*n+3)=0; A0 (4*N+1, 4*n+4)=0;
A0 (4*N+2, 4*n+1)=0; A0 (4*N+2, 4*n+2)=S(N+1, n+1);
A0 (4*N+2, 4*n+3)=0; A0 (4*N+2, 4*n+4)=0;
A0 (4*N+3, 4*n+1)=0; A0 (4*N+3, 4*n+2)=0;
A0 (4*N+3, 4*n+3)=S(N+1, n+1); A0 (4*N+3, 4*n+4)=0;
A0 (4*N+4, 4*n+1)=0; A0 (4*N+4, 4*n+2)=0;
A0 (4*N+4, 4*n+3)=0; A0 (4*N+4, 4*n+4)=S(N+1, n+1);

```

end

# List of References

- Alveroglu, B., Segalini, A., & Garrett, S. J. 2016a. The effect of surface roughness on the convective instability of the BEK family of boundary-layer flows. *European Journal of Mechanics-B/Fluids*, **56**, 178–187.
- Alveroglu, B., Segalini, A., & Garrett, S. J. 2016b. An energy analysis of convective instabilities of the Bödewadt and Ekman boundary layers over rough surfaces. *to appear in Proceedings of the 16th International Symposium on Transport Phenomena and Dynamics of Rotating Machinery, ISROMAC-16, Honolulu, HI, USA.*
- Appelquistt, E. 2014 (May). *Direct numerical simulations of the rotating-disk boundary-layer flow*. Ph.D. thesis, KTH Mechanics, Stockholm-Sweden.
- Balakumar, P., & Malik, M. R. 1990. Traveling disturbances in rotating-disk flow. *Theoretical and Computational Fluid Dynamics*, **2**(3), 125–137.
- Batchelor, G. K. 1951. Note on a class of solutions of the Navier-Stokes equations representing steady rotationally-symmetric flow. *The Quarterly Journal of Mechanics and Applied Mathematics*, **4**(1), 29–41.
- Bechert, D. W., Hoppe, G., & Reif, W. E. 1985. *Paper# AIAA-85-0546, presented at AIAA Shear Flow Control Conference.*
- Bers, A. 1975. Linear waves and instabilities. *In: Plasma physics–les houches 1972.*
- Billant, P., Chomaz, J., Delbende, I., Huerre, P., Loiseleux, T., Olendraru, C., Rossi, M., & Sellier, A. 1998. Instabilities and vortex breakdown in swirling jets and

- wakes. *Pages 267–286 of: IUTAM Symposium on Dynamics of Slender Vortices*. Springer.
- Bödewadt, U. T. 1940. Die drehströmung über festem grunde. *ZAMM-Journal of Applied Mathematics and Mechanics/Zeitschrift für Angewandte Mathematik und Mechanik*, **20**(5), 241–253.
- Bridges, T. J., & Morris, P. J. 1984. Differential eigenvalue problems in which the parameter appears nonlinearly. *Journal of Computational Physics*, **55**(3), 437–460.
- Briggs, R. J. 1964. Electron-stream interaction with plasmas.
- Canuto, C., Hussaini, M. Y., Quarteroni, A., & Zang, T. A. 1988. *Spectral methods in fluid dynamics*. Tech. rept. Springer.
- Carpenter, P. 1997. The right sort of roughness. *Nature*, **388**(6644), 713–714.
- Chomaz, J. 2004. Transition to turbulence in open flows: what linear and fully non-linear local and global theories tell us. *European Journal of Mechanics-B/Fluids*, **23**(3), 385–399.
- Colley, A. J., Thomas, P. J., Carpenter, P. W., & Cooper, A. J. 1999. An experimental study of boundary-layer transition over a rotating, compliant disk. *Physics of Fluids (1994-present)*, **11**(11), 3340–3352.
- Cooper, A. J., & Carpenter, P. W. 1997. The stability of rotating-disc boundary-layer flow over a compliant wall. Part 1. Type I and II instabilities. *Journal of Fluid Mechanics*, **350**, 231–259.
- Cooper, A. J., Harris, J. H., Garrett, S. J., Özkan, M., & Thomas, P. J. 2015. The effect of anisotropic and isotropic roughness on the convective stability of the rotating disk boundary layer. *Physics of Fluids (1994-present)*, **27**(1), 014107.
- Corke, T. C., & Knasiak, K. F. 1998. Stationary travelling cross-flow mode interactions on a rotating disk. *Journal of Fluid Mechanics*, **355**, 285–315.

- Corke, T. C., Matlis, E. H., & Othman, H. 2007. Transition to turbulence in rotating-disk boundary layers convective and absolute instabilities. *Journal of Engineering Mathematics*, **57**(3), 253–272.
- Cros, A., Floriani, E., Le Gal, P., & Lima, R. 2005. Transition to turbulence of the Batchelor flow in a rotor/stator device. *European Journal of Mechanics-B/Fluids*, **24**(4), 409–424.
- Davies, C., & Carpenter, P. W. 2003. Global behaviour corresponding to the absolute instability of the rotating-disc boundary layer. *Journal of fluid mechanics*, **486**, 287–329.
- Dhanak, M. R. 1992. Effects of uniform suction on the stability of flow on a rotating disc. *Pages 431–440 of: Proceedings of the Royal Society of London A: Mathematical, Physical and Engineering Sciences*, vol. 439. The Royal Society.
- Drazin, P. G., & Reid, W. H. 2004. *Hydrodynamic stability*. Cambridge university press.
- Ekman, V. W. 1905. On the influence of the earth's rotation on ocean currents. *Ark. Mat. Astron. Fys.*, **2**, 1–53.
- Faller, A. J. 1963. An experimental study of the instability of the laminar Ekman boundary layer. *J. Fluid Mech*, **15**(163), 560–576.
- Faller, A. J., & Kaylor, R. E. 1966. A numerical study of the instability of the laminar Ekman boundary layer. *Journal of the Atmospheric Sciences*, **23**(5), 466–480.
- Fasel, H. 1976. Investigation of the stability of boundary layers by a finite-difference model of the Navier-Stokes equations. *Journal of Fluid Mechanics*, **78**(02), 355–383.
- Finlayson, B. A. 2013. *The method of weighted residuals and variational principles*. Vol. 73. SIAM.

- Floriani, E., de Wit, T. D., & Le Gal, P. 2000. Nonlinear interactions in a rotating disk flow: From a Volterra model to the Ginzburg–Landau equation. *Chaos: An Interdisciplinary Journal of Nonlinear Science*, **10**(4), 834–847.
- Gajjar, J. S. B. 1996. On the nonlinear evolution of a stationary cross-flow vortex in a fully three-dimensional boundary layer flow. *Pages 317–326 of: IUTAM Symposium on Nonlinear Instability and Transition in Three-Dimensional Boundary Layers*. Springer Netherlands.
- Garrett, S. J. 2009. Linear growth rates of types I and II convective modes within the rotating-cone boundary layer. *Fluid dynamics research*, **42**(2), 025504.
- Garrett, S. J., & Peake, N. 2002. The stability and transition of the boundary layer on a rotating sphere. *Journal of Fluid Mechanics*, **456**, 199–218.
- Garrett, S. J., Hussain, Z., & Stephen, S. O. 2009. The cross-flow instability of the boundary layer on a rotating cone. *Journal of Fluid Mechanics*, **622**, 209–232.
- Garrett, S. J., Harris, J., & Thomas, P. J. 2012. On the effect of distributed roughness on transition over rotor-stator devices. *Proc. 28th ICAS Cong.*, 18.
- Garrett, S. J., Cooper, A. J., Harris, J. H., Ozkan, M., Segalini, A., & Thomas, P. J. 2016. On the stability of von Kármán rotating-disk boundary layers with radial anisotropic surface roughness. *Physics of Fluids*, **28**(1).
- Gaster, M. 1962. A note on the relation between temporally-increasing and spatially-increasing disturbances in hydrodynamic stability. *Journal of Fluid Mechanics*, **14**(02), 222–224.
- Gray, W. E. 1952. The nature of the boundary layer flow at the nose of a swept wing. *Roy. Aircraft Est. TM*, **256**.
- Gregory, N., & Walker, W. S. 1960. Experiments on the effect of suction on the flow due to a rotating disk. *Journal of Fluid Mechanics*, **9**(02), 225–234.

- Gregory, N., Stuart, J. T., & Walker, W. S. 1955. On the stability of three-dimensional boundary layers with application to the flow due to a rotating disk. *Philosophical Transactions of the Royal Society of London A: Mathematical, Physical and Engineering Sciences*, **248**(943), 155–199.
- Gustavsson, L. H. 1979. Initial-value problem for boundary layer flows. *Physics of Fluids (1958-1988)*, **22**(9), 1602–1605.
- Hall, P. 1986. An asymptotic investigation of the stationary modes of instability of the boundary layer on a rotating disc. *Pages 93–106 of: Proceedings of the Royal Society of London A: Mathematical, Physical and Engineering Sciences*, vol. 406. The Royal Society.
- Healey, J. J. 2010. Model for unstable global modes in the rotating-disk boundary layer. *Journal of Fluid Mechanics*, **663**, 148–159.
- Howard, L. N., & Gupta, A. S. 1962. On the hydrodynamic and hydromagnetic stability of swirling flows. *Journal of Fluid Mechanics*, **14**(03), 463–476.
- Huerre, P., & Monkewitz, P. A. 1990. Local and global instabilities in spatially developing flows. *Annual review of fluid mechanics*, **22**(1), 473–537.
- Huerre, P., Batchelor, G. K., Moffatt, H. K., & Worster, M. G. 2000. Open shear flow instabilities. *Perspectives in Fluid Dynamics*, 159–229.
- Imayama, S., Alfredsson, P. H., & Lingwood, R. J. 2014. On the laminar–turbulent transition of the rotating-disk flow: the role of absolute instability. *Journal of Fluid Mechanics*, **745**, 132–163.
- Jasmine, H. A. 2003. *Absolute and convective instability in some rotating fluid flows..* Ph.D. thesis, University of Manchester.
- Jasmine, H. A., & Gajjar, J. S. B. 2005. Convective and absolute instability in the incompressible boundary layer on a rotating disk in the presence of a uniform magnetic field. *Journal of engineering mathematics*, **52**(4), 337–353.

- Khorrani, M. R. 1991. On the viscous modes of instability of a trailing line vortex. *Journal of Fluid Mechanics*, **225**, 197–212.
- Khorrani, M. R., Malik, M. R., & Ash, R. L. 1989. Application of spectral collocation techniques to the stability of swirling flows. *Journal of Computational Physics*, **81**(1), 206–229.
- Kierzenka, J., & Shampine, L. F. 2001. A BVP solver based on residual control and the Maltab PSE. *ACM Transactions on Mathematical Software (TOMS)*, **27**(3), 299–316.
- Landau, L. D. 1946. On the vibrations of the electronic plasma. *Zh. Eksp. Teor. Fiz.*, **10**, 25.
- Lessen, M., Sadler, S. G., & Liu, T. 1968. Stability of pipe Poiseuille flow. *Physics of Fluids (1958-1988)*, **11**(7), 1404–1409.
- Lilly, D. K. 1966. On the instability of Ekman boundary flow. *Journal of the Atmospheric Sciences*, **23**(5), 481–494.
- Lingwood, R. J. 1995. Absolute instability of the boundary layer on a rotating disk. *Journal of Fluid Mechanics*, **299**, 17–33.
- Lingwood, R. J. 1996. An experimental study of absolute instability of the rotating-disk boundary-layer flow. *Journal of Fluid Mechanics*, **314**, 373–405.
- Lingwood, R. J. 1997. Absolute instability of the Ekman layer and related rotating flows. *Journal of Fluid Mechanics*, **331**, 405–428.
- Lingwood, R.J., & Garrett, S.J. 2011. The effects of surface mass flux on the instability of the BEK system of rotating boundary-layer flows. *European Journal of Mechanics-B/Fluids*, **30**(3), 299–310.
- Mack, L. M. 1985. The wave pattern produced by a point source on a rotating disk. *In: AIAA, Aerospace Sciences Meeting*, vol. 1.

- Malik, M. R. 1986. The neutral curve for stationary disturbances in rotating-disk flow. *Journal of Fluid Mechanics*, **164**, 275–287.
- Melander, M. V. 1983. An algorithmic approach to the linear stability of the Ekman layer. *Journal of Fluid Mechanics*, **132**, 283–293.
- Miklavcic, M., & Wang, C.Y. 2004. The flow due to a rough rotating disk. *Zeitschrift für angewandte Mathematik und Physik ZAMP*, **55**(2), 235–246.
- Murdock, J. W. 1977. Numerical Study of Nonlinear Effects on Boundary-Layer Stability. *AIAA Journal*, **15**(8), 1167–1173.
- Navier, C. L. M. 1827. Sur les lois du mouvement des fluides. *Comp. Ren. Acad. Sci.* **6**.
- Orszag, S. A. 1971. Accurate solution of the Orr–Sommerfeld stability equation. *Journal of Fluid Mechanics*, **50**(04), 689–703.
- Othman, H., & Corke, T. C. 2006. Experimental investigation of absolute instability of a rotating-disk boundary layer. *Journal of Fluid Mechanics*, **565**, 63–94.
- Peyret, R. 2013. *Spectral methods for incompressible viscous flow*. Vol. 148. Springer Science & Business Media.
- Sahoo, B., Abbasbandy, S., & Poncet, S. 2014. A brief note on the computation of the Bödewadt flow with Navier slip boundary conditions. *Computers & Fluids*, **90**, 133–137.
- Saric, W. S., & Reed, H. L. 2003. Crossflow instabilities theory & technology. *AIAA paper*, **771**, 2003.
- Savas, Ö. 1987. Stability of Bödewadt flow. *Journal of Fluid Mechanics*, **183**, 77–94.
- Schmid, P. J., & Henningson, D. S. 2012. *Stability and transition in shear flows*. Vol. 142. Springer Science & Business Media.

- Sirovich, L., & Karlsson, S. 1997. Turbulent drag reduction by passive mechanisms. *Nature*, **388**(6644), 753–755.
- Smith, N. H. 1947. Exploratory investigation of laminar-boundary-layer oscillations on a rotating disk.
- Spalart, P. R., Moser, R. D., & Rogers, M. M. 1991. Spectral methods for the Navier-Stokes equations with one infinite and two periodic directions. *Journal of Computational Physics*, **96**(2), 297–324.
- Sparrow, E. M., & Cess, R. D. 1962. Magnetohydrodynamic flow and heat transfer about a rotating disk. *Journal of Applied Mechanics*, **29**(1), 181–187.
- Tatro, P. R., & Mollo-Christensen, E. L. 1967. Experiments on Ekman layer instability. *Journal of Fluid Mechanics*, **28**(03), 531–543.
- Thomas, C. 2007. *Numerical simulations of disturbance development in rotating boundary-layers*. Ph.D. thesis, Cardiff University.
- Turkyilmazoglu, M. 2009. Effects of mass transfer on a resonance instability in the laminar boundary layer flow over a rotating-disk. *Sadhana*, **34**(6), 947–965.
- Van de Vooren, A. I., Botta, E. F. F., & Stout, J. 1987. The boundary layer on a disk at rest in a rotating fluid. *The Quarterly Journal of Mechanics and Applied Mathematics*, **40**(1), 15–32.
- von Kármán, T. 1921. Über Laminare und Turbulente Reibung. *Z. Angew. Math. Mech.*
- Walsh, M. J. 1982. AIAA Pap. 82-0169. *Reston (Va.): AIAA*, **2**.
- Watanabe, T., Warui, H. M., & Fujisawa, N. 1993. Effect of distributed roughness on laminar-turbulent transition in the boundary layer over a rotating cone. *Experiments in fluids*, **14**(5), 390–392.
- Watson, J. 1962. On spatially-growing finite disturbances in plane Poiseuille flow. *Journal of Fluid Mechanics*, **14**(02), 211–221.

- Yoon, M. S., Hyun, J. M., & Park, J. S. 2007. Flow and heat transfer over a rotating disk with surface roughness. *International journal of heat and fluid flow*, **28**(2), 262–267.
- Zebib, A. 1984. A Chebyshev method for the solution of boundary value problems. *Journal of Computational Physics*, **53**(3), 443–455.